CHAPTER 3

Heat transfer to objects in pool fires

J.P. Spinti, J.N. Thornock, E.G. Eddings, P.J. Smith & A.F. Sarofim
Department of Chemical Engineering, University of Utah, USA.

Abstract

In accident scenarios involving fire and the transport of explosive material, the time available for escape is dependent on the heat transfer rate from the fire to the energetic material. A review is presented of historical modeling approaches that draw on empiricism for estimating both heat flux from fires and fire hazard. While such methods can be used for conservative estimates of heat flux in determining safe separation distances, they cannot be used in situations where overestimating the heat flux may underestimate the hazard, such as the heating of high-energy explosives. Next, a large eddy simulation (LES) technique for addressing fire phenomena with embedded, heat sensitive objects is described. With the advent of high performance computing, LES is emerging as a powerful tool for resolving a large set of spatial and temporal scales in fires and for capturing observed pool fire phenomena such as visible flame structures. The development of the LES approach described here is based on verification and validation (V&V) principles, utilizing a V&V hierarchy that is focused on the intended use of the simulation. This LES approach couples surrogate fuel representations of complex hydrocarbon fuels, reaction models for incorporation of the detailed chemical kinetics associated with the surrogate fuel, soot formation models, models for unresolved turbulence/chemistry interactions, radiative heat transfer models, and modifications to the LES algorithm for computing heat transfer to objects. The chapter concludes with an analysis of simulation and experimental data of heat transfer to embedded objects in large JP-8 pool fires and of time to ignition of an energetic device in such a fire. The analysis considers the role of validation, sensitivity analysis and uncertainty quantification in moving toward predictivity.

1 Introduction

Explosives are transported via highway, rail line, and air for use in mining, space exploration, building demolition, pyrotechnics, avalanche control, and military

applications. In addition, certain hydrocarbons, most notably liquefied petroleum gas (LPG, mainly composed of propane), can explode when the storage vessel is heated by an external fire, resulting in the so-called boiling liquid expanding vapor explosion (BLEVE). For these events, the time to explosion is critical as it determines the time available for first responders to intervene and for those at the scene of an accident to escape.

On August 10, 2005, a semi-trailer truck carrying 38,000 pounds of mining explosives tipped over, skidded across the pavement, caught fire, and then detonated in Spanish Fork Canyon, Utah. The driver was negotiating a sharp turn at an excessive speed when the accident occurred. Eyewitnesses estimated a time of three minutes from the start of the fire to the detonation event. The blast left a crater 30 feet deep and 70 feet wide in the road, and the truck was reduced to shards of metal, frayed pieces of tire, and an engine block. This incident and others like it provide the motivation for calculating the potential hazard of an explosive device immersed in a pool fire of transportation fuel.

Heat transfer to objects in or near pool fires has been the subject of study for decades. Traditionally, the focus has been on determining a safe separation distance from the fire. Calculation with a conservatively high heat flux provided a good margin of safety. However, there are times when conservative estimations of heat flux are inadequate for determining the magnitude of the hazard, particularly when dealing with containers of energetic materials. For example, some energetic materials may detonate under slow heating (slow cook-off) conditions and deflagrate under rapid heating (fast cook-off) conditions. Overestimating the heat flux may underestimate the hazard, motivating the need for physically-based methods that accurately predict heat flux from pool fires to embedded objects. In this chapter, the hazard is characterized in terms of the time to ignition of the explosive device and the violence (measured as kinetic energy of the exploded container) of the event.

Full-scale experimental investigation of heat transfer to objects in or near pool fires is limited because such experiments are expensive and difficult to instrument due to the harsh environment. Consequently, pool fire dynamics and heat transfer have been studied in small-scale, controlled laboratory settings, where detailed instrumentation yields high quality, quantitative data that is used to gain insight into the fire physics and the heat transfer process. Fire simulation tools based on computational fluid dynamics (CFD) offer a way to scale the laboratory experiments to larger, more realistic scenarios involving a variety of accidental conditions including wind speed and direction, size of the fire (1−100 m), and position of the object relative to the fire.

1.1 Chapter outline

Section 2 reviews the semi-empirical modeling approaches that have been employed to estimate the radiation field from hydrocarbon pool fires. The fire community has used these approaches to provide immediate and practical engineering estimates of the radiation hazard. However, these approaches are unable to predict, a priori, the effects of changing fuels, wind conditions, and fire configurations.

Section 3 presents a framework for predicting heat transfer to embedded objects in pool fires based on a foundation of verification and validation (V&V). Sections 4–9 review next generation modeling tools for achieving high fidelity transportation fuel pool fire simulations within the V&V framework. Section 4 details how transportation fuels composed of complex mixtures can be represented by surrogate fuels that approximate the physical and chemical characteristics of the original fuel. Section 5 evaluates the capability of a chemical kinetic mechanism developed for such surrogate fuels to predict concentrations of soot precursors and outlines four methodologies for calculating soot from its precursors. Section 6 discusses large eddy simulation (LES), a sophisticated numerical approach that captures describes the dynamics of buoyant pool fires. Section 7 describes a parameterization methodology (e.g. reaction model) for reducing the degrees of freedom in detailed kinetic schemes of transportation fuel combustion. Section 8 discusses models that account for the complex and coupled interactions between turbulence and chemistry at the unresolved scale. Together, the reaction model and the model for turbulence/chemistry interactions allow complex combustion chemistry to be coupled to the LES simulation in a realistic way. Section 9 provides an overview of radiation, the dominant mode of heat transfer in most large pool fires, and its complexities as a spatial and spectral phenomenon.

Section 10 provides a brief overview of validation activities for heat transfer to embedded objects in transportation fuel pool fires. These activities focus on the use of a validation metric to quantify the level of agreement between experimental and simulation data. Section 11 illustrates the application of the LES fire simulation tool to the prediction of heat flux to an explosive device in a full scale hazards classification test for which data is unavailable. Section 12 demonstrates how an energetic material model can be coupled to the fire simulation tool to predict time to ignition of an explosive device. As the emphasis of this chapter is on predictive models, Section 13 concludes the chapter with a brief discussion on error quantification and predictivity.

2 Historical modeling approaches

2.1 Homogeneous flame

The early models of heat transfer from flames are based on the 1959 review by Hottel [1] of Blinkov and Khudiakov's data on burning rate and flame height as seen in Fig. 1. The data include a number of fuels in pans with diameters ranging from 0.4 cm to 30 m.

The data were rationalized by equating the heat flux density, q'', to the vaporization rate of the fuel, $\dot{m}''$, multiplied by the heat of vaporization, Δh_{vap}. The heat flux to the fuel was decomposed into conduction, convection, and radiation contributions to give,

$$\dot{m}'' \Delta h_{\mathrm{vap}} = q'' = \frac{4K}{d}(T_{\mathrm{F}} - T_{\mathrm{o}}) + h(T_{\mathrm{F}} - T_{\mathrm{o}}) + \sigma F(T_{\mathrm{F}}^4 - T_{\mathrm{o}}^4)(1 - \mathrm{e}^{-Kad}). \qquad (1)$$
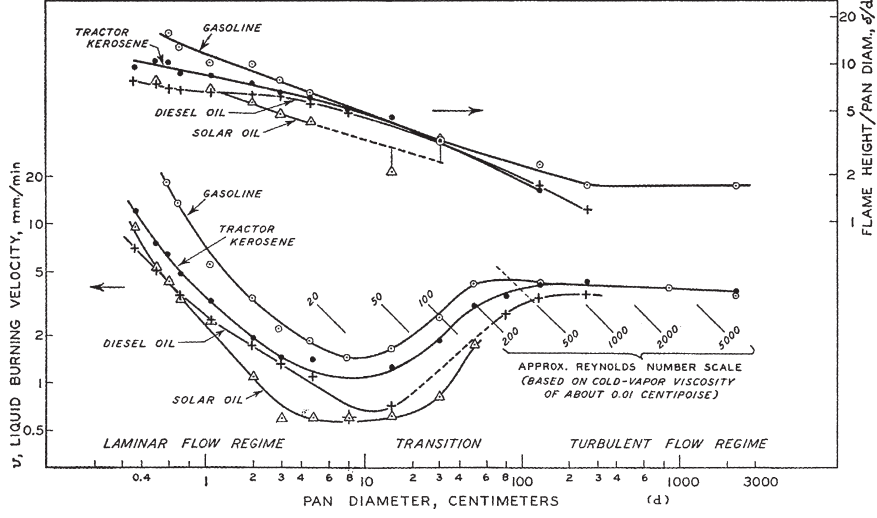
Figure 1: Correlation by Hottel [1] of burning rate and flame height from pool fires as a function of pan diameter.

The first term on the right-hand side of eqn (1) represents conduction from the rim of the pan at the flame temperature, T_F, to the liquid at T_o, where K is the liquid conductivity and d is the pan diameter. The second term represents convection from the flame to the liquid, where h is the convective heat transfer coefficient. The third term represents the radiation from the flame, where F is the view factor from the flame to the pan, σ is the Stefan–Boltzmann constant, K is the absorption coefficient in the flame, and a is the ratio of the mean beam length to the pan diameter. This simplified model invokes the assumption of a homogeneous flame. Hence, a turbulent flame is assumed to have homogeneous gaseous and soot concentrations at some 'effective radiation temperature'.

Hottel [1] established the framework for current semi-empirical models used to estimate radiation. For example, in Fig. 2 the fire is approximated by a cylinder at a uniform temperature and composition with a height H_F, diameter D_F, and temperature T_F. Consider the flux per unit area, $\dot{q}_S$, to an element at a distance R_{FS} from the fire (eqn (2)),

$$\dot{q}_S = F_{FS}\varepsilon_F\sigma T_F^4, \tag{2}$$

where

$$F_{FS} = f(H_F, D_F, R_{FS}), \tag{3}$$

and

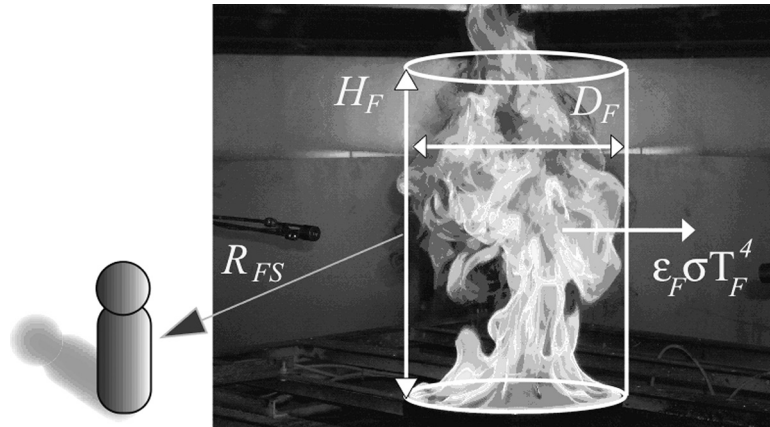$$(1-\varepsilon_F) = (1-\varepsilon_{CO_2})(1-\varepsilon_{H_2O})(1-\varepsilon_{soot}). \tag{4}$$

Figure 2: Approximation of a fire by a homogeneous cylinder. Photograph taken by William Ciro, 2005.

To estimate the radiation from a homogeneous flame, one needs to know the flame shape and size to compute the geometric view factor, F_{FS}; the flame absorption coefficient/flame emissivity, computed from both gas emissivities (ε_{CO_2}, ε_{H_2O}) and soot emissivity (ε_{soot}); and an effective flame temperature, T_F. Various semi-empirical approaches for estimating the radiation field in and around hydrocarbon pool fires have been reviewed by De Ris [2] and Mudan [3]. A conical or cylindrical flame shape is usually assumed over a circular pool. A flame height can either be estimated through photographs or from the burning rate of the fuel. The nondimensional flame height (flame height to pool diameter ratio) has been found to correlate well with a nondimensional mass burning rate [3, 4]. Correlations relating the flame tilt angle from the vertical to wind velocity are also available [2].

Once the shape and size of the fire are calculated, the radiative characteristics of the fire need to be determined. The radiative properties of the flame are often estimated in the form of gray absorption coefficients or gray emissivities by assuming a homogenous mixture of CO_2, H_2O, and soot. Correlations are currently available for the spectral emissivities of combustion products of hydrocarbons [5]. The relative magnitude of CO_2, H_2O and soot emissivities are shown in Fig. 3 for partial pressures of CO_2 and H_2O of 0.12, a soot volume fraction of 10^{-7}, a mean beam length of 3 m, and a flame temperature of 1,200 K. At 1,200 K, three quarters of the blackbody spectrum is in the 2.4–4.8 μm range, a range where soot radiation dominates. Therefore, the determination of soot emission and absorption is critical in computing accurate radiant heat fluxes from flames.

An alternative method of describing the fire hazard of a fuel is to estimate the total radiative output of the fire to its surroundings and report that radiative output as a fraction (χ_R) of the total heat of combustion. This fraction cannot be determined theoretically and is normally estimated [2].
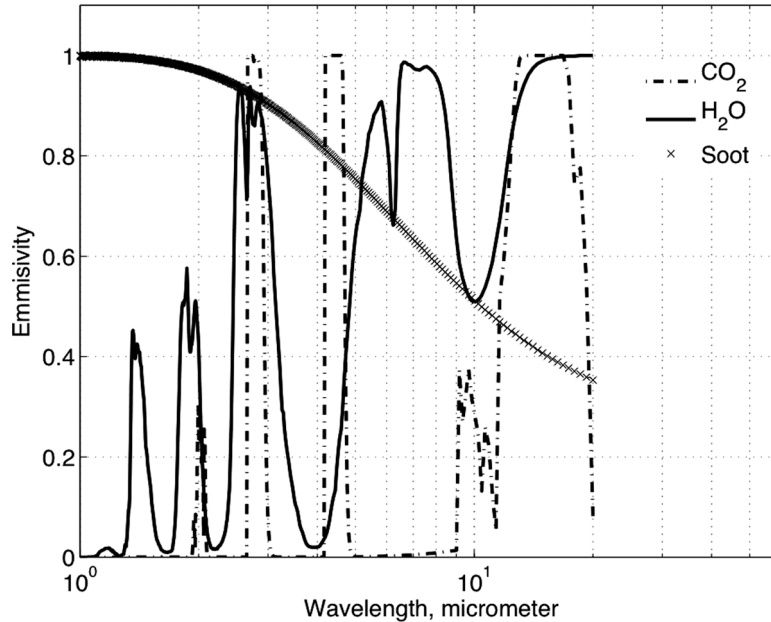
Figure 3: Spectral emissivities of CO_2 (p_{CO_2} = 0.12), H_2O (p_{H_2O} = 0.12), and soot (volume fraction = 10^{-7}) at 1,200 K for a mean beam length of 3 m.

2.2 Homogeneous model and observable fire phenomena

The major shortcoming of the homogeneous model is the evaluation of the effective flame temperature. In his review, Hottel assumed a value of 1,100 K [1]. The effective flame temperature, however, is dependent on pool size and to a lesser degree on fuel type [6, 7]. Figure 4 shows average surface emissive power as a function of pool diameter for a range of fuels. In general, the radiation is found to increase with pool diameter as a result of the increase in emissivity. However, for large pool fires, the radiation decreases as a result of the shielding of flame radiation by the outer, cooler soot layers. This phenomenon is evident in Fig. 4, where several fuels show an effective emissive power of the flame surface passing through a maximum at pool diameters of 1−10 m, with peak values near 150 kW/m². Liquid natural gas (LNG) is the exception; being lightly sooting, its shielding effects are not yet evident. For this reason, the maximum radiation for large LNG flames exceeds that of more sooting fuels. In the review by Mudan and Croce [8], peak emissive power values of 220 kW/m² are reported for land-based LNG fires (higher values are found on water) compared with peak values of 160 kW/m² for LPG and 130 kW/m² for gasoline.

The shielding of the core of the flame by soot has been studied for some time, with Smith [9] first proposing models that tried to provide a mathematical framework for the observations of the periodic transport to the surface of large eddies
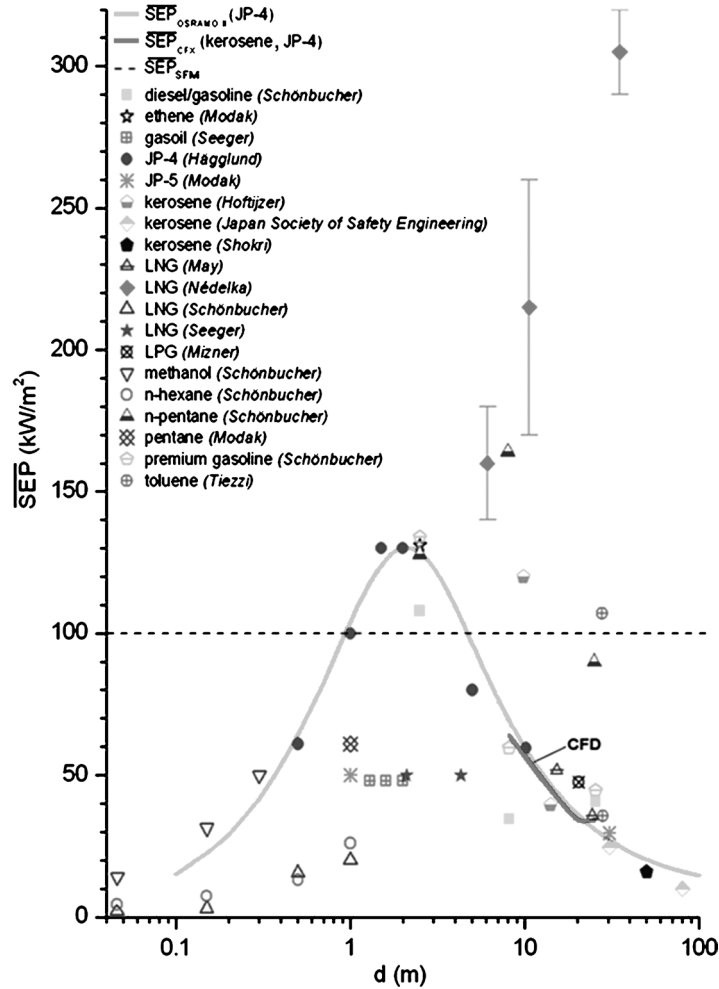
Figure 4: Average surface emissive power of pool fires for different fuels as a function of pool diameter [6].

from the hot core. The emissive powers of larger flames vary widely due to this phenomenon. Mudan [3] estimated that the luminous zones covered 20% of the surface of the flame and had emissive powers in the range of 110–130 kW/m^2, while the cooler background had an emissive power of 20 kW/m^2. Thermographic cameras have been used by Schönbucher's research group to obtain time-resolved measurements of the emissive power distribution in flames. They have developed probabilistic models that describe hot spots with surface emissive powers ranging from 33 to 430 kW/m^2 and colder soot parcels with surface emissive powers ranging from 6 to 50 kW/m^2 [7].

Radiative fluxes to the pool surface and even at locations away from the fire are likely to be influenced by the assumed flame size and shape, quantified by geometric view factors [10]. Numerical estimates of the radiative heat fluxes to the pool surface from 30 cm diameter pool fires employing the homogeneous model were found to be higher than the experimental values by 40% [2]. Most of this error was attributed to assuming a conical shape to the flame.

Another shortcoming of the homogeneous model is its inability to predict the radiative feedback to the pool surface, particularly in large pool fires. Obtaining accurate estimates of the radiative fluxes to the pool surface is important for determining fuel burning rates. Hottel [1] was able to explain the trends in the burning rates of liquid fuels by relating the rate of heat transfer from the fire to the pool to the rate of fuel vaporization, but the effective emissive power of the flame that he assumed was, in effect, a fitting parameter. The cooler, unburned, sooty pyrolysis gases near the fuel surface in large fires may block part of the flame radiation from reaching the surface, similar to the effects observed for external heat transfer. Shinotake *et al.* [10] showed that radiation blockage significantly affects the fuel burning rates in pool fires of diameters greater than 1 m. They also observed that the experimentally measured radiative fluxes to the pool increased with increase in diameter but then quickly saturated compared to the external fluxes. They explained these observations in terms of radiation blockage by performing simple two-layer model calculations assuming conical shapes. An outer cone represented the radiative characteristics of the fire and an inner cone represented the vapor dome of pyrolysis gases. The assumption of a homogeneous flame failed to capture the observed trends in heat fluxes. However, the two-layer model calculations were found to be very sensitive to the adopted soot concentrations and soot temperatures in the flame as well as to the vapor dome. Measurements in very large pool fires also show significant gradients in the radiative heat fluxes to the pool surface, which are likely to result in significant gradients in the fuel vaporization rates within the pool [11].

In Fig. 4, the mean surface emissive power for many hydrocarbon pool fires is seen to decrease with increasing pool diameter due to smoke obscuration. Although a systematic methodology to reliably address this phenomenon is not yet available, some explanations have been proposed. The vapor dome of large fires may contain pyrolyzed fuel vapors which are at moderate temperatures relative to the reaction zone. Poor mixing and/or the slow entrainment of this stream with the air stream may result in the formation of long-lived, fuel-rich eddies that contain unoxidized fuel [12]. The smaller fluid strain rates associated with this process can reduce the diffusion rates, giving the fuel more time to pyrolyze and to form larger soot particles (smoke) that take longer to oxidize.

Klassen and Gore [4] measured transient emission and absorption properties in pool fires of different fuels and sizes (maximum diameter of 1 m). They observed a relatively cold layer of soot particles near the fuel surface. Comparing their absorption and emission measurements, they showed that a large portion of the soot particles were at relatively low temperatures and did not contribute to emission. Therefore, it is important to understand both the chemical phenomena which lead to the formation of soot, and the local transport phenomena which determine

the distributions of soot and soot temperature within a flame. The local soot concentration results from a time evolved history of local production and oxidation as well as convective and diffusive (thermophoretic) transport processes [13]. In fact, in laminar diffusion flames, the peak soot concentrations have been found to be slightly offset from the location of peak temperature [14]. This phenomenon is shown in Fig. 5 for a laminar C_2H_2 diffusion flame above a burner with a 12 mm × 96 mm fuel slot.

The local radiant emission from a flame is linearly dependent on the soot concentration and is dependent on temperature to the fourth power. The effective emissive power at the flame surface is the integral of the local emissive power multiplied by the transmissivity to the surface and corresponds to an emission temperature that is intermediate to the maximum flame temperature (~1,960 K) and the temperature at the position of maximum soot concentration (~1,640 K). Hence, knowledge of the temperature and soot volume fraction distributions is critical in calculating the effective flame temperature across flame fronts. In pool fires, similar effects occur on a macroscopic level due to the shielding of the flame core by the cooler, external soot layers and at a microscopic level as a consequence of the soot radiation from flamelets in the combustion zone.

The maximum heat flux is normally used to calculate safe separation distances from fires using metrics on damage from radiation such as those provided in Fig. 6: heat flux that causes pain to exposed humans, yields skin burns, or ignites wood for different times of exposure. Maximum tolerable heat fluxes can be established for different assumed times of exposure. Soot obscuration of radiation from fires will result in an overestimation of heat flux if flame temperature is assumed to be independent of diameter. This error will result in a conservatively safe distance of separation.
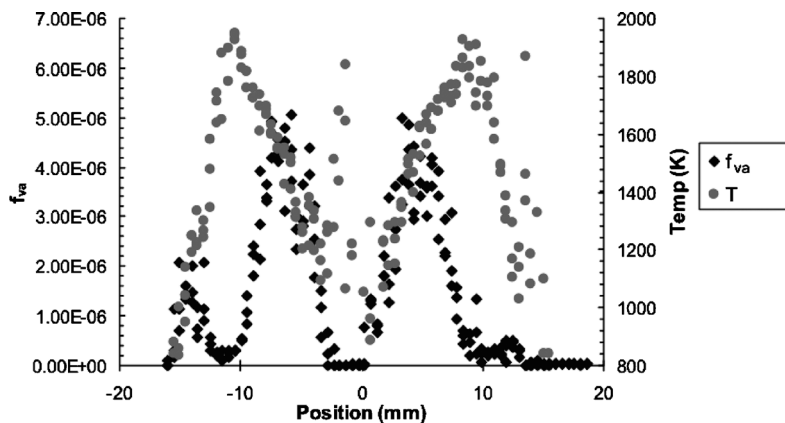

Figure 5: Radial profiles of soot concentration and temperature at an axial height of 7.14 mm in a laminar C_2H_2 diffusion flame (Fig. 27 of ref. [14]).
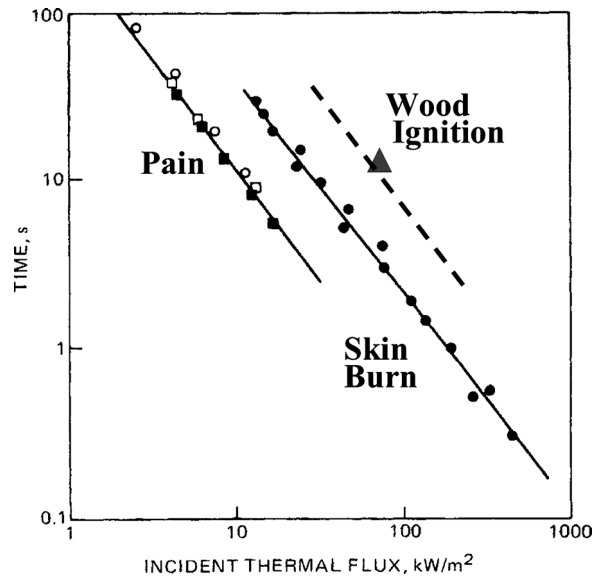
Figure 6: Skin exposure times to different heat fluxes that result in pain or burns, and flux needed to ignite wood (adapted from [8]).

For certain problems, however, overestimation of the heat flux may underestimate the fire hazard. This is particularly true when containers of high energy materials are exposed to radiation. An example of how lower heat fluxes can lead to greater hazards is shown in Fig. 7, where time to explosion of containers of the explosive PBX is plotted as a function of heat flux to the container surface. As expected, the time to explosion increases as heat flux decreases. However, at low heat flux rates, the intensity of the explosion increases as shown by the inset figures of the remnants of the container for two heat flux levels. The violence of the explosion increases as the time to explosion increases. Indeed, it is well known in the explosives community that long heating times (e.g. slow cook-off) can lead to detonations since more of the explosive material is heated to the ignition temperature. In contrast, with fast heating times (e.g. fast cook-off) only a surface layer is heated to the ignition temperature. The problem of BLEVEs with LPG is influenced by the accumulation of energy in the storage tanks that leads to the greatly enhanced strength of the explosions that result. For these reasons, conservative estimates of heat flux are no longer adequate.

Fire modeling approaches more sophisticated than the homogeneous model are required to reliably address observed pool fire phenomena. These phenomena, including the effects of fuel type, smoke obscuration, relative locations of the flame front and of regions of high soot concentration, variation of local flame temperature, radiation blockage, and radiative feedback to the pool surface determine the radiative heat transfer to an embedded object [15, 16]. The past two decades
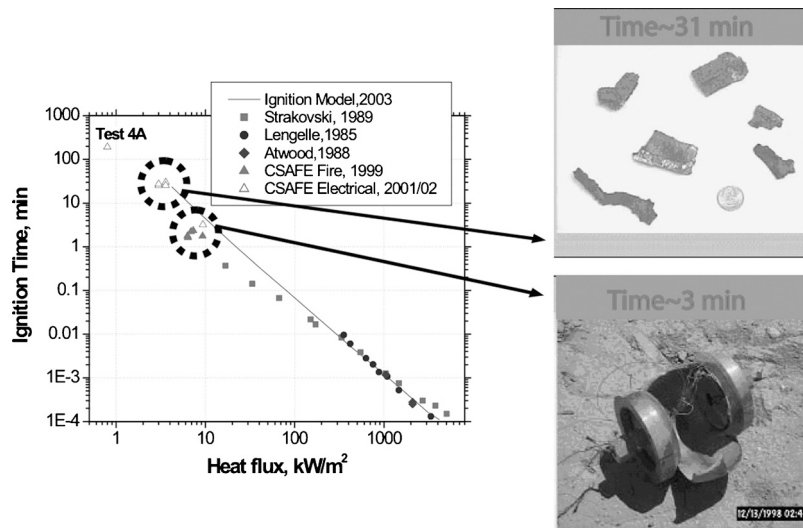
Figure 7: Time to ignition for containers of the explosive PBX as a function of heat flux, using both electrical heating and external flames. Inset figures show the recovered container fragments at two heating rates.

have seen an increasing use of CFD-based models to study fire phenomena. The progress that has been made will be discussed in the remainder of this chapter.

3 V&V as a foundation for predicting heat transfer to embedded objects in pool fires

The goal of this chapter is to present a physically-based method for predicting the potential hazard of an explosive device immersed in or near a pool fire of transportation fuel. To accomplish this goal, CFD-based computational tools that capture the relevant physical processes associated with the fire and the heat-up of the explosive device are employed.

To move toward predictivity with these computational tools, we choose a methodology based on the V&V principles set forth by Oberkampf and Trucano [17]. Verification is the process of determining whether or not the mathematical models are implemented into computer code as the programmer intended, independent of the model's physics. Validation determines how well the computer model matches the physical world. The process of V&V is cyclical as shown in Fig. 8, involving development of the conceptual model, verification of the model implementation, validation of the physical results, and evaluation of the conceptual model. Certification of the computer code for predictive use and quantification of error in the prediction involves the two-way coupling between the various stages of the V&V cycle.
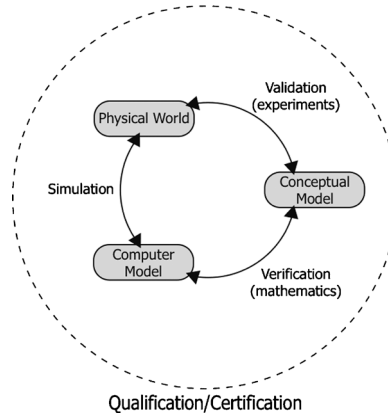
Figure 8: Connectivity between verification, validation, simulation, and certification (adapted from [18]).

3.1 V&V hierarchy

A key tool in the V&V methodology is the construction of a V&V hierarchy. The apex of the hierarchy is the specific intended use of the simulation tool, i.e. the full system to be simulated. The remainder of the hierarchy is composed of several levels of decreasing technical complexity: subsystem cases, benchmark cases, coupled problems, unit level problems, and molecular processes. As one moves down the hierarchy, the quantity and quality of data increases and the experimental uncertainties decrease.

At the highest level of the hierarchy, data are directly applicable to the intended use of the model but limited in scope and accuracy and often qualitative in nature. The subsystem case level is the decomposition of the overall system into simpler systems. Data with high experimental uncertainties are generally available for subsystem cases. The third level consists of benchmark cases, in which detailed experimental data from simplified but fully coupled problems are available for comparison. Coupled problems at the fourth level consist of two or more unit problems coupled together. Data available at this level include standard numerical solutions to simple problems and experimental data for coupled systems. The unit problems at the fifth level consist of isolated physical models. These models are validated as stand-alone problems with highly accurate numerical and experimental data. The lowest level in the hierarchy, molecular processes, further divides the unit problem into its fundamental components. The high fidelity data available at the unit problem level is also available at this level.

A V&V hierarchy is constructed for heat transfer to explosive objects embedded in transportation fuel pool fires with V&V activities from the molecular processes level to the full system level as seen in Fig. 9. Some of these activities are
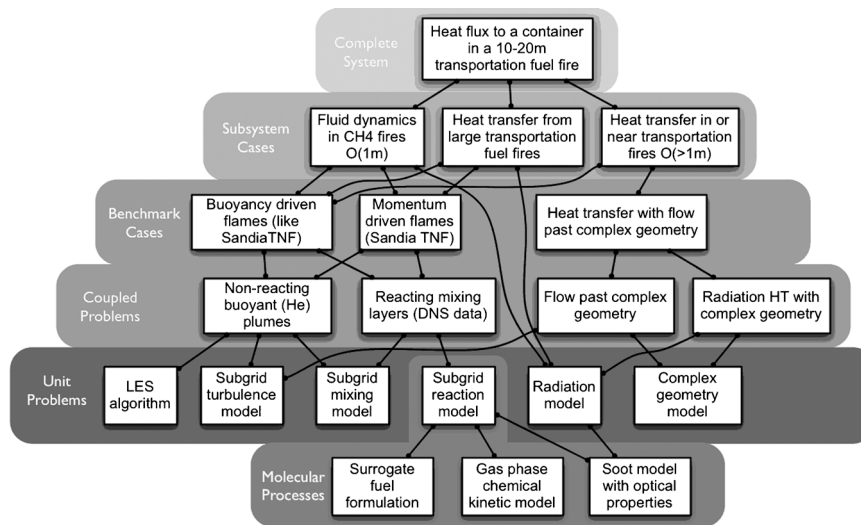
Figure 9: V&V hierarchy for simulations of heat flux to an object embedded in a transportation fuel pool fire.

highlighted in subsequent sections to demonstrate this hierarchal approach in moving toward predictivity. With one exception, the boxes at each level represent cases where experimental data sets have been identified in the context of the intended use of the simulation tool. The one exception is the 'buoyancy driven flames' box at the benchmark level; the desired experimental data for this box is unavailable.

3.2 Validation metric

Validation of computed results in simulation science has generally consisted of comparing in graphical manner form (e.g. a two-dimensional plot) data extracted from a simulation or set of simulations with measured observables from an experiment or set of experiments. Based on such a graphical comparison, a person may declare that the computer model is 'validated', 'invalidated', or 'requires improvement'. However, as pointed out by Oberkampf and Barone [19], these statements are qualitative in nature, leaving conclusions to the discretion of the observer. This potential for widely varying conclusions creates the need for a non-biased measurement, or metric, for determining the 'level of agreement' between experimental evidence and simulation results. The objective numerical values provided by the metric can then be used to formulate a value judgment of the comparison based on the level of risk one is willing to accept for the intended application. While the value judgment still requires the intervention of the biased human, the calculation of the metric does not

include a notion of 'quality', thus making the metric itself a non-biased participant in the validation process. Here, we briefly review a metric based on the use of statistical confidence intervals. This metric will be used in subsequent sections of this chapter to evaluate the level of agreement between LES data and experimentally measured data.

Given a set of two or more experimental observations ($n \geq 2$) and assuming that a population can be described by a normal distribution, a confidence interval for the true mean, μ, can be constructed using v degrees of freedom ($v = n - 1$) as

$$\mu \sim \left(\bar{x} - t_{\alpha/2,v} \cdot \frac{s}{\sqrt{n}}, \, \bar{x} + t_{\alpha/2,v} \cdot \frac{s}{\sqrt{n}} \right), \tag{5}$$

where x is the observed mean, s is the standard deviation, the level of confidence is $100(1 - \alpha)\%$, and $t_{\alpha/2,v}$ is the student-t distribution value based on the values of α and v.

Now, given a set of simulation and experimental data, one may construct an estimated error,

$$\tilde{E} = y_{\mathrm{m}} - \bar{y}_{\mathrm{e}}, \tag{6}$$

where y_{m} refers to the model (simulation) results and $\bar{y}_{\mathrm{e}}$ refers to the sample mean of the experimental results, e.g. the average of a set of n experimental observations. Note that $\tilde{E}$ is referred to as the 'estimated' error rather than the actual error because the true mean (μ) cannot be known given a small set of observations. Next, the *true* error is written as

$$E = y_{\mathrm{m}} - \mu. \tag{7}$$

Using the above definitions, the expression for the confidence interval for the true error is,

$$E \sim \left(\tilde{E} - t_{\alpha/2,v} \cdot \frac{s}{\sqrt{n}}, \, \tilde{E} + t_{\alpha/2,v} \cdot \frac{s}{\sqrt{n}} \right). \tag{8}$$

When computing metrics over a range of input variables such as spatial location, it is useful to reduce the collection of metrics to a single, global metric representing the system. The average relative error metric and the average relative confidence indicator, as described by Oberkampf and Barone [19], can be used to compute a global metric. The average relative error metric is defined by

$$\left| \frac{\tilde{E}}{y_{\mathrm{e}}} \right|_{\mathrm{ave}} = \frac{1}{(x_{\mathrm{u}} - x_1)} \int_{x_1}^{x_{\mathrm{u}}} \left| \frac{y_{\mathrm{m}}(x) - \bar{y}_{\mathrm{e}}(x)}{\bar{y}_{\mathrm{e}}(x)} \right| \mathrm{d}x, \tag{9}$$

where x_{u} and x_1 are the upper and lower bounds of the input variable. The relative average confidence indicator is given by

$$\left| \frac{CI}{\bar{y}_{\mathrm{e}}} \right| = \frac{t_{0.05,v}}{(x_{\mathrm{u}} - x_1)\sqrt{n}} \int_{x_1}^{x_u} \left| \frac{s(x)}{\bar{y}_{\mathrm{e}}(x)} \right| \mathrm{d}x, \tag{10}$$

The average relative error metric and the average relative confidence indicator provide a compact statement regarding the level of agreement, expressed as the global metric $\left|\tilde{E}/\overline{y}_e\right|_{ave} \pm \left|CI/\overline{y}_e\right|_{ave}$.

A few important points need to be considered relative to the metrics outlined here. First, the confidence intervals for the mean are not to be interpreted as traditional error bars on the simulation results; rather, they are the intervals in which the true error is estimated to lie with a given confidence. Second, for small numbers of experimental observations, the confidence intervals are made larger by increasing values of $t_{\alpha/2,v}$. It is thus advantageous to have multiple replications of a given experiment. Third, the confidence intervals speak to the quality of the experimental data and may lead one to seek out more and/or improved data sets. Finally, experimental observations are given supremacy over simulation results, as acknowledged by the sole use of experimental data in the construction of the confidence intervals.

4 Surrogate fuel formulation

The use of CFD to model heat flux to an explosive device in a transportation fuel pool fire raises the challenge of how to represent complex hydrocarbon fuels in computer simulations. One example of a transportation fuel is jet fuel (Jet-A or the military counterpart, JP-8), a mixture of hundreds of hydrocarbons that varies geographically and with time. It would be impractical to perform a simulation with such a complex mixture, even if the thermodynamics and detailed chemical kinetics for all the species in the mixture were available. Therefore, surrogate fuels, for which the necessary chemical and physical characteristics are known, must be developed. Different surrogates may be formulated for a given fuel depending upon the flame properties of interest. In this section, surrogate fuels are formulated for use in the simulation of a jet fuel pool fire, with particular interest in matching the burning rate and the heat transfer to objects immersed in, or in close proximity to, the fire. This work corresponds to the 'surrogate fuel formulation' box at the molecular processes level of the V&V hierarchy in Fig. 9.

The major categories of hydrocarbons in jet fuels are normal and branched alkanes, cyclo-alkanes, and aromatics. Several investigators have developed surrogates for jet fuels [20–24] for applications other than pool fires. For the application of a transportation fuel pool fire, each surrogate component is required to have known chemical kinetics, to be representative of a main class of hydrocarbons present in jet fuels, and to be relatively inexpensive. In order to match burning rate and heat transfer to embedded objects in a pool fire, the mixture of components must match the volatility of the fuel, the sooting tendency, and the heat of combustion, and must reproduce the flame characteristics of a Jet-A/JP-8 pool fire, preferably with a small number (<10) of components.

For the surrogate fuel study, the fuels tested included Jet-A, Norpar-15, and surrogates composed of various chemical reagents. Jet-A was acquired from the Salt Lake City Airport. Norpar-15, obtained from Exxon Chemicals, is a narrow-boiling

range mixture of hydrocarbons. Three surrogates, Hex-11, Hex-12, and Hex-25c, each composed of six compounds, were formulated to match volatility (the boiling point distribution) and sooting tendency (smoke point) of the Jet-A/JP-8 fuel. The compositions of all five fuels are listed in Table 1.

Other properties of the Jet-A and the calculated properties of the three surrogates are listed in Table 2. All three surrogates are similar to Jet-A in terms of volatility as reflected by the flash point and the average boiling point and in terms of smoke point.

Table 1: Fuel compositions (in mol. % except where noted).

Hex-11	Hex-12	Hex-25c	Norpar-15	Jet-A[a]
n-C$_8$, 3.5	n-C$_8$, 3.0	n-C$_8$. 5.0	n-C$_{14}$, 34.4	n-Paraffin, ≈28
n-C$_{12}$, 40.0	n-C$_{12}$, 30.0	n-C$_{12}$. 32.0	n-C$_{15}$, 49.0	
n-C$_{16}$, 5.0	n-C$_{16}$, 12.0		n-C$_{16}$, 13.5	
		HMN[b], 10.0	n-C$_{17}$+, 3.1	Branched paraffin, ≈29
Xylenes, 8.5	Xylenes, 15.0	n-HxBe[c], 23.0		Mono-aromatics, ≈18
Tetralin, 8.0	Tetralin, 13.0	PMH[d], 15.0		Di-aromatics, ≈2
Decalin, 35.0	Decalin, 27.0	Decalin, 15.0		Cycloparaffin, ≈20
				Nondetermined, ≈3
Sum, 100.0	100.0	100.0	100.0	100.0

[a] Approximate composition of Jet-A in this table is in wt. %.
[b] 2,2,4,4,6,8,8-heptamethylnonane.
[c] n-hexylbenzene.
[d] 2,2,4,6,6-pentamethylheptane.

Table 2: Properties of Jet-A and surrogate fuels.

Properties	Jet-A	Hex-11	Hex-12	Hex-25c
Smoke point (mm)	24.5	28.7	23.1	24.0
TSI[a]	26.7	17.6	22.1	20.3
MW (g/mol)	173.5[b]	151.5	152.2	166.5
VABP[c] (°C)	220.2	211.1	215.7	209.5
Flash point (°C)	40.9	40.3	41.3	39.0
Latent heat[d] (kJ/kg)	254.6	280.4	281.8	253.8
Combustion heat (MJ/kg)	44.9	44.5	44.6	44.6

[a]TSI is the threshold soot index. It is defined based on the smoke point such that its value ranges from 0 (least sooting) to 100 (most sooting).
[b]MW (molecular weight) of Jet-A is estimated using the API empirical equation.
[c]VABP is the volumetric average boiling point. It is the mean of the 10%, 30%, 50%, 70%, and 90% recovery temperatures determined in ASTM D86.
[d]Latent heat is estimated at VABP.

4.1 Validation of surrogate formulation

The ability of the surrogate formulations to match the burning rates and heat fluxes in Jet-A/JP-8 pool fires was tested by burning the jet fuel and its surrogates in a round steel pan, 0.3 m in diameter and 0.1 m deep, placed 0.5 m above the ground. The tests were conducted in an enclosure 5 m × 5 m in cross-section and 6 m high equipped with dampers to control air infiltration and an exhaust duct. Both transient and steady-state tests were performed. Transient tests consisted of igniting and burning a batch of fuel in the pan. Steady-state tests involved continual replacement of the fuel in the pan to maintain a constant fuel level. Flame heights, shape, and puffing frequency were determined with a high-speed video camera shooting at 2,000 frames/s and with real-time video. Total heat fluxes and radiative heat fluxes were measured with gas-purged, water-cooled radiometers. Details of the test conditions can be found in [25, 26].

In classical studies of hydrocarbon pool fires [27–29], the mode of pool fire combustion (e.g. transient or steady-state) is not always stated. The tests described here indicate that the combustion mode plays a significant role in the measured fuel properties of interest.

4.2 Burning rates and heat fluxes at steady state

In the steady-state experiments, the liquid fuel density was assumed to be constant throughout the test. Gas chromatograph (GC) spectra of fuel samples taken from the burning pan show that Jet-A samples did not change in composition over time.

Instantaneous volumetric burning rates were calculated and averaged over a time interval of 60 s. The results for Jet-A are plotted in Fig. 10 as a function of time. For this experiment, the steady-state burning rate of 2.07×10^{-3} m/min (0.0278 kg/m^2 s) is reached 24 min after ignition.

For liquid pools greater than 0.2 m in diameter, the mass burning rate (m'', kg/m^2 s) can be predicted by

$$m'' = m''_\infty [1 - \exp(-k \cdot \beta \cdot d)] \tag{11}$$

where m''_∞ is the mass burning rate of an infinite diameter pool (kg/m^2 s), k is the extinction–absorption coefficient of the flame (1/m), β is the mean beam length corrector, and d is the pool diameter (m) [30]. As there are no reported constants for Jet-A pool fires, values of m''_∞ and $k \cdot \beta$ for kerosene are used (0.039 kg/m^2 s and 3.5 m^{-1}, respectively) [28]. From eqn (11), the computed mass burning rate for Jet-A is 0.0258 kg/m^2 s (1.91×10^{-3} m/min), which is close to the experimental value for Jet-A reported above and to the value of 1.9×10^{-3} m/min reported for a 30 cm kerosene pool fire [1, 27].

Results from Hex-12 and Norpar-15 tests are also plotted in Fig. 10 for comparison. The steady-state regression rates for Hex-12 and Norpar-15 are 1.90 and 0.96×10^{-3} m/min, respectively. The time required for Hex-12 to reach steady state in this configuration is approximately 24 min.
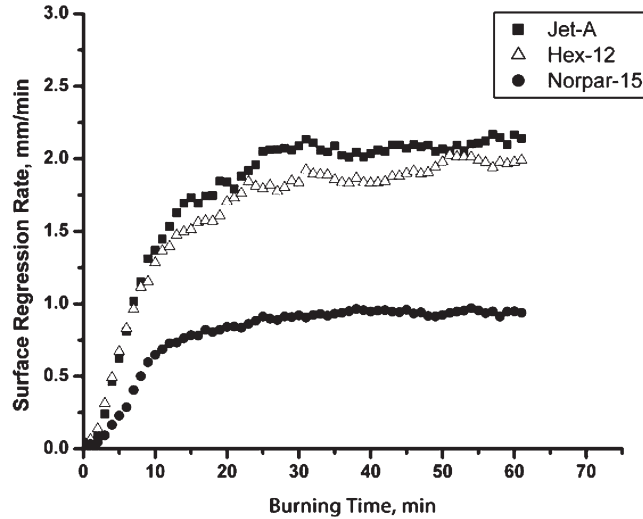
Figure 10: Continuous feed, constant level 30 cm diameter pool fire surface regression rate profile.

For the intended use of heat transfer to an explosive device, a key measure for the surrogate is its ability to yield radiation intensities that match those from a Jet-A flame. Real time heat flux measurements are shown in Fig. 11 for Jet-A and Hex-12 flames. These measurements were taken at a height of 0.20 m above the fuel surface and 0.40 m from the center of the pan. About 20 min after ignition, the radiative heat flux reached a relatively constant value of 10.9 kW/m^2 for Jet-A and 11.4 kW/m^2 for Hex-12. The average radiative heat flux for Norpar-15 was 5.8 kW/m^2.

4.3 Burning rates and heat fluxes for transient burning

In a typical pool fire, a fixed quantity of fuel is ignited and burned to completion. Due to the complex mixture of hydrocarbons present in Jet-A/JP-8, transient behavior is observed for many of the key physical and chemical parameters. Lighter hydrocarbons are expected to vaporize and burn preferentially such that during the later stages of the fire, the fuel should be enriched in residual heavy hydrocarbons. The transient experiment was conducted by filling the pan with fresh fuel, then turning off the feed system and allowing the fuel to burn to completion. The decreasing fuel level as a function of time, used to compute the surface regression rate, was measured using an optical level sensor [25].

The surface regression rate of Jet-A in transient tests is shown in Fig. 12. The surface regression rate increases rapidly up to 10 min and reaches a peak value of 1.84×10^{-3} m/min at 11 min. This peak value is close to the burning rate obtained in the steady-state tests. The rate falls off rapidly over the range of 12–35 min and then decreases more slowly from 40–80 min until the end of burning. The Jet-A
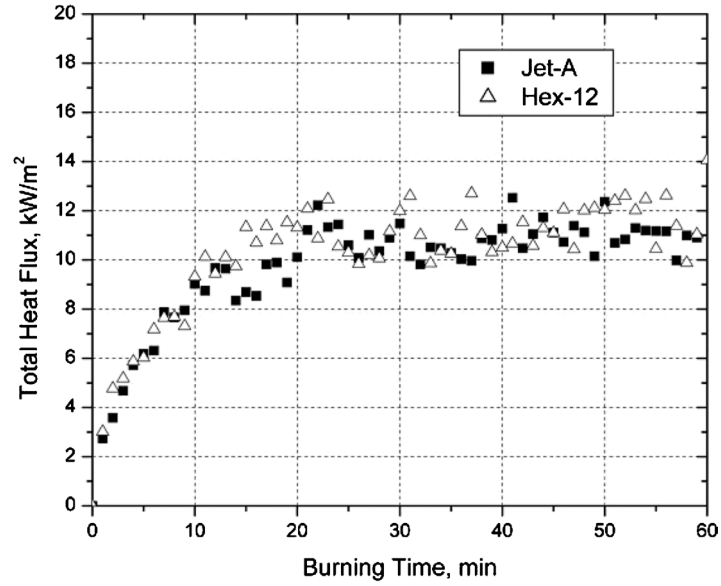
Figure 11: Radiative heat flux measurements from 30 cm diameter pool, continuous feed, constant fuel level experiments.
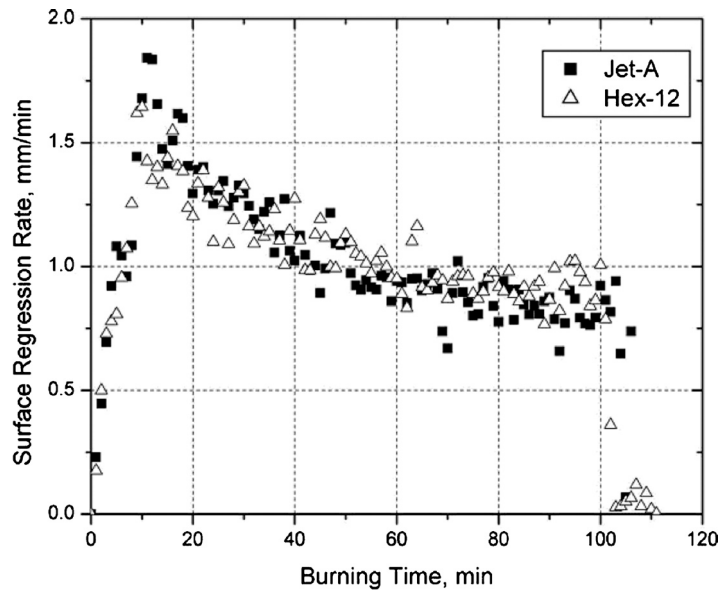

Figure 12: Transient surface regression rate profile for 30 cm diameter pool fire.

burning rate profile is successfully simulated by the surrogate fuel Hex-12 as shown in Fig. 12. The peak burning rate of Hex-12, 1.64×10^{-3} m/min, is slightly lower than that of Jet-A. The average burning rate for Hex-12 is 0.77×10^{-3} m/min, slightly lower than the average of 0.82×10^{-3} m/min for Jet-A.

Two explanations have been proposed for the high burning rate soon after ignition [31]. First, in the initial burning stage, there is no heat loss to the edges of the fuel pan and the entire amount of heat transferred back from the flame to the pool surface can contribute to fuel vaporization. Second, light components burn much faster initially, and the burning rate decreases after these species are depleted [28, 29].

The issue of whether the high initial burning rate is due to intense thermal feedback or to compositional variation was addressed by conducting transient burning experiments with Norpar-15, which is composed primarily of normal alkanes with 14–16 carbons (>99.8%) as shown in Table 1. After an initial transient, the surface regression rate is relatively constant, which supports the view that the initial high boiling rate for Jet-A (and its surrogates) is due to compositional change. Further confirmation was provided by the agreement of the mean fuel regression rate for Norpar-15 in the transient and steady state (Fig. 10) experiments. The radiant heat flux from the flame to the surroundings was consistent with the change in burning rate as well [25]. Finally, direct evidence of compositional change over time was demonstrated by GC analysis of Jet-A samples taken from the fuel pan [25].

4.4 Effect on fuel composition changes on sooting propensity

The composition changes described above are expected to lead to a continuous change in smoke point. Based on an ASTM D86 distillation test [32] of the Hex-12 surrogate, smoke points were calculated at different stages of volume loss and the results are plotted in Fig. 13. In addition, smoke points were measured on samples taken in a transient pool fire at different percentages of fuel volume consumption. Smoke points for Hex-12 increase with increasing volume loss for samples from both pool fire tests and distillation tests because the soot-promoting components (xylenes, tetralin, and decalin) are more volatile than n-dodecane and n-cetane. By the end of a burn, the residual surrogate fuel is nearly pure n-cetane and reaches its highest smoke point. In contrast, the smoke point of Jet-A decreases slowly with increasing burn-off/boil-off. This decrease is believed to be related to the wide spectrum of aromatics in actual jet fuel, as suggested in the detailed hydrocarbon analysis for Jet-A [33]. The existence of high molecular weight, high boiling point, and high sooting index naphthalenes and benzo-cycloalkanes in the actual fuel helps to maintain the smoke point relatively constant through low and intermediate percentages of fuel consumption with a slight decreasing trend at high percentages of fuel consumption.

4.5 Improved surrogate formulation

Due to the challenges associated with matching sooting propensity of Jet-A over its entire boiling range (or lifetime of a transient pool fire), a more chemically
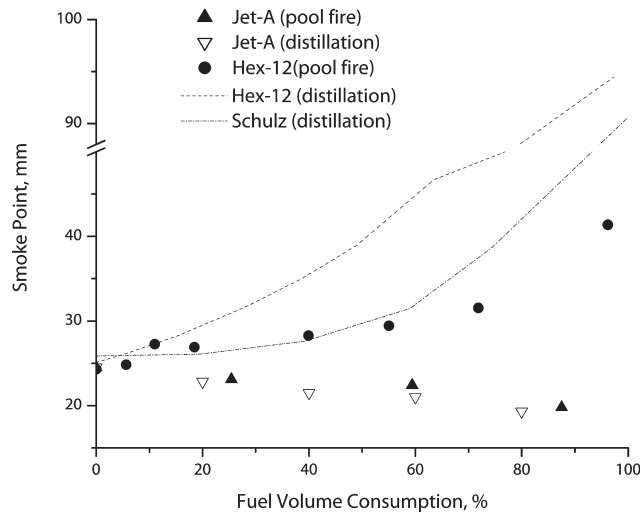
Figure 13: Smoke point variation as a function of volume of fuel burned (or distilled) for jet fuel and surrogates.

complex surrogate is required. The method of structural group contributions was adapted to the formulation of surrogates [25] and was used to provide a more chemically accurate description of the fuel [26]. The method is a significant improvement over previous approaches as it does not require any experimental procedures or information on fuel properties. However, the molecular structure of the fuel molecules must be determined.

The improved surrogate, Hex-25c, consists of six species. Its composition is given in Table 1, while its physical properties are given in Table 2. A comparison of the smoke point of Hex-25c with that of Jet-A is shown in Fig. 13, where it is evident that the new surrogate provides significant improvement in smoke point performance over the Hex-12 surrogate, particularly in the later stages of fuel consumption.

5 Chemical kinetics for soot production from JP-8

Two other areas of major research activity at the molecular processes level are the kinetic modeling of the gas and the solid (soot) phases. Kinetic modeling of surrogate fuels requires mechanisms and chemical kinetics for the major components of the surrogate [20–24, 34, 35]. Although the kinetic mechanisms are still under development, considerable success has been achieved by various research groups in matching experimental results. In general, these reaction mechanisms are tuned to meet specific objectives. For example, one focus area in engine modeling is ignition, which is influenced by chemical kinetics at low temperatures.

For the purpose of calculating heat transfer to embedded objects in pool fires, soot formation, which is strongly dependent on soot precursors derived from acetylene

and benzene, must be predicted. The following section describes kinetics that have been optimized to predict benzene and acetylene in premixed flames. The resulting mechanism is called the Utah Surrogate mechanism [36].

5.1 Utah Surrogate mechanism

A schematic representation for soot formation, adapted from Bockhorn [37], is shown in Fig. 14. The initial steps are the ignition and consumption of the surrogate mixture, which is driven by reactions with H, O, and OH radicals (with contributions from HO_2 in the ignition zone). The larger paraffinic fuel molecules decompose and cascade down to the smaller aliphatic and olefinic molecules. The key pathway to soot is the formation of benzene and then polycyclic aromatic hydrocarbons (PAH), which are the building blocks of the first particles. Acetylene is important because it is the major contributor to soot mass addition and it participates in the H-abstraction-ACetylene-Addition (HACA) mechanism [38] that leads to the growth of PAH and soot. Reaction mechanisms that address the steps shown in Fig. 14 are large, involving hundreds of chemical species and thousands of chemical reactions [22–24, 36–41].

The Utah Surrogate mechanism is formulated from detailed sub-models of *n*-butane, *n*-hexane, *n*-heptane, *n*-decane, *n*-dodecane, *n*-tetradecane, and *n*-hexadecane;
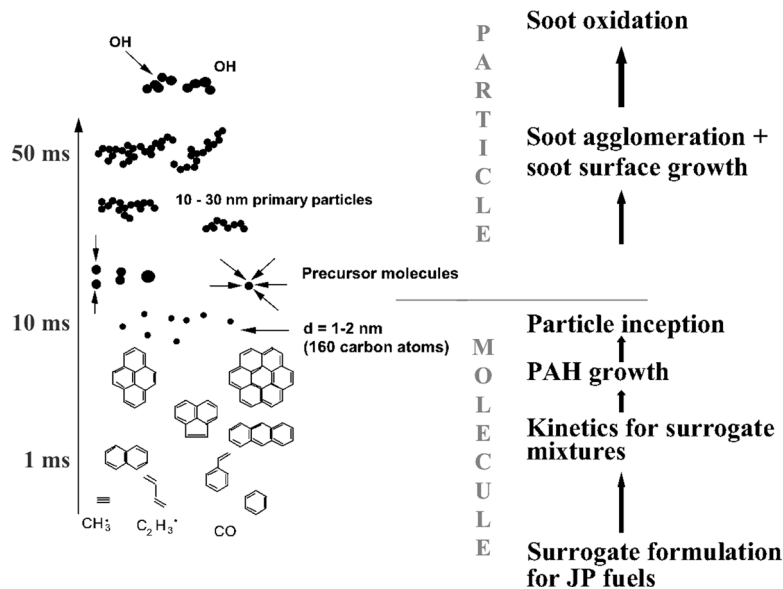

Figure 14: Schematic representation of sequential steps for soot formation and burn out (adapted from [37]).

semi-detailed sub-models of *i*-butane, *i*-pentane, *n*-pentane, 2,4-dimethyl pentane, *i*-octane, 2,2,3,3-tetramethyl butane, cyclohexane, methyl cyclohexane, tetralin, 2-methyl 1-butene, and 3-methyl 2-pentene; and aromatics that include benzene, toluene, and xylenes. The mechanism is available as supplemental material provided to the Combustion Institute in support of the publication by Zhang *et al.* [36]. The mechanism can be used to predict the fuel consumption and major combustion products for jet fuels that are comprised of mixtures of *n*-paraffins, *i*-paraffins, cyclo-paraffins, aromatics, and alkyl-substituted aromatics. Jet fuel composition can vary widely, depending upon the crude oil being refined and the refining procedures used. For example, aromatic content varies from 11% to 26%.

The mechanism was built on the following foundation:

- Marinov–Westbrook–Pitz hydrogen model [42]
- Hwang *et al.* [43] and Miller *et al.* [44] acetylene oxidation models
- Wang and Frenklach acetylene reaction set with vinylic and aromatic radicals [45]
- Marinov and Malte ethylene oxidation sub-model [46]
- Tsang propane and propene chemical kinetics [47, 48]
- Pitz and Westbrook *n*-butane sub-model [49]
- Miller and Melius benzene formation sub-model [50]
- Emdee–Brezinsky–Glassman toluene and benzene oxidation sub-model [51]
- Vovelle and coworkers *n*-heptane decomposition model [52]
- Pitsch *i*-octane decomposition model [53]

New submodels were added for a number of *n*-paraffins (C_5, C_6, C_{10}, C_{12}, C_{16}), a number of iso-paraffins (*i*-C_4, *i*-C_5, *i*-C_6, 2,2,3,3,-tetramethyl-C_4), cyclohexane, methyl cyclohexane, butadiene, and 3-methyl 2-pentene.

The mechanism is able to model a wide range of surrogates. It has been optimized for atmospheric conditions, flame studies, and soot precursors. Its ability to model the concentration of acetylene in flames of common components of surrogates, as well as a kerosene flame, is shown in Fig. 15, where results for acetylene concentration as a function of height above the burner are presented. In Fig. 15 the results for acetylene concentration as a function of height above the burner are presented for fuel rich flames of acetylene (C_2H_2, low pressure for Westmoreland and atmospheric pressure for Bockhorn), methane (CH_4), ethylene (C_2H_4), *n*-heptane (nC_7), and kerosene and for a stoichiometric *n*-heptane flame ($nC_{7,10}$). The conditions for the flames are given in Table 3. Kinetic model predictions for the pure component fuels and for kerosene using a surrogate formulation are shown by the solid lines. The agreement with the data shows the progress that is being made in the development of kinetic models with predictive capabilities. Nevertheless, a validation metric has not been applied to this analysis, so quantitative information is not available. Similar comparisons for benzene concentration can be found in [36].

5.2 Soot formation and oxidation

The Utah Surrogate mechanism provides the gas phase reactions up to the point of particle inception, as shown in Fig. 14. Several soot models are available that can
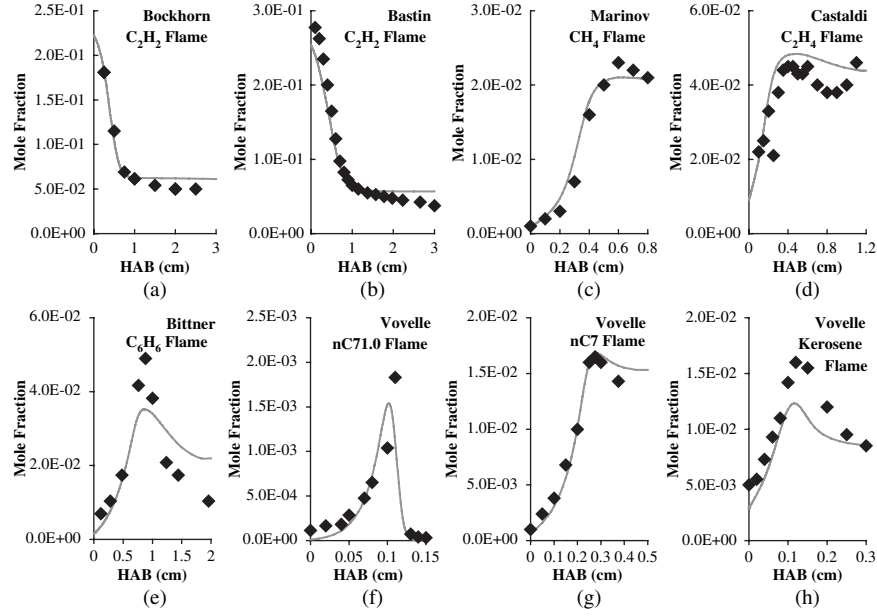
Figure 15: Comparison of concentrations of acetylene simulated using the Utah Surrogate mechanism with experimental results reported by different authors (see Table 3 for experimental conditions): (a) atmospheric pressure fuel rich flames of acetylene (C_2H_2), (b) low pressure fuel rich flames of C_2H_2, (c) fuel rich flames of methane (CH_4), (d) fuel rich flames of ethylene (C_2H_4), (e) fuel rich flames of benzene (C_6H_6), (f) stoichiometric flames of n-heptane ($nC_{71.0}$), (g) fuel rich flames of n-heptane (nC_7), and (h) fuel rich flames of kerosene.

Table 3: Experimental conditions for premixed flames in Fig. 15.

Author	Fuel	Inert Ar (%)	C/O	P (torr)	Flow rate (g/(cm^2 s))	Reference
Marinov	CH_4	0.453	0.626	760	7.19×10^{-2}	[54]
Westmoreland	C_2H_2	0.05	0.959	20	1.58×10^{-2}	[55]
Bastin	C_2H_2	0.45	1.00	19.5	3.46×10^{-2}	[56]
Bockhorn	C_2H_2	0.55	1.103	90	3.43×10^{-2}	[57]
Harris	C_2H_4	0.656	0.92	760	1.12×10^{-1}	[58]
Castaldi	C_2H_4	0.578	1.02	760	7.21×10^{-2}	[59]
Bittner	C_6H_6	0.3	0.717	20	2.19×10^{-2}	[60]
Ciajolo	C_6H_6	0.752[a]	0.72	760	5.07×10^{-2}	[61]
Vovelle	C_7H_{16}	0.73[a]	0.605	760	6.50×10^{-2}	[62]
Vovelle	i-C_8H_{18}	0.682[a]	0.608	760	5.56×10^{-2}	[62]
Vovelle	$C_{10}H_{22}$	0.682[a]	0.558	760	6.68×10^{-2}	[34]
Vovelle	Kerosene	0.684[a]	$\phi = 1.7$	760	7.96×10^{-2}	[34]

[a]N_2 is used the inert rather than Ar.

provide the transition from the soot precursor molecules to soot. Four classes of models utilized in order of increasing complexity are:

- Empirical models like that of Sarofim and Hottel [63] represent a combination of soot formation and destruction. Such models account for some of the major factors affecting soot contributions to radiative absorption and emission: temperature, stoichiometric ratio, and fuel type. With empirical models, a certain fraction of the fuel is converted to soot under fuel rich conditions, but no soot persists in a fuel lean environment.
- The Lindstedt model [39] has four steps: nucleation, surface growth, oxidation, and coagulation. The nucleation is assumed to be an activated process that is proportional to acetylene concentration and which yields nuclei of a specified size, with 100 carbon atoms being suggested. Surface growth is proportional to acetylene concentration and has a rate parameter fitted to literature rates. Soot is assumed to be oxidized by O_2 with a rate constant fitted to data so as to allow for the role of OH. Coagulation is calculated using the standard equations for aerosol dynamics.
- The HACA mechanism, built on the two-step process of activation of an aromatic molecule by hydrogen abstraction followed by acetylene addition, leads to both molecular weight growth and cyclization [40]. Lumping mechanisms have been developed for the PAH growth using generic rates for the different classes of reactions including acetylene addition, hydrogen abstraction, and reactions with OH and O_2. Soot nucleation is assumed to occur by the dimerization of two PAHs. Although dimers of all PAH combinations can be included, it is common to use pyrene. Soot formation and growth are calculated using moment methods, with allowance for nucleation, coagulation, and surface growth, as well as oxidation reactions. The implementation of this method by Appel *et al.* [38] has found widespread use.
- Sectional models treat the soot simultaneously with the chemical kinetics by assigning large PAH particles and soot particles to bins that have a range of carbon numbers. The transition from gas phase chemistry to particle chemistry is achieved by assigning a bin with a given carbon number as the smallest particle size. One implementation of the sectional model [41] has the smallest bin for mass numbers of 201–400, with an H/C ratio of 0.5, corresponding to a particle size of 0.85 nm. The mass limits are approximately doubled for each sequential bin; the largest of 20 bins corresponds to mass numbers of 105–210 million, an H/C ratio of 0.125, and a particle size of 68 nm. Bins are assumed to react with all other bins and with gas phase molecules. The first four bins are considered to be large PAHs and the bins from 5 to 20 to be soot particles. Soot can also be oxidized, primarily by reactions with OH, O, and O_2. The rates of oxidation for most flame conditions are dominated by the reaction with OH. The rate of reaction is proportional to the collision rate of the OH with the soot surface with approximately 13% of the collisions [64] leading to the consumption of soot by the stoichiometric reaction C + OH = CO + H.

6 Use of LES methods for pool fires

A major challenge in applying CFD to fires is the wide range of continuum length scales and their corresponding time scales that characterize the fire physics in large diameter (>1 m) fires. For example, important physical time and length scales range from molecular $O(10^{-9}$ s, 10^{-10} m$)$ to scales that are observable with the naked eye $O(1$ s, 1 m$)$. This range of time and length scales prohibits the use of fully resolved, three-dimensional, direct numerical simulation (DNS) techniques. Additionally, transportation fuel fires often involve complicated interactions with the environment such as the highly unsteady processes of fluid/structure interaction, wind effects, and flame spread across fuels.

Given current modeling options and the importance of unsteady effects in transportation fires, LES is the prime candidate for modeling such fires. Compared to the traditional Reynolds averaging (RANS) approach, LES captures the unsteady effects of pool fires more accurately by resolving the large length and time scales that are responsible for controlling the dynamics of the fire [65]. In fact, LES is emerging as the prevailing methodology for studying fires due to its ability to render realistic, time-resolved flows of gases, heat, and smoke throughout a domain [66].

An LES approach was employed by Schmidt *et al.* [67] and Kang *et al.* [68] to study turbulence structure in medium scale methanol pool fires. In both these efforts, reasonably good agreement was obtained for the mean velocity and temperature fields and their fluctuations. Xin *et al.* [69] conducted a study of a 7.1 cm methane pool fire that quantitatively reproduced the average scalars and velocities. Numerical simulations of pool fires employing the LES approach and accounting for participating media radiative heat transfer have also been demonstrated [70–72]. In the fire protection engineering community, a widely used fire simulation tool is Fire Dynamics Simulator (FDS), developed by McGrattan *et al.* at NIST [73, 74]. This LES-based tool has been used in residential and industrial fire reconstructions and in the design of fire protection systems.

In the V&V hierarchy (Fig. 9), the low-Mach LES algorithm and the subgrid turbulence closure are identified as two of the unit problems. The LES algorithm is composed of the numerical differencing scheme and a solution method (algorithm) for solving the filtered set of governing equations. The subgrid turbulence model is the set of approximations that 'close' the set of filtered equations, effectively modeling the unresolved turbulent fluctuations. The LES algorithm and subgrid turbulence closure are closely coupled, but by separating the two, one can independently address modeling choices that affect simulation results for the intended use of the LES tool.

6.1 LES equations

The essential governing equations, written in finite volume form, include the mass balance, momentum balance, mixture fraction balance, and energy balance

equations. Using a bold-face symbol to represent a vector quantity, the equations are:

1. The mass balance,

$$\int_V \frac{\partial \rho}{\partial t} dV + \oint_S \rho \mathbf{u} \cdot d\mathbf{S} = 0, \tag{12}$$

where ρ is density and $\mathbf{u}$ is the velocity vector.

2. The momentum balance,

$$\int_V \frac{\partial \rho \mathbf{u}}{\partial t} dV + \oint_S \rho \mathbf{u}\mathbf{u} \cdot d\mathbf{S} = \oint_S \tau \cdot d\mathbf{S} - \int_V \nabla p dV + \int_V \rho \mathbf{g} dV, \tag{13}$$

where τ is the deviatoric stress tensor defined as $\tau_{ij} = 2\mu S_{ij} - \frac{2}{3}\mu \frac{\partial u_k}{\partial x_k}\delta_{ij}$ and the symmetric stress tensor $S_{ij} = \frac{1}{2}\left(\frac{\partial u_i}{\partial x_j} + \frac{\partial u_j}{\partial x_i}\right)$. The second isotropic term in τ_{ij} is absorbed into the pressure projection for the current low-Mach scheme. Also in eqn (13), $\mathbf{g}$ is the gravitational body force and p is the pressure.

3. The mixture fraction balance,

$$\int_V \frac{\partial \rho f}{\partial t} dV + \oint_S \rho \mathbf{u} f \cdot d\mathbf{S} = \oint_S D\nabla f \cdot d\mathbf{S}, \tag{14}$$

where f is the mixture fraction and a Fick's law form of the diffusion term assuming equal diffusivities results in a single diffusion coefficient, D.

4. The thermal energy balance,

$$\int_V \frac{\partial \rho h}{\partial t} dV + \oint_S \rho \mathbf{u} h \cdot d\mathbf{S} = \oint_S k\nabla h \cdot d\mathbf{S} - \oint_S q \cdot d\mathbf{S}, \tag{15}$$

where h is the sum of the chemical plus sensible enthalpy and q is the radiative flux. A Fourier's law form of the conduction term is used with a diffusion coefficient, k, and the pressure term is neglected.

Now, consider a control volume, V, with surface area S. Because the equations will be solved on a computational grid, one can assume that the control volume has N faces, where unique faces are identified with their index k. The discussion is further simplified by only considering cubic volumes of length h.

Given the cubic control volume, a surface-filtered field for a variable ϕ is defined as $\overline{\phi}^{(j)}(\mathbf{x})$, where the variable is filtered on a plane in the x_j orthogonal direction. Then, for any surface k, the field is sampled at the face-centered location. For example, if $j = 1$, the surface-filtered quantity is

$$\overline{\phi}^{2d,(1)}(\mathbf{x}) = \frac{1}{h^2} \int_{x_2-h/2}^{x_2+h/2} \int_{x_3-h/2}^{x_3+h/2} \phi(\mathbf{x}') dx_2' dx_3'. \tag{16}$$

The volume average follows as

$$\overline{\phi}^{3d}(\mathbf{x}) = \frac{1}{h^3} \int_{x_1-h/2}^{x_1+h/2} \int_{x_2-h/2}^{x_2+h/2} \int_{x_3-h/2}^{x_3+h/2} \phi(\mathbf{x}')dx_1'dx_2'dx_3'. \tag{17}$$

The bars over the variable ϕ are labeled with superscripts '2d' and '3d' to distinguish between the two filters. Pope [75] identifies the proceeding definitions as using the 'anisotropic box' filter kernel where the resultant variables are simply averages over the interval $x_j - \frac{1}{2}h < x_j' < x_j + \frac{1}{2}h$.

For convenience in isolating density in the filtered equations, a Favre-filtered quantity is defined for an arbitrary variable φ as

$$\tilde{\varphi}^{2d} \equiv \frac{\overline{\rho\varphi}^{2d}}{\overline{\rho}^{2d}}, \tag{18}$$

and

$$\tilde{\varphi}^{3d} \equiv \frac{\overline{\rho\varphi}^{3d}}{\overline{\rho}^{3d}}. \tag{19}$$

This convention of explicitly defining the 2d and 3d filters is different than what is commonly observed in the literature, where the filtered equations are derived from finite difference equations rather than finite volume equations. Thus, using $\overline{\rho}^{2d}$ and $\overline{\rho}^{3d}$ in eqns (18) and (19) for surface and volume filtered densities, respectively, is appropriate for the present discussion.

These definitions for filtered quantities are applied to the integral forms of the governing equations to obtain the Favre-filtered LES equations. Nevertheless, there are terms in the Favre-filtered equations that cannot be solved. These include the surface-filtered convection of momentum $\widetilde{u_i u_j}^{2d}$, the surface-filtered convection of mixture fraction, $\widetilde{u_j f}^{2d}$, and the surface-filtered convection of enthalpy, $\widetilde{u_j h}^{2d}$.

For the filtered momentum product, $\overline{\rho}^{2d}\,\widetilde{u_i u_j}^{2d}$, a subgrid stress tensor is defined as,

$$\tau_{ij}^{sgs} = \widetilde{u_i u_j}^{2d} - \tilde{u}_i^{2d}\tilde{u}_j^{2d}. \tag{20}$$

Similarly, subgrid diffusion terms are defined for mixture fraction and enthalpy,

$$\mathcal{J}^f = \widetilde{u_j f}^{2d} - \tilde{u}_j^{2d}\tilde{f}^{2d}, \tag{21}$$

$$\mathcal{J}^h = \widetilde{u_j h}^{2d} - \tilde{u}_j^{2d}\tilde{h}^{2d}. \tag{22}$$

Using these definitions, the final forms of the Favre-filtered equations are

1. The filtered mass balance,

$$\frac{d}{dt}(\tilde{\rho}^{3d}) + \frac{S_k}{V}n_{kj}(\overline{\rho}^{2d}\tilde{u}_j^{2d}) = 0. \tag{23}$$

2. The filtered momentum balance,

$$\frac{\mathrm{d}}{\mathrm{d}t}(\overline{\rho}^{3\mathrm{d}}\tilde{u}_i^{3\mathrm{d}}) = \frac{S_k}{V}n_{kj}(-\overline{\rho}^{2\mathrm{d}}\tilde{u}_i^{2\mathrm{d}}\tilde{u}_j^{2\mathrm{d}} + \overline{\tau}_{ij}^{2\mathrm{d}} + \tau_{ij}^{\mathrm{sgs}} - \overline{p}^{2\mathrm{d}}\delta_{ij}) + \overline{\rho}^{3\mathrm{d}}g_i. \qquad (24)$$

3. The filtered mixture fraction balance,

$$\frac{\mathrm{d}}{\mathrm{d}t}(\overline{\rho}^{3\mathrm{d}}\tilde{f}^{3\mathrm{d}}) = \frac{S_k}{V}n_{kj}(-\overline{\rho}^{2\mathrm{d}}\tilde{u}_j^{2\mathrm{d}}\tilde{f}^{2\mathrm{d}} + D\nabla\overline{f}^{2\mathrm{d}} + \mathcal{J}^f). \qquad (25)$$

4. The filtered thermal energy balance,

$$\frac{\mathrm{d}}{\mathrm{d}t}(\overline{\rho}^{3\mathrm{d}}\tilde{h}^{3\mathrm{d}}) = \frac{S_k}{V}n_{kj}(-\overline{\rho}^{2\mathrm{d}}\tilde{u}_j^{2\mathrm{d}}\tilde{h}^{2\mathrm{d}} + k\nabla\overline{h}^{2\mathrm{d}} - \overline{q}^{2\mathrm{d}} + \mathcal{J}^h). \qquad (26)$$

The subgrid momentum stress, τ_{ij}^{sgs}, the subgrid mixture fraction dissipation, $\mathcal{J}^f$, and the subgrid enthalpy dissipation, $\mathcal{J}^h$, contain the unresolved or subgrid action of the turbulence on the transported quantities. Since these terms arise from definitions, models are introduced to include the subgrid effects that they represent. These models are discussed next.

6.2 Subgrid turbulence models

Invoking an 'eddy-viscosity' modeling concept, the subgrid transport due to turbulent advection is treated as an enhanced diffusion term for the unclosed terms listed above. That is, the subgrid mixture fraction dissipation and subgrid enthalpy dissipation are respectively written as,

$$\mathcal{J}^f = D_t \frac{\partial\overline{f}^{2\mathrm{d}}}{\partial x_j}, \qquad (27)$$

and

$$\mathcal{J}^h = k_t \frac{\partial\overline{h}^{2\mathrm{d}}}{\partial x_j}. \qquad (28)$$

To model D_t and k_t, constant turbulent Schmidt (Sc_t) number,

$$Sc_t = \frac{1}{\rho}\frac{\mu_t}{D_t}, \qquad (29)$$

and Prandtl (Pr_t) number,

$$Pr_t = \frac{1}{\rho}\frac{\mu_t}{k_t}, \qquad (30)$$

are assumed, where μ_t is a turbulent viscosity. Following Pitsch and Steiner [76], the values of the turbulent Schmidt and Prandtl numbers are taken as $Sc_t = Pr_t = 0.4$, which is consistent with a unity Lewis number assumption.

For the subgrid momentum stress tensor, τ_{ij}^{sgs}, two common LES turbulence clo-sure models are the constant coefficient Smagorinsky model [77] and the dynamic coefficient Smagorinsky model [78]. As with the scalar subgrid modeling terms, the eddy viscosity model is again invoked for τ_{ij}^{sgs}, which is approximated by

$$\tau_{ij}^{\text{sgs}} \approx -2\nu_t \overline{S}_{ij} = -2(C_s\Delta)^2 \,|\,\overline{S}\,|\,\overline{S}_{ij}, \tag{31}$$

where Δ is the filter width, ν_t is the eddy viscosity, and $|\,\overline{S}\,| \equiv (2\overline{S}_{ij}\overline{S}_{ij})^{1/2}$. For the Smagorinsky model, $C_s \approx 2$ depending on the filter type, numerical method, and flow configuration [75].

For the dynamic Smagorinsky model, C_s is computed by taking a least squares approach to determine the length scale [79],

$$(C_s\Delta)^2 = \frac{\left\langle \mathcal{L}_{ij} M_{ij} \right\rangle}{\left\langle M_{ij} M_{ij} \right\rangle}, \tag{32}$$

where

$$\mathcal{L}_{ij} = 2(C_s\Delta)^2 \widehat{|\,\overline{S}\,|\,\overline{S}_{ij}} - 2(C_s\hat{\Delta})^2 \,|\,\overline{S}\,|\,\overline{S}_{ij}, \tag{33}$$

and

$$M_{ij} \equiv 2(\widehat{|\,\overline{S}\,|\,\overline{S}_{ij}} - \alpha^2 \,|\,\overline{S}\,|\,\overline{S}_{ij}). \tag{34}$$

The hat defines an explicit test filter and the angular brackets in eqn (32) conceptu-ally represent an averaging over a homogeneous region of space that, experience has shown, is necessary for stability. Experience has also shown that averaging over the test filter width is adequate. The filter width ratio, $\alpha = \hat{\Delta}/\Delta$, is usually taken to be 2.

6.3 LES algorithm

The set of filtered equations (eqns (23)–(26)) are discretized in space and time and solved on a staggered, finite volume mesh. The staggering scheme consists of four offset grids. One grid stores the scalar quantities and the remaining three grids store each component of the velocity vector. The velocity components are situated so that the center of their control volume is located on the face centers of the scalar grid in their respective direction.

The staggered arrangement is advantageous for computing low-Mach LES react-ing flows. First, since a pressure projection algorithm is used, the velocities are exactly projected without interpolation error because the location of the pressure gradient coincides directly with the location of the velocity storage location. Second, Morinishi *et al.* [80] showed that kinetic energy is exactly conserved on a staggered grid when using a central differencing scheme on the convection and diffusion terms without a subgrid model. Having a spatial scheme that conserves kinetic energy is

advantageous because it limits artificial dissipation that arises from the differencing scheme. These conservation properties make the staggered grid a prime choice for LES reacting flow simulations.

For the spatial discretization of the LES scalar equations, flux limiting and upwind schemes for the convection operator are used. These schemes are advantageous for ensuring that scalar values remain bounded. For the momentum equation, a central differencing scheme for the convection operator is used. All diffusion terms are computed with a second-order approximation of the gradient.

When computing the 2d surface filtered field on the faces of the control volume, one is forced to use an interpolation from the 3d volume filtered field. This approximation is tolerated because computing the 2d surface field is not possible with the given grid scheme.

An explicit time stepping scheme is chosen. A general, multistep explicit update for a variable, ϕ, may be written as,

$$\phi^0 = \phi^n,$$

$$\phi^{(i)} = V \sum_{k=0}^{m-1} (\alpha_{i,k} \phi^{(k)} + \Delta t \beta_{i,k} L(\phi^{(k)})), \quad i = 1,...,m, \tag{35}$$

$$\phi^{(m)} = \phi^{n+1},$$

where n is the time level, m is the substep between n and $n + 1$, α and β are integration coefficients, and L is a linearization operator on the convective flux and source terms.

The time step is limited by

$$\Delta t \le c \Delta t_{\text{F.E.}}, \tag{36}$$

where $\Delta t_{\text{F.E.}}$ is the forward-Euler time step limited by the Courant–Friedrichs–Levy condition and c is a constant less than or equal to 1.

A higher order multistep method is derived by letting $m > 1$ and choosing appropriate constants for α and β. For this study, two-step and three-step, strong stability preserving (SSP) coefficients were chosen from Gottlieb *et al.* [81]. The coefficients for SSP-RK 2 and SSP-RK 3 are optimal in the sense that the scheme is stable when $c = 1$ if the forward-Euler time step is stable for hyperbolic problems. In practice, for the Navier–Stokes equations, the value of c is taken to be less than 1.

Choosing an explicit time stepping scheme, rather than an implicit one, creates a challenge for solving the set of equations. The density at the $n + 1$ time step, which is required to determine the cardinal variables, requires an estimation. Taking the estimated density for $\overline{\rho}^{n+1}$ to be $\overline{\rho}^*$, the estimation can be as simple as $\overline{\rho}^* = \overline{\rho}^n$. Note that the 2d and 3d filter distinction is dropped for the remainder of this discussion for the sake of simplicity. Another procedure includes predicting a value for $\overline{\rho}^*$ from performing a forward-Euler step in time as,

$$\overline{\rho}^* = \overline{\rho}^n - \Delta t \frac{S_k}{V} n_{kj}^{(\overline{\rho}\widetilde{u}_j)}. \tag{37}$$

Ideally, one would like to know $\overline{\rho}^{n+1}$, but ρ is a function of the same variables that are being updated in time, namely the mixture fraction, f, and enthalpy, h. This quandary, a result of the explicit time stepping method, will not be resolved for variable density flows without using a fully implicit method. Explicit methods, however, can be advantageous, especially for large scale parallel computations. Specifically, load balancing is easier and more efficient with explicit methods because the amount of work required per processor is readily determined a priori. Explicit methods are also easier to code into a computer and to debug. For these reasons, the current algorithm discussion is limited to explicit methods.

The explicit algorithm for solving the set of filtered equations is shown in Algorithm 1.

Algorithm 1 Explicit LES algorithm.

    for $t = t_{min}\ldots t_{max}$ **do**
      for $RK_{step} = 1\ldots N$ **do**
        Solve for scalars products $(\overline{\rho}\tilde{f})^{n+1}$ and $(\overline{\rho}\tilde{h})^{n+1}$.
        Estimate $\overline{\rho}* = \overline{\rho}^{n+1}$ from eqn (37)
        if $\overline{\rho}* < \overline{\rho}_{min}$ or $\overline{\rho}* > \overline{\rho}_{max}$ **then**
          $\overline{\rho}* = \overline{\rho}^{n}$
        end if
        Compute $\tilde{f}^{n+1} = (\overline{\rho}\tilde{f})^{n+1} / \overline{\rho}*$ and $\tilde{h}^{n+1} = (\overline{\rho}\tilde{h})^{n+1} / \overline{\rho}*$
        Compute $\overline{\rho}^{n+1} = f(\tilde{f}^{n+1}, \tilde{h}^{n+1})$
        Compute $\tilde{\mathbf{u}}*$, the unprojected velocities
        Perform RK averaging if needed
        Compute correct pressure from pressure Poisson equation
        Project velocities with correct pressure to get $\tilde{\mathbf{u}}^{n+1}$
      end for
    end for

6.4 Large scale, parallel computing with LES

LES is computationally intensive because it resolves a relatively large set of spatial and temporal scales, it is computationally intensive. An LES algorithm can be implemented in a serial code, but the underlying models must be simplified and/or lower resolution cases must be considered. To understand the interactions between a transportation fuel fire and embedded objects, all relevant scales require resolution. For example, the relevant scales for turbulence/chemistry interactions can be orders of magnitude smaller than the largest fire scales. Accounting for all these length and time scales requires massively parallel computations.

The LES fire simulation tool described above utilizes Uintah, a component-based visual problem solving environment (PSE) that provides a framework for large-scale parallelization of different applications [82–84]. Uintah was designed and

implemented to satisfy three goals: (1) to provide a general framework for massively parallel simulations of fluid and particle physics; (2) to facilitate both MPI- and thread-based parallelism; and (3) to allow scientists from outside the computer field to have an intuitive method for easily inserting their algorithms into a parallel framework without being bogged down by parallel programming details.

The integration of the LES fire simulation tool in the Uintah PSE required the development of reusable, physics-based components that could be used interchangeably and interact with other components. Examples of such components include a pressure solver, a momentum solver, a scalar solver, and a subgrid scale turbulence model. Also implemented in Uintah are components developed by third parties, specifically nonlinear and linear solvers designed for complex flow problems. Realistic fire simulations must account for relevant physical processes such as turbulent reacting flow, convective and radiative heat transfer, multiphase interactions, and fundamental gas-phase chemistry. Representations of these physical processes lead to very large sets of highly nonlinear, partial differential equations (PDEs); robust nonlinear and linear solvers on massively parallel platforms are required. Hence, two suites of nonlinear and linear scalable solvers for scientific applications modeled using PDEs, Portable Extensible Toolkit for Scientific Computation (PETSc) [85] and High Performance Preconditioners (HYPRE) [86], are interfaced with Uintah.

6.5 V&V studies of LES code/turbulence model

6.5.1 Verification using the method of manufactured solutions
Both analytical and manufactured solutions are frequently used as verification tools. Analytical solutions to the Navier−Stokes equations usually involve simple systems where parts of the equations are reasonably neglected. As a result, not all parts of the equation and the corresponding discretization scheme are fully tested when compared to analytical solutions. Manufactured solutions allow for arbitrary complexity in the solutions because they have no physical meaning, a manufactured solution, or a set of manufactured solutions, is created to verify all parts of the equation. When manufactured solutions are processed through the governing equations, the governing equation itself might not be satisfied, so an extra source term is added to account for the additional terms that arise from the manufactured solution. The method of manufactured solutions [87] is an extremely useful verification exercise for finding programming errors and ensuring expected behavior of the computer code.

The convective and diffusive spatial operators as well as the pressure correction algorithm are tested in two-dimensional planes by initializing the domain with a manufactured solution for velocity and pressure (added exponential term to manufactured solution in [88]),

$$u(x, y, t) = 1 - A \cdot \cos(x - t)\sin(y - t)\mathrm{e}^{-2vt}, \tag{38}$$

$$v(x, y, t) = 1 + A \cdot \sin(x - t)\cos(y - t)\mathrm{e}^{-2vt}, \tag{39}$$

$$p(x,y,t) = \frac{-A^2}{4}\left[\cos(2(x-t)) + \cos(2(y-t))\right]e^{-4vt}, \tag{40}$$

where A is the amplitude and v is the viscosity. Note that the velocity field satisfies the continuity equation, $\nabla \cdot U = 0$, for constant density.

To test the spatial discretization error, the advection/diffusion terms and the computed gradient of the pressure correction from the Poisson solve are evaluated at $t = 0$. Then, advection/diffusion terms and the correction gradient are compared to the exact solutions for each two-dimensional plane (x–y, x–z, y–z) in a three-dimensional Cartesian space. The total force vector on a fluid element is given by the sum of the individual components,

$$F^{\text{Total}} = F^{\text{a}} + F^{\text{d}} + F^{\nabla P}, \tag{41}$$

where F^{a} is the advective force, F^{d} is the diffusive force, and $F^{\nabla P}$ is the pressure force. Decomposing the force vector into its various components is useful for identifying programming error in individual force components, but here we consider only the total force vector.

The total normalized error for the force components is measured as

$$\text{Normalized error} = \frac{\left\| F_e^{\text{Total}} - F^{\text{Total}} \right\|}{\left\| F_e^{\text{Total}} \right\|}, \tag{42}$$

where the subscript e is the force computed from the manufactured solution. Fig. 16 shows that the normalized error from the spatial discretization decreases at a second-order rate with increasing mesh resolution for each two-dimensional plane.
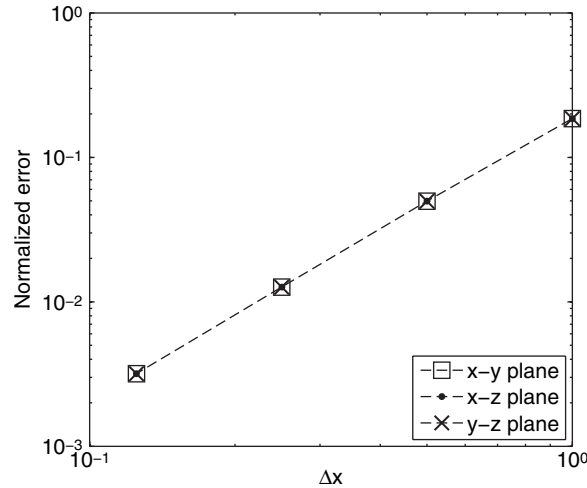

Figure 16: Total error convergence using a manufactured solution for the spatial operators. Each two-dimensional plane in the three-dimensional Cartesian space is tested and shows second-order behavior.

6.5.2 Verification and validation with Compte-Bellot and Corrsin data

Further verification of the LES code and validation of the constant coefficient and dynamic Smagorinsky subgrid turbulence models is achieved by initializing the computational domain with the experimental data of Compte-Bellot and Corrsin [89] and then marching the solution in time using the second-order SSP-RK time stepping scheme on a 32^3 periodic mesh. The curves generated by this technique are displayed in Fig. 17. The straight solid line represents a simulation with no subgrid turbulence model and no molecular viscosity. This line stays nearly level, with only a slight increase in kinetic energy that is added from the time stepping scheme (the energy characteristics of the SSP-RK algorithm are discussed in [90]). This result verifies that the simulation is free from numerical dissipation. The other two curves show the kinetic energy behavior obtained from the constant coefficient Smagorinsky and dynamic coefficient Smagorinsky models. Both curves generally follow the kinetic energy decay in the data, an expected result for isotropic turbulence.

6.5.3 Validation of subgrid turbulence models

Additional turbulence model validation is performed using buoyant helium plume data from the 'coupled problem' level of the V&V hierarchy. This 'coupled problem' combines the effects of fluid flow and turbulence without the complications introduced by chemical reactions. The data set from the 1 m helium plume, taken in the FLAME facility at Sandia National Laboratories in Albuquerque, NM, includes time-averaged vertical velocity, horizontal velocity, and mixture fraction profiles as well as instantaneous values of these variables [91].
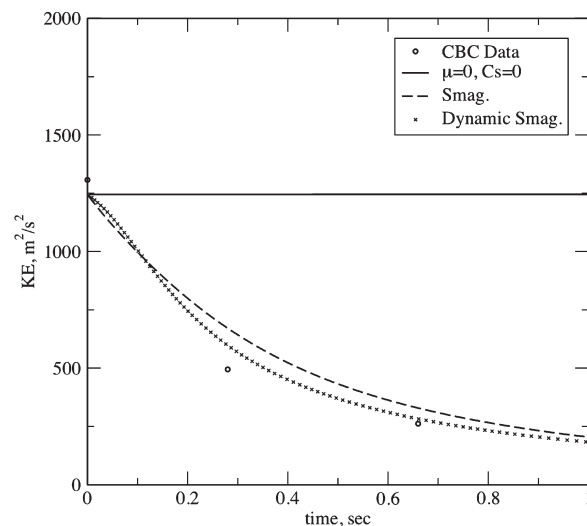

Figure 17: LES code verification and turbulence subgrid model validation. Kinetic energy is reported per unit mass.

Simulations of the 1 m helium plume were performed on a 3 m^3 computational domain using the LES code described above coupled with two types of dynamic turbulence models: the dynamic coefficient Smagorinsky model described above and a local dynamic model [92]. The purpose of the study was to determine the best turbulence model for the large buoyant plume. In the case of helium, it has been observed [93] that small Rayleigh–Taylor instabilities, on the order of 1.5 cm for a 1 m helium plume, may control the strength of the air entrainment. Failure to capture this effect leads to weak air entrainment and velocities that are too high in the centerline velocity field. Since proper mixing requires that the length scale of the Rayleigh–Taylor instability be captured on the mesh, a turbulence model that does not smear out the instability is preferred.

For the simulations, the turbulent Schmidt (Sc_t) and Prandtl (Pr_t) numbers were held constant at 0.4 (eqns (29) and (30)) and the filter width (Δ) was averaged over a grid volume,

$$\Delta = (\Delta x \Delta y \Delta z)^{1/3}. \tag{43}$$

Fig. 18 compares mixture fraction as a function of radial distance for the two turbulence models and three mesh resolutions at a height of 0.6 m above the inlet. The bands on the experimental data represent the 90% confidence interval constructed from the experimental data. While both models overpredict the helium centerline concentration, the local dynamic model appears to perform slightly better and to converge at a lower mesh resolution than the dynamic Smagorinsky model. However, global metric values (from eqns (9) and (10)) shown in Table 4 for the mixture fraction and streamwise (u) velocity components suggest that neither turbulence model provides a distinct advantage over the other at the finest resolution ($\Delta x = 1$ cm).
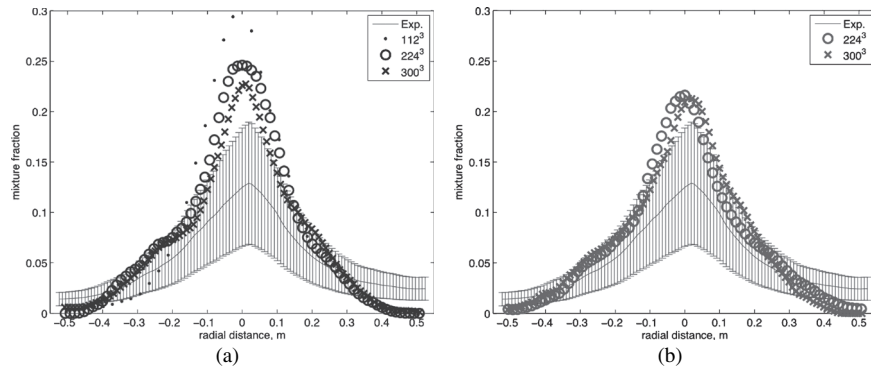

Figure 18: Profiles of the average mixture fraction as a function of radial distance at a height of 0.6 m above the inlet for (a) the dynamic Smagorinsky model and (b) the local dynamic model.

Table 4: Global average relative errors with the average relative confidence indicator for the streamwise (u) velocity and mixture fraction. All values are percentages.

	u velocity		Mixture fraction	
Resolution	Dynamic Smagorinsky	Local dynamic	Dynamic Smagorinsky	Local dynamic
112^3	25 ± 20	NA	91 ± 45	NA
224^3	18 ± 20	9 ± 20	64 ± 45	41 ± 45
300^3	11 ± 20	10 ± 20	47 ± 45	48 ± 45

Further investigation of the overprediction of the centerline helium concentration is ongoing and includes understanding the effects of the density prediction in the explicit scheme and of the scalar turbulent closure.

7 Combustion/reaction models

Detailed combustion modeling of turbulent flows is computationally prohibitive due to the wide range of time and length scales that are coupled through interactions between thermochemistry and fluid dynamics. The use of a detailed kinetic scheme to describe the chemistry requires the solution of a transport equation for $N_S - 1$ species where N_S is the total number of species. This requirement, coupled with the stiffness of the source terms in the transport equations, makes the computational load unmanageable for transportation fuel pool fires. Fortunately, the fluid dynamics length and time scales overlap with only a subset of the thermochemical time scales, so some degree of decoupling is possible. Indeed, a large class of combustion models relies on the assumption that many chemical time scales are significantly faster than the fluid dynamic scales of interest and can be decoupled. The entire thermochemical state is then represented by a small set of parameters called reaction variables.

This system representation by a small set of reaction variables is only valid when the thermochemical state of the system is well-approximated by a manifold in the lower-dimensional space defined by the reaction variables [94]. The concept of a low-dimensional manifold is best explained by considering different reaction trajectories in a high-dimensional state space. Due to fast reactions, these trajectories quickly relax to a low-dimensional attracting manifold governed by the slow reactions. Once the manifold is reached, all reaction trajectories move along the manifold toward equilibrium.

The ultimate goal of a manifold identification technique is to represent the chemical and molecular transport processes that control flame structure (the subgrid or microscale physics) in a macroscale simulation. This goal is achieved through parameterization of the state space (ρ, T, Y_1, Y_2,...,Y_S) described by the low-dimensional manifold. A transport equation is then solved on the computational mesh for each of

the parameters. A model for all other thermochemical variables as a function of the resolved scale parameters provides the bridge between the resolved and the unresolved scales in the simulation. This model is called a subgrid reaction model and is located at the unit problem level in Fig. 9.

7.1 Parameterization of a reacting system

The state of a single phase reacting system with N_S species requires $N_S + 1$ variables (e.g. $N_S - 1$ mass fractions, temperature, and pressure) to uniquely specify the thermochemical state, ϕ, of the system [95, 96]. The reaction model parameterizes ϕ by η, a vector of parameters (reaction variables) of size n, where $n < N_s + 1$. The reaction model then provides a unique mapping from η to ϕ, i.e. each ϕ_i is represented by an N_η-dimensional surface in η-space. Mathematically, the state relationship is written as

$$\phi(\rho, T, Y_1, Y_2, ..., Y_S) \approx \phi(\eta_1, \eta_2, ..., \eta_n) = \phi(\eta) \tag{44}$$

Given that the thermochemical state of the physical system is inherently $(N_S + 1)$-dimensional, a unique surface may not exist in the lower-dimensional space parameterized by η.

While parameterization of a low-dimensional manifold greatly simplifies the solution of a complex reacting flow by reducing the number of independent variables in the system, the choice of reaction variables is critical. The reaction variables should span both the resolved and subgrid time scales of interest and provide a reasonable representation of the subgrid scale reaction processes.

In combustion applications, mixture fraction, f, is widely used as a reaction variable. Mixture fraction is defined as the local ratio of the total mass originating from the fuel stream to the total mass originating from the fuel and the oxidizer streams. For describing nonpremixed systems, mixture fraction is an obvious choice for a reaction parameter since it represents the stoichiometry of the mixture. However, it does not provide any information about the intrinsic state of the system.

In the following sections, two different parameterizations are evaluated, one using DNS data [97–100] and the other using experimental data from the International Workshop on Measurement and Computation of Turbulent Nonpremixed Flames (TNF data) [101]. Both parameterizations use the concept of canonical reactors to account for the detailed chemical kinetics and subgrid transport processes.

7.2 Use of canonical reactors

The two components of a reaction model as defined here are the identification of an attracting manifold in thermochemical state space and the parameterization of that manifold. Three canonical reactor models are chosen for manifold extraction: an equilibrium model, a perfectly stirred reactor (PSR) model, and a steady laminar flamelet model (SLFM). Manifolds may also be extracted from other canonical reactors such as a premixed flame reactor, a laminar diffusion flame reactor, or

a reactor based on the one-dimensional turbulence model of Kerstein [102], but these reactors will not be discussed further in this chapter.

The equilibrium model is based on the assumption that the chemistry is infinitely fast and hence all chemical reactions are in equilibrium. This model ignores any effects of diffusion or of transient flame behavior. The present equilibrium calculations were performed with the CANTERA solver [103], which uses Gibbs free energy minimization to find the equilibrium state.

The PSR model is a mathematical approximation to a well-stirred reactor. A PSR Fortran code that predicts the steady-state temperature and species compositions [104, 105] was used to generate the results shown here. Since the PSR has a flow term the reaction trajectories account for chemical kinetics coupled to flow.

The SLFM model is a one-dimensional counterflow flame configuration utilizing a coordinate transformation from physical space to mixture fraction space [106]. This reaction model accounts for stoichiometry and diffusion simultaneously, by considering a one-dimensional coordinate in the flame-normal direction. The SLFM calculations were performed with a unity Lewis number assumption.

7.3 Progress variable parameterization

The progress variable parameterization is a two-variable reaction model based on the mixture fraction and η_{CO_2}, a progress variable derived from the CO_2 mass fraction. The model is generated by reparameterizing the solution to the flamelet equations by (f, η_{CO_2}) instead of the usual parameterization by (f, χ), where χ is the scalar dissipation. The advantage of the η_{CO_2} parameterization is that the effects of extinction may be incorporated; parameterization by (f, χ) does not capture extinction because the state variables are discontinuous with respect to χ at the steady extinction limit [107]. The flamelet solutions are then tabulated as functions of (f, η_{CO_2}), with η_{CO_2} defined as

$$\eta_{CO_2} = \frac{Y_{CO_2} - \beta}{\alpha - \beta},$$

(45)

where $\alpha = \max(Y_{CO_2} | f)$ and $\beta = \min(Y_{CO_2} | f)$.

7.3.1 Generation of DNS data
DNS data for reaction model validation were obtained from a DNS code that solves the compressible, reacting Navier–Stokes equations using eighth-order explicit finite-differences [108] with a fourth-order Runge–Kutta method in conjunction with a temporal error controller [109]. Mixture-averaged transport is employed, with transport coefficients calculated from the Chemkin transport package [110]. Further details, including initial and boundary conditions, can be found in [107].

DNS calculations of a spatially evolving, two-dimensional, turbulent $CO/H_2/N_2$–air jet flame were used in this parameterization analysis [107]. The fuel stream composition in mole % was 45%CO, 5%H_2, and 50% N_2 at 300 K and the oxidizer stream was air at 300 K. These streams yield a stoichiometric mixture fraction of

f_{st} = 0.437. The kinetic mechanism employed for CO/H$_2$ oxidation included 12 species and 33 reactions [111, 112]. The mean jet velocity was 50 m/s with a co-flow velocity of 1 m/s. The Reynolds number based on the fuel stream properties (jet width and jet velocity) was 4,600.

7.3.2 Validation of progress variable parameterization

Consider a set of reaction variables, η, used to parameterize the thermochemical state, ϕ, of the system. One may project a DNS data set into η-space and determine a mean surface that the DNS data occupies by $\langle \phi \mid \eta \rangle$, the average value of the state variables conditioned on a given set of values of the reaction variables. This concept is illustrated in Fig. 19, where the data points representing realizations of the temperature ($\phi = T$) from a DNS dataset are plotted against the mixture fraction ($\eta = f$). The thick solid line represents the conditional mean of T in mixture fraction space, $\langle T \mid f \rangle$, while the thick dashed line represents the temperature obtained if the system was in thermochemical equilibrium. The thin lines in Fig. 19 are explained below.

Given the projected data in η-space (points in Fig. 19) and the conditional mean (thick solid line in Fig. 19), the standard deviation of ϕ from its mean in η-space is expressed as

$$\sigma_{\phi_i} = \sqrt{\langle (\phi_i^{DNS} - \langle \phi_i^{DNS} \mid \eta \rangle)^2 \mid \eta \rangle}, \qquad (46)$$

where $\phi_i \mid \eta$ represents all values of the ith state variable which correspond to the given value η, and $\langle \, \rangle$ indicates an average. As there may be many points in physical
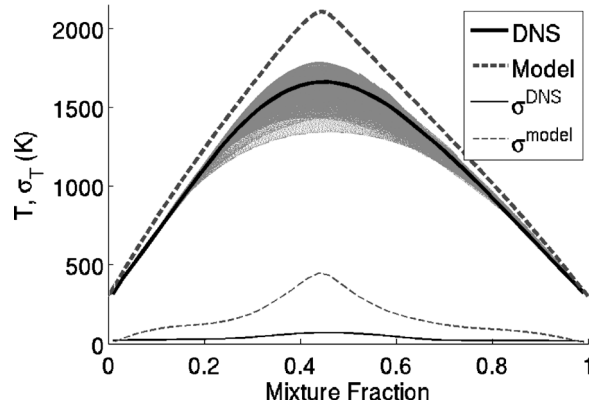

Figure 19: DNS results of CO/H$_2$/N$_2$–air jet flame showing temperature projected into mixture fraction space. DNS data is represented by points and the conditional mean by the thick solid line. Also shown is the equilibrium solution (thick dotted line).

space that have the same η, σ_{ϕ_i} provides a quantitative measure of the best possible performance a given model parameterized by η can achieve relative to the DNS data and is henceforth referred to as the ideal model performance.

The thin solid line in Fig. 19 shows σ_T as a function of f and provides a measure of the accuracy with which T is parameterized by f. The data deviates from an ideal model by approximately 70 K at $f = 0.43$, a 4% deviation.

The dashed line in Fig. 19 represents the temperature predicted by the equilibrium model, which is a unique function of the mixture fraction for an adiabatic system. The deviation of the DNS data from the surface defined by the model may be defined as

$$\sigma_{\phi_i}^* = \sqrt{\langle (\phi_i^{\mathrm{DNS}} \mid \eta - \phi_i^*(\eta))^2 \rangle},$$ (47)

where $\phi_i^{\mathrm{DNS}}|\eta$ is a realization of the DNS data conditioned on a specific value set of η, and $\phi_i^*(\eta)$ is the ith state variable as given by the model. The thin dashed line in Fig. 19 shows the deviation, σ_T^*, of the equilibrium-predicted temperature from the DNS data.

The actual model performance relative to the DNS data is measured by $\sigma_{\phi_i}^*$ from eqn (47). Thus, by comparing σ_{ϕ_i} and $\sigma_{\phi_i}^*$, a quantitative measure of the performance of the given model parameterized by η is obtained.

Fig. 20 shows the results of an (f, χ) parameterization of temperature for an ideal model generated from the DNS data as well as the SLFM reaction model. Comparing Figs. 19 and 20, it is clear that the addition of χ as a second parameter allows significantly better representation of the data than the one-parameter equilibrium model, with maximum errors of 3% and 9% for the ideal and SLFM models, respectively at f_{st}. However, the SLFM model does deviate from the ideal (f,χ) model at both low and high χ.

Fig. 21 shows the results of an $(f, \eta_{\mathrm{CO_2}})$ parameterization of temperature for the same DNS and SLFM reaction model data shown in Fig. 20. The progress variable parameterization of the SLFM reaction model performs nearly ideally across the entire range of $\eta_{\mathrm{CO_2}}$. In fact, ideal models based on an $(f, \eta_{\mathrm{CO_2}})$-parameterization are consistently able to represent the state variables better than ideal (f, χ)-parameterizations for this jet flame case.

7.4 Heat loss parameterization

The heat loss parameterization is a two-variable reaction model based on the mixture fraction f, and γ, a variable derived from enthalpy that represents fractional heat loss. It is defined as:

$$\gamma = \frac{h_{\mathrm{a}} - h}{\int_{T_{\mathrm{ref}}}^{T_{\mathrm{ad}}} c_p \mathrm{d}T} = \frac{h_{\mathrm{a}} - h}{h_{\mathrm{a}} - h_{\mathrm{a,ref}}}.$$ (48)

In eqn (48), h_{a} is the adiabatic enthalpy, h is the absolute enthalpy, T_{ref} is the reference temperature, T_{ad} is the adiabatic temperature, c_p is the mixture-averaged

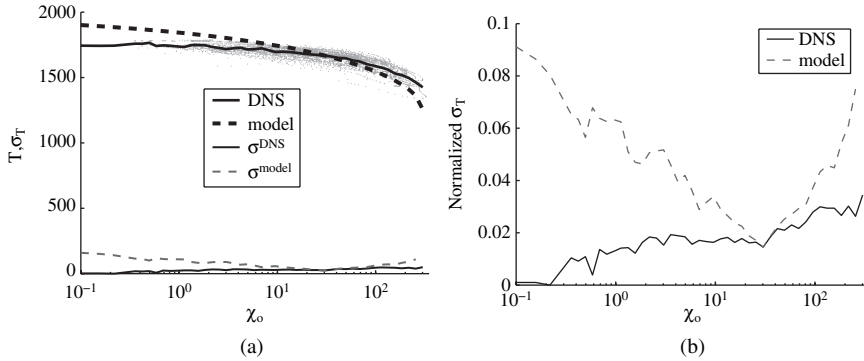Figure 20: Parameterization of temperature by (f, χ) for the $CO/H_2/N_2$–air jet flame case. Results for (a) temperature and conditional mean and (b) normalized conditional mean from an ideal model (DNS) and the SLFM model (model) are shown.
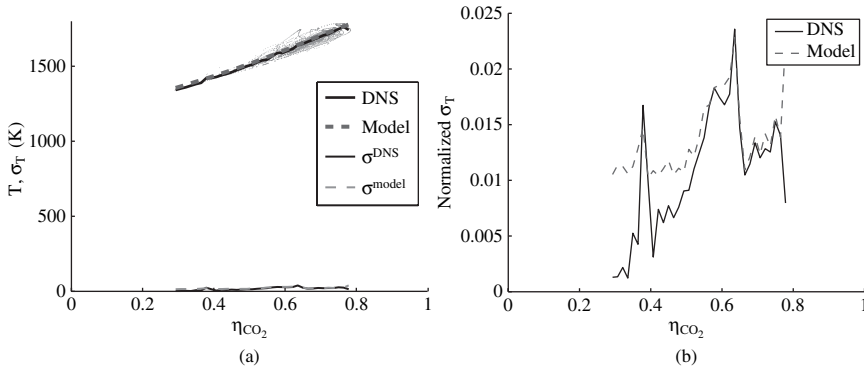

Figure 21: Parameterization of temperature by (f, η_{CO_2}) for the $CO/H_2/N_2$–air jet flame case. Results for (a) temperature and conditional mean and (b) normalized conditional mean from an ideal model (DNS) and the SLFM model (model) are shown.

specific heat from the adiabatic product composition, and $h_{a, ref}$ is the absolute enthalpy of adiabatic products at the reference temperature. The adiabatic enthalpy and temperature are the enthalpy and temperature which would exist if no energy were lost to the surroundings. The numerator is the residual enthalpy. The denominator normalizes the residual enthalpy by the sensible enthalpy of the system. When the heat loss is zero, the system is adiabatic. If heat loss is greater than zero, heat (energy) is lost from the system. If heat loss is less than zero, heat (energy) has entered the system. For unreacted fluid elements with mixture fractions near 0 or 1, the sensible enthalpy of the system is small. As a result, γ can become very large near the edges of mixture fraction space.

The inclusion of heat loss accounts for changes in the enthalpy of the system due to heat transfer phenomena such as radiation. By representing enthalpy changes with γ, enthalpy becomes quasi-linearly independent of mixture fraction. This representation also facilitates tabulation of reaction model results for implementation in a CFD code and allows the incorporation of local extinction in the constructed tables.

7.4.1 TNF data

Detailed measurements were taken of a methane jet [113, 114] with a fuel composition of 22.1% CH_4, 33.2% H_2 and 44.7% N_2 by volume. The co-flow consisted of air with 0.8% H_2O entering at 292 K. The stoichiometric mixture fraction was $f_{st} = 0.167$. Measurements of temperature and concentrations of N_2, O_2, CO, H_2, CO_2, H_2O, OH, CH_4 and NO were obtained. Axial profiles ($x/d = 2.5$ up to $x/d = 120$) and radial profiles ($x/d = 5, 10, 20, 40, 60, 80$) of mean and rms values, conditional statistics, and single shot data were taken. Typically, 800–1,000 samples were acquired at each location with uncertainties in the experimental measurements available in the listed references.

The experimental flame data was organized into bins of (f, γ). Heat loss was calculated at each data point using eqn (48). To compute the sensible enthalpy, the adiabatic composition was obtained from an adiabatic equilibrium calculation at a reference temperature of 273.15 K. Then, each data point was placed into a bin that was characterized by an (f, γ) pair of values. The validity of the parameterization proposed in eqn (44) is assessed using this TNF data table.

7.4.2 Validation of heat loss parameterization

In order to use an (f, γ) parameterization, heat loss must be present in the canonical reactor model. For the equilibrium model, heat loss was incorporated by varying the composition and enthalpy of the initial $CH_4/H_2/N_2$–air mixture. For the PSR reactor, model reactor solutions were obtained for a range of mixtures (defined by the inlet equivalence ratio) at various normalized heat loss values by including heat loss from the reactor in the calculation. The volume of the reactor for the $CH_4/H_2/N_2$–air case was 67.4 cm^3 and the residence time was specified as 0.003 s. For the SLFM model with a unity Lewis number assumption, the adiabatic profile for enthalpy is a line connecting the enthalpy of the fuel and oxidizer streams, a direct consequence of enthalpy being a conserved scalar. To incorporate heat loss effects into the SLFM reactor model, the heat loss as defined in eqn (48) was adopted. First, the adiabatic solution was computed followed by the computation of the denominator in eqn (48). Next, the enthalpy profile was computed given a constant value of heat loss. The species flamelet equations were then solved, with temperature computed from enthalpy and composition computed using a one-equation Newton's method. The maximum scalar dissipation rate was set at 20 s^{-1} since in buoyancy-driven flames, the scalar dissipation rate is low and does not vary much through the flow field.

The reaction model results presented here are based on the species, thermodynamics, and detailed kinetics found in the GRI3.0 scheme, but similar results could also be obtained using the surrogate JP-8 kinetic mechanism described in Section 5.

Figure 22 shows temperature and species concentrations conditioned on various values of heat loss and plotted in mixture fraction space for the $CH_4/H_2/N_2$ flame. While this flame was close to adiabatic conditions, a realizable heat loss ranging from −0.02 to 0.09 was identified [115]. These plots include the experimental data along with the results from the three canonical systems described previously. Qualitatively, the temperature manifold (Fig. 22(a)) and those of the major species, including CO_2 and H_2O (Fig. 22(b)), are well-represented by the PSR and SLFM reaction models [115]. Reasonable predictions for some minor species such as OH, seen in Fig. 22(c), are also achieved using the nonequilibrium models. The prediction of other minor species, including NO, could be improved with the addition of a third parameter.

With this (f,γ) parameterization, qualitative analysis reveals that the nonadiabatic equilibrium calculations match the experimental data only in the lean region;
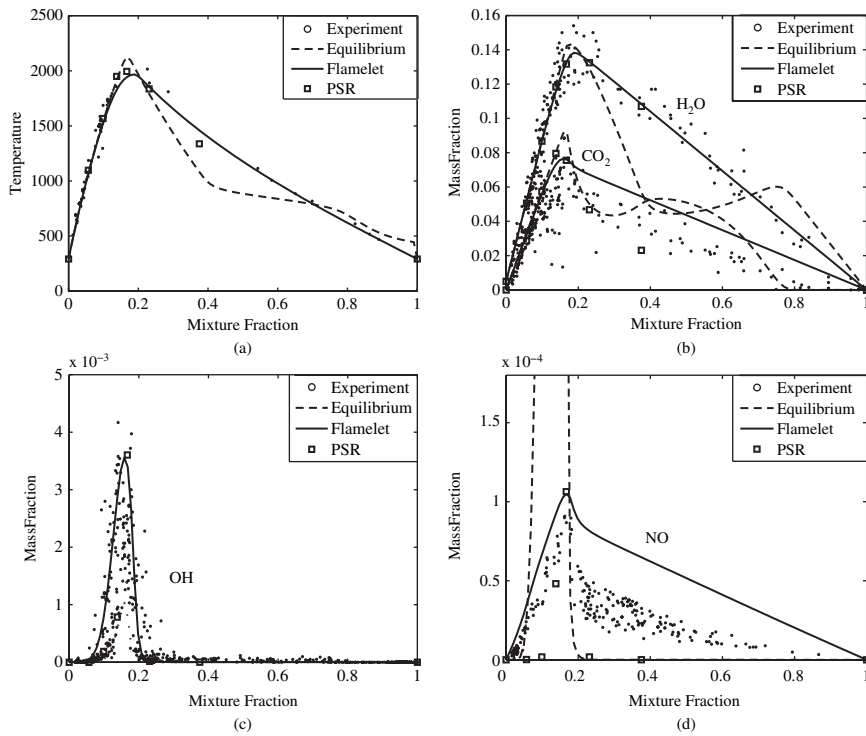

Figure 22: Temperature and species concentrations in a $CH_4/H_2/N_2$-air flame conditioned on various values of heat loss as a function of mixture fraction from both experiments and three canonical reactor models: (a) temperature at $\gamma = -0.0372$, (b) CO_2 and H_2O mass fraction at $\gamma = -0.0107$, (c) OH mass fraction at $\gamma = +0.0158$, (d) NO mass fraction at $\gamma = +0.0688$.

significant deviations from equilibrium are noted in the near stoichiometric and rich regions of the flame. Thus, the performance of the equilibrium model relative to the TNF flame data is inferior to that of both the PSR and SLFM reaction models. Quantitative validation, although not yet completed, requires that an appropriate validation metric be applied to the results obtained from all three canonical reactors for all ϕ_i measured experimentally.

7.5 Soot models

An essential aspect of parameterization by mixture fraction in the three canonical reactor models discussed above (equilibrium, SLFM, PSR) is that all species diffuse at the same rate. However, soot is the product of a relatively slow reaction, is not in equilibrium and does not diffuse at the same rate as the molecular species. Hence, soot is not expected to correlate well with mixture fraction. Attempts to correlate the soot volume fraction with mixture fraction in calculations of turbulent diffusion flames have been carried out previously with limited success [116]. From measurements carried out in co-flow diffusion flames, Kennedy *et al.* [117] modeled the nucleation rate as a function of mixture fraction alone and showed the surface growth process to be the controlling mechanism in determining total soot volume fractions. A second complication presented by soot is that in strongly sooting flames, the soot can significantly alter the flame chemistry. It acts as a sink for important species such as OH and C_2H_2 and as a source for CO during oxidation. It also alters the heat release profile through radiative heat loss. Due to this bidirectional coupling between the soot field and the flame field, it cannot be effectively postprocessed on established flame fields as has been done with other pollutants such as NO_x.

Currently, there are two approaches to modeling soot formation in a multiscale fire simulation. The first approach is to solve transport equations on the computational mesh for the variables of interest in the chosen soot model. For example, if using the Lindstedt soot model [39], transport equations need to be solved for the soot volume fraction and the soot particle number density. The second approach is to include the soot formation and oxidation processes in the subgrid scale reaction model, and then parameterize these slower processes with an additional 'time' parameter. For example, in the SLFM approach, the slow processes such as NO_x or soot formation are not accurately captured because the flamelet equations are solved to steady state [118]. To alleviate this shortcoming, the flamelet equations can be solved in unsteady form using time as an additional parameter. The transient flamelet may be thought of as moving through the computational mesh in a Lagrangian sense. Pitsch *et al.* [119] linked the flamelet time to axial position in a jet based on the axial jet velocity and then performed a numerical simulation of soot formation in a turbulent C_2H_4 jet diffusion flame. In the progress variable approach, a scalar (or combination of scalars) that correlates monotonically with the subgrid flamelet time is employed as the 'time' parameter and transported on the computational mesh. This approach was first employed by Desam and Smith [120] to study NO_x formation in turbulent nonpremixed jet flames.

8 Turbulence/chemistry interactions

Transportation fires are characterized by interactions between the length and time scales of the turbulent transport processes and the chemical reactions. These length and time scales may or may not overlap, as illustrated in Fig. 23. In this figure, the 'mixing time scale' refers to the time scales of the turbulent transport processes while the 'chemistry time scale' refers to the time scales of the reactions in the kinetic mechanism. The axis in Fig. 23 represents the time and length scales of the fire physics with the smallest scales on the left and the largest scales on the right. The scales resolved on the CFD mesh, the 'macromixing' region, represent only a small subset of the scales present in the fire. The 'micromixing' region is characterized by subgrid scale mixing phenomena and turbulence/chemistry interactions that are unresolved on the computational mesh. The LES filter scale is the boundary between these two regions. Subgrid scale models must appropriately account for these complex coupled interactions at the unresolved scale. These subgrid interactions influence chemical source terms in scalar transport equations and the distribution of gas phase species and soot in the fire.

A mixing model (represented by the 'subgrid mixing model' block at the unit problems level of the V&V hierarchy) accounts for scalar micromixing, which is the subgrid variation of the scalar field from the mean scalar value transported on the mesh, by describing the statistical distribution of the subgrid scalar field.
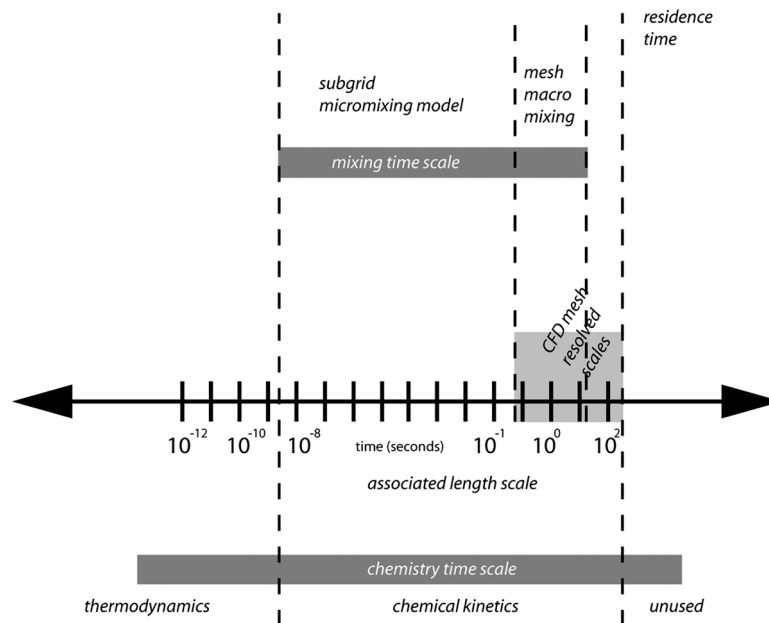

Figure 23: Length and time scales of turbulent transport processes and chemical reactions.

If the joint PDF of a set of scalars $\varphi = (\varphi_1, \varphi_2, \ldots, \varphi_n)$ is known, the mean value of any function of these scalars can be calculated as

$$\overline{\phi} = \int_{\varphi_n} \ldots \int_{\varphi_1} \phi(\varphi) P(\varphi_1, \ldots, \varphi_n) \mathrm{d}\varphi_1 \ldots \mathrm{d}\varphi_n, \tag{49}$$

where $P(\varphi_1, \ldots, \varphi_n)$ is the joint PDF of $(\varphi_1, \ldots, \varphi_n)$.

Models which describe the full joint PDF of φ are known as direct or transported PDF methods [121, 122]. Direct PDF methods are often used in the simulation of turbulent flows where many chemical degrees of freedom are incorporated [123, 124], although difficulties arise in modeling the diffusion terms in the PDF transport equations. Recently, Fox and coworkers have proposed the finite-mode PDF or multi-environment PDF model [125, 126]. This model is based on discretizing the joint PDF into a small number of environments or modes and then solving transport equations for the scalar concentrations in each environment along with the probability of each environment. Higher order statistics are incorporated by increasing the number of modes that are transported. In this way, joint PDFs may be discretely approximated and chemical source terms closed directly. Analogous to direct PDF methods, the primary difficulty in the multi-environment PDF approach lies in modeling the diffusion between environments.

8.1 Validation of presumed PDF models in nonpremixed flames

An alternate approach to direct PDF methods is a class of models, presumed PDF models, where the shape of the PDF is prescribed. These models represent an approximation to eqn (49). The presumed functions are typically continuous, which implies that the presumed PDF represents all statistical moments of the variable. Presumed PDF models offer significant advantages over direct PDF methods, primarily because of their relative ease of implementation into existing CFD codes. One disadvantage is that joint composition PDFs of all the reaction model parameters are not easily presumed. As a result, statistical independence is often assumed for reaction models with several parameters,

$$P(\varphi_1, \ldots, \varphi_n) \approx P(\varphi_1) \cdots P(\varphi_n), \tag{50}$$

where $P(\varphi_1, \ldots, \varphi_n)$ is the joint PDF of $(\varphi_1, \ldots, \varphi_n)$ and $P(\varphi_1)$ is the PDF of (φ_1). With this assumption of statistical independence, the joint PDF of the reaction model parameters is represented as a product of conditional and marginal PDFs. Then, eqn (49) becomes

$$\overline{\phi} = \int_{\varphi_n} \ldots \int_{\varphi_1} \phi(\varphi) P(\varphi_1) \ldots P(\varphi_n) \mathrm{d}\varphi_1 \ldots \mathrm{d}\varphi_n. \tag{51}$$

Despite its limitations, this class of models is widely used. Fortunately, many reaction models currently in use have only a few parameters which are often not strongly correlated.

The issue of parameter independence in combustion systems was evaluated using TNF workshop data for a $CO/H_2/N_2$–air flame, a $CH_4/H_2/N_2$–air flame, and a piloted CH_4–air flame [127]. Two models for the joint PDF of a reaction model parameterized by (f, γ) were considered. One model assumes that the parameters are independent and that the marginal PDF of heat loss is a delta function. The other model assumes that the conditional PDF of heat loss conditioned on mixture fraction is a delta function. Both models employ a marginal mixture fraction PDF.

Figure 24 shows temperature plots of the piloted CH_4–air flame comparing presumed PDF model average values to experimental average values. Both PDF models use a clipped Gaussian mixture fraction PDF. For the data labeled 'Marg. PDF', the marginal heat loss PDF is assumed to be a delta function. For the data labeled 'Cond. PDF', the conditional PDF of heat loss conditioned on mixture fraction is a delta function. The plots include data from a third model, the mean value model, which assumes zero variance in heat loss and mixture fraction. Additional plots from the three flames for all measured species (N_2, O_2, CH_4, CO, H_2, CO_2, H_2O, OH, and NO) and temperature are found in [127].

Overall, the delta conditional heat loss PDF model predicts the mean scalar values better than the delta marginal heat loss PDF model, although application of an appropriate metric is needed to quantify the differences. The assumption that the conditional PDF of heat loss is a delta function ensures that integration occurs over all realizable space. However, the conditional PDF model does require knowledge of the conditional expectation of heat loss. A proposed shape for this function can be found in [127]. The marginal PDF model assumes that f and γ are statistically independent, resulting in integration over a constant heat loss for all mixture fractions. The experimental data is not realizable for all points in f / γ space, so a normalization is performed when integrating over any nonrealizable space. This normalization prevents accurate prediction of O_2 and N_2.

The mean value model predictions are good only in regions far downstream in the flame where mixing of the fuel and air streams has occurred. The assumptions of the mean value model are poor in the near jet region where mixing is not complete.

8.2 Shape of presumed PDF

Two different presumed shapes for $P(\varphi)$ were considered for the pool fire simulations: the β-PDF [95, 128, 129] and the clipped-Gaussian PDF [107, 130, 131]. These PDFs are parameterized by the mean ($\overline{\varphi}$) and variance (σ_φ^2) of the variable φ. Given the LES formulation of the governing equations, variables transported on the mesh ($\overline{\varphi}$) are implicitly filtered. Additionally, because of the variable-density nature of the flows being simulated, the Favre-filtered form of the governing equations (Section 6) is used.

To compute PDF shape, the LES must supply both the Favre-filtered variable and its variance. A transport equation is typically evolved for the Favre-filtered variable, while the variance may be modeled in several ways [132]. The LES algorithm described in Section 6 employs a scale similarity model [128], assuming that
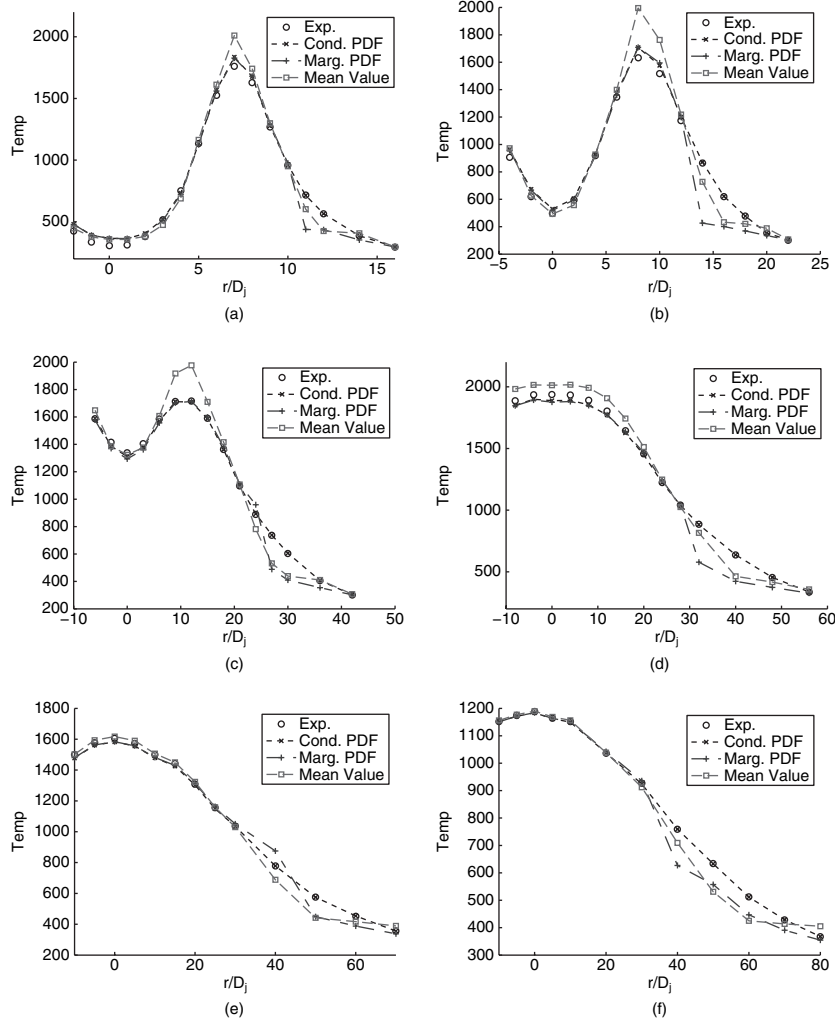
Figure 24: Temperature plots in a piloted CH_4–air flame comparing presumed PDF model average values to experimental average values. The plots are at (a) $h/D = 7.5$ cm, (b) $h/D = 15$ cm, (c) $h/D = 30$ cm, (d) $h/D = 45$ cm, (e) $h/D = 60$ cm, and (f) $h/D = 75$ cm, where h is the height above the burner and D is the diameter of the orifice.

the small-scale statistics can be inferred from the resolved scale structures in the flow. Using the standard definition of the variance, the mixture fraction variance is modeled as

$$\sigma_f^2 = C(\widetilde{f^2} - \tilde{f}^2), \tag{52}$$

where $\tilde{f}$ is the Favre-filtered mixture fraction and the coefficient $C = 0.5$ [133]. Lacking a true mean as required by eqn (52), the filter is used as an approximation to the mean and then multiplied by the model parameter.

By construction, the presumed PDF for φ matches the mean and variance of φ. For variables which range from 0 to 1, the maximum variance is given by

$$\sigma^2_{\varphi,\text{max}} = \overline{\varphi}(1 - \overline{\varphi}). \tag{53}$$

At maximum variance, both the β and clipped-Gaussian PDFs reduce to appropriately weighted δ-functions at $\varphi = 0$ and $\varphi = 1$,

$$P(\varphi) = (1 - \overline{\varphi})\delta(\varphi) + (\overline{\varphi})\delta(\varphi - 1), \sigma^2_{\varphi} = \sigma^2_{\varphi,\text{max}}. \tag{54}$$

Likewise, at zero variance, they become a single -function at $\varphi = \overline{\varphi}$,

$$P(\varphi) = \delta(\varphi - \overline{\varphi}), \sigma^2_{\varphi} = 0. \tag{55}$$

Both the β-PDF and clipped-Gaussian PDF become singular at zero and at maximum variances [107], but their properties (eqns (54) and (55)) insure that the PDF does not need to be constructed or integrated at these limits. Nevertheless, integration of the β-PDF can be very difficult (and inaccurate) when the variance is near its maximum, even when using integration schemes designed for singular functions. The clipped-Gaussian PDF creates no integration difficulties at high variances because the singularities are treated directly with α_0 and α_1 [107], making the clipped-Gaussian PDF easier and computationally cheaper to integrate than the β-PDF.

9 Radiative heat transfer model

Radiation, the dominant mode of heat transfer in hydrocarbon fires, is incorporated in the V&V hierarchy at the unit problem level in Fig. 9. With the advent of massively parallel computers, performing realistic computations of participating media radiative transfer is increasingly tractable. In order to spatially resolve the important flow characteristics in a fire, grids containing 10^6–10^8 computational cells are used at every time step associated with the calculation. Parallelization of the radiation calculations by decomposing the radiation solution in spatial, angular, or energy domains is essential. A finite volume-based discrete ordinates radiation model that is decomposed in the spatial domain is employed. The inputs to this model are gas temperature and the concentrations of the radiatively active species (CO_2, H_2O, soot), which are calculated on the spatially decomposed flow grid as well as at the boundaries. The adoption of a spatial decomposition strategy for the radiation component allows easy integration with other components in the LES fire simulation tool.

9.1 Discrete ordinates method

The discrete ordinates method is based on the numerical solution of the radiative transport equation (RTE) along specified directions. The total solid angle about a

location is divided into a number of ordinate directions, each assumed to have uniform intensity. Each transport equation that is solved corresponds to an ordinate direction selected from an angular quadrature set that discretizes the unit sphere and describes the variation of directional intensity throughout the domain. If ζ_m, μ_m, and η_m represent the direction of cosines associated with each ordinate direction, k represents the absorption coefficient and I_b represents the black body emissive power, then the differential equation governing the discrete ordinates method in the absence of scattering can be written for each direction m as [134],

$$\zeta_m \frac{\partial I_m}{\partial x} + \mu_m \frac{\partial I_m}{\partial y} + \eta_m \frac{\partial I_m}{\partial z} = -kI_m + kI_b \ . \tag{56}$$

The boundary condition associated with the eqn (56), considering the surrounding surfaces to be black, is

$$I_m = I_b. \tag{57}$$

If the absorption coefficient and temperature within the domain and at the boundaries are specified, eqn (56) can be iteratively solved for the directional intensities (I_m) throughout the domain for each direction associated with the discrete ordinates method.

The variables of interest in most radiative transfer analyses are the distributions of radiative heat flux vectors ($\mathbf{q}(\mathbf{r})$) and the radiative source terms ($-\nabla \cdot \mathbf{q}(\mathbf{r})$). The radiative source term describes the conservation of radiative energy within a control volume and is a source term in the total energy equation, thereby coupling radiation with the other physical processes that occur in a multi-physics application. Both of these variables are direction-integrated quantities and readily determined once the distributions of directional intensities (I_m) within the domain are known [135].

When using the discrete ordinates method, integrations over solid angles to obtain $\mathbf{q}(\mathbf{r})$ and $-\nabla \cdot \mathbf{q}(\mathbf{r})$ are replaced by a quadrature of order n and an appropriate angular weight (w_m) associated with each direction, m. The number of equations to be solved depends on the order of approximation, n, used. In the work described here, $n = 4$ (the S4 approximation).

The discrete ordinates method is spatially decomposed to solve the RTE on parallel computers [136]. Mathematical libraries of robust, scalable, nonlinear and linear solvers developed by third parties are used to solve the matrices that result during the solution procedure [85]. The domain boundaries are assumed to be black walls at a temperature of 293 K.

9.2 Radiative properties

In order to solve for the intensities (I_m) for each direction associated with the discrete ordinates method (eqn (56)), radiative properties throughout the computational domain must be specified. It is also desirable to solve the RTE in a limited number of spectral intervals or bands in the interest of computational efficiency. Therefore, radiative property models must be selected that are appropriate for the conditions encountered in a transportation fuel pool fire, divide the spectrum of

interest into a limited number of spectral intervals and provide averaged or spectrally integrated radiative properties at each interval or band.

The algorithm described here requires the radiative properties in the form of an absorption coefficient. Absorption coefficients may be extracted from total or averaged transmissivity or emissivity data using Beer–Lambert's law after specification of path length or mean beam length. However, the specification of path lengths/mean beam lengths is difficult in buoyant pool fires due to the 'puffing' phenomenon exhibited by such fires [137]. Also, Beer–Lambert's law is not valid for an absorption coefficient that has been averaged over many spectral lines. Estimating an absorption coefficient by using a single path length and Beer–Lambert's law for the entire spatial field results in significant error in radiative field solutions [138, 139]. Nevertheless, it is difficult to implement more rigorous procedures within the domain decomposition strategy employed here and therefore all absorption coefficients are computed using a single path length.

The gray model property model that has been implemented employs total emissivity data to compute absorption coefficients. The total emissivity of CO_2–H_2O gas mixtures is first determined from a series of curve fit relations from Hottel charts for low temperature flames (300 K $< T <$ 1,200 K), a weighted-sum-of-gray-gases model proposed by Coppalle and Vervisch [140] for high temperature flames (2,000 K $< T <$ 3,000 K), and a linear interpolation between the two regimes at intermediate temperatures. Total absorption coefficients are then extracted from the total emissivity data after specification of a mean beam length. Details of this property model may be found in Adams [141].

The correlation of Sarofim and Hottel [63] for the emissivity of a sooting flame is employed to estimate the absorption coefficient of soot:

$$k_{\text{soot}} = \frac{4}{L_c}\ln(1 + 350 f_v T L_e), \tag{58}$$

where f_v is the soot volume fraction, T is the gas or soot temperature in Kelvin, and L_e is the mean beam length.

To determine non-gray properties, the spectral region of interest (50 to 10,000 cm^{-1}) is divided into a number of intervals (width $\approx$ 25 cm^{-1}) and spectral optical depths are determined at each interval employing a narrow band model (RADCAL) [5]. An average absorption coefficient (k_η) corresponding to each interval is then obtained by dividing the spectral optical depth by a path length (L). The entire spectrum is then divided into six bands and the average absorption coefficients within each band (η) are lumped together to yield a patch mean absorption coefficient for that band according to the equation

$$k_{\text{patch}} = \frac{\int_{\eta,\text{band}} k_\eta I_{b,\eta} e^{-k_\eta L} d\eta}{\int_{\eta,\text{band}} I_{b,\eta} e^{-k_\eta L} d\eta}. \tag{59}$$

This strategy is similar to that employed by Hostikka *et al.* [74] for performing radiation calculations in an LES fire simulation except that a Planck mean absorption coefficient was evaluated and employed in their calculations. Krishnamoorthy *et al.*

[142] showed the advantages of employing a Patch mean absorption coefficient over a Planck mean coefficient in comparisons against non-gray benchmark problems.

The evaluation of absorption coefficients from the gray and non-gray models requires the specification of a path length or mean beam length. One-tenth of the mean beam length of the computational domain is taken as the path length by Hostikka *et al.* [74] in their pool fire simulations and is the mean beam length/path length used here.

9.3 Algorithm verification

One case used for radiation model verification is the nonhomogeneous medium benchmark introduced by Hsu and Farmer [143]. The problem consists of an isothermal unit cube with cold black walls. The interior of the cube consists of a gray, non-scattering, absorbing/emitting material with an optical thickness (τ = absorption coefficient times the side length) distribution given by

$$\tau(x, y, z) = 0.9 \left(1 - \frac{|x|}{0.5} \right) \left(1 - \frac{|y|}{0.5} \right) \left(1 - \frac{|z|}{0.5} \right) + 0.1 \tag{60}$$

A uniform black body emissive power of unity within the domain defines the distribution of temperature. Since the radiative properties, temperature, and boundary conditions for this problem are known, the RTE can be solved to determine the distributions of the radiative fluxes and the radiative flux divergence. The root mean square error norms, also known as the L2 error norms, of both radiative flux and radiative flux divergence are shown in Fig. 25.

The spherical surface symmetrical equal dividing angular quadrature scheme (SSD) [144] was employed to calculate the numerical solution accuracies plotted in Fig. 25. The results obtained by Burns and Christon [145] using the rotated LC quadrature scheme are also shown in Fig. 25 (open symbols). The number of equations that need to be solved with the SSD_{1a}, SSD_{2a}, and SSD_{3b} schemes are exactly the same as those of the rotated LC_4, LC_6, and LC_8 quadrature sets, respectively, enabling a direct comparison of the solution accuracies of the two schemes when the same number of equations is being solved. In general, the two schemes perform equally well with error norms decreasing as spatial and angular resolution increases.

10 Heat transfer to an embedded object in a JP-8 pool fire

The goal of this work is to calculate the potential hazard of an explosive device immersed in a pool fire of transportation fuel. We characterize the hazard in terms of the time to ignition of the device and the violence (measured as kinetic energy of the exploded container) of the event. To accomplish this goal, a fire simulation tool for performing scalable, parallel, three-dimensional simulations of a large-scale pool fire with an embedded device has been developed. This simulation tool incorporates all the fire physics components at the unit problem level of the
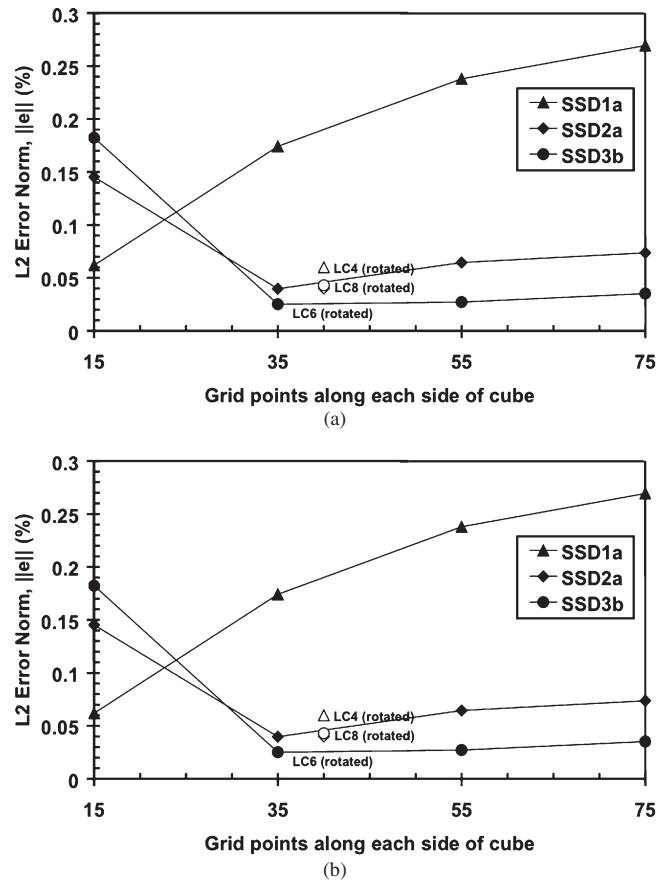
Figure 25: Numerical accuracy of quadrature schemes as a function of spatial and angular resolution: (a) predicted radiative flux divergence along $(x, 0, 0)$; (b) predicted radiative heat flux along $(x, 0.5, 0)$.

V&V hierarchy in Fig. 9 to accurately represent the heat transfer to the device. Coupling of this fire simulation tool with an energetics material model to predict time to ignition of an explosive device is discussed in Section 12.

10.1 Modified LES algorithm

The LES equations (Section 6) are modified to account for the presence of a steel-shelled container of explosive material (PBX, HMX) in the computational domain. A law of the wall approximation [146] is used for the boundary condition for the momentum transport equation. Because radiation is the dominant mode of heat transfer in heavily sooting pool fires, radiative heat transfer between the solid and the fire is modeled in the enthalpy transport equation while convection

heat transfer is neglected [147]. For the solid wall boundary conditions, the wall is considered as a black body radiating at its own temperature. The solid object heats up, so the boundary condition for the fire is time varying. The turbulent conductivity is modeled in a manner similar to the turbulent diffusivity as discussed in Section 6.

The solid is modeled with the 'material-point' method (MPM) [148, 149], which uses material (mass) points to represent the solid and calculates stresses and heat conduction within the solid using interpolation by basis functions. The equations for the fire in the presence of an object are discretized using a finite-volume scheme, as described in Section 6. Additional details about the MPM algorithm are found in [148, 149].

10.2 Coupling between LES fire phase and container heat-up phase

Because of the wide range of time scales of the complete system (intended use) case, the simulation is decomposed into three distinct phases. For the first phase, the dynamic LES fire simulation is performed to determine a steady heat flux profile to the device. This profile is generally not symmetric and depends on such variables as the crosswind velocity, the size of the pool, and the placement of the device. This phase is characterized by simulated time scales of O(1–10 s). In the second phase of the calculation, the heat-up phase, the fire simulation is frozen. Steady heat flux values from the fire phase are applied to an MPM object representing the device embedded in or near the fire. As this phase develops, the steel shell and the explosive material heat up, with the two materials represented by a single temperature field. This phase, with time scales of O(10 s–10 min), is continued until the explosive's ignition criterion is reached. The third phase, the explosion phase, begins at the ignition point. The explosion phase is characterized by time scales of $O(10^{-9}–10^{-3}$ s) and represents the container breakup and the expulsion of the explosive.

A second simulation decomposition strategy was also tested. In this strategy, the first phase proceeds as described above. The steady heat fluxes from the fire phase are then fed to a series of one-dimensional calculations performed in the radial direction of the cylindrical object. The one-dimensional calculations compute heat transfer and pressurization along the radial direction until the ignition point of the explosive is reached, at which point the simulation terminates. This strategy does not include the details of the exploding container.

10.3 Subsystem cases: heat transfer in a large JP-8 pool fire

Data sets obtained at the subsystem level of the V&V hierarchy (Fig. 9) are limited due to harsh experimental conditions and high cost, and the errors associated with such measurements are large. Nevertheless, even limited data is useful for achieving some level of validation and error quantification, particularly since the subsystem cases include the coupling of multiple physical processes and closely mimic the intended use. Here, two experimental data sets are used in a validation

exercise for the LES fire phase. These data sets include heat flux measurements made at various locations in and near large JP-8 pool fires. This validation exercise is conducted using the validation metric discussed in Section 3.2.

10.3.1 Validation data sets

Two experiments have been identified for subsystem validation purposes. The first experiment was conducted by Kramer *et al.* [150] at the Sandia National Laboratories Burn Site. The experiment was intended to measure heat fluxes from a circular JP-8 pool fire (7.16 m diameter) to a large calorimeter (4.6 m length, 1.2 m diameter, 2.54 cm wall thickness) suspended directly over the pool. After the pool was ignited, temperatures were recorded for 30 min from thermocouples fixed at various axial and azimuthal locations inside the calorimeter. From the interior thermocouple data, heat flux measurements to the outside surface of the calorimeter were deduced using the Sandia One-Dimensional Direct and Inverse Thermal (SODDIT) code [151]. In an effort to reduce wind effects, a circular wind fence (24.4 m diameter) was constructed around the fire. Wind direction and speed were measured outside the wind fence. The average wind speed was 1 m/s with a primary direction normal to the axis of the calorimeter. Despite the wind fence, the fire was observed to lean in the primary wind direction.

The second experiment was conducted by Blanchat *et al.* [152] at the Sandia National Laboratories Burn Site to provide well-characterized environmental information relative to an open pool fire with embedded, weapon-sized calorimeters. The circular pool of JP-8 fuel measured 7.9 m. Details regarding the experimental setup can be found in [152]. Four separate tests were performed on different days with different measured wind speeds and different calorimeters. Here, the focus is on Experiment #1, wherein two small calorimeters (0.3 m diameter, 0.4 m long) were positioned over the pool at radii of 1.5 m and 2.5 m and the winds were characterized as being calm (0–2.2 m/s) in a direction normal to the axis of the calorimeters. Heat flux gauges were positioned near the ground with one gauge in the center and the remaining 48 gauges in concentric circles spaced 1 m apart along eight radial directions of the pool. No wind fence was used in this experiment; wind speeds were measured at various positions around the pool.

10.3.2 Simulation details and results

Two JP-8 pool fire simulations were performed. In the first simulation, the large calorimeter was suspended over the pool in the same configuration as [150]. The second simulation was the same configuration as the first with the exception that it did not include the calorimeter. Both simulations were run on 448 processors in a $20\text{ m} \times 17\text{ m} \times 20\text{ m}$ rectangular domain with a resolution of $200 \times 170 \times 200$. The x-axis was taken as the vertical direction. A fuel inlet with diameter 7.16 m representing the pool surface was included on the $-x$ face while the remaining $-x$ face was modeled with a wall boundary condition. Fuel was introduced into the domain based on a fuel regression rate of 1.6 mm/min. On the $-y$ vertical boundary, an inlet boundary condition was used to model the crosswind and was set to 1 m/s for

both simulations. The opposing vertical side ($+y$) and the top of the domain ($+x$) were modeled with an outlet boundary condition. The remaining vertical sides ($-z$ and $+z$) had pressure boundary conditions. The entire flow was initially quiescent and fuel was introduced after the simulation began. Both simulations were run until the time-averaged heat fluxes became steady. For the first simulation, heat fluxes were extracted at different axial locations on the calorimeter surface around the azimuthal direction corresponding to the thermocouple locations in the first experiment described above. For the second simulation, heat fluxes were extracted from the pool surface corresponding to the pool surface heat flux gauges of the second experiment described above.

From the first simulation, azimuthal heat flux values at a location 1.96 m down the large calorimeter are presented in Fig. 26. Also shown are the experimental results with 90% confidence intervals for the mean data and the estimated error. Since only one experiment was performed, the first 10 min of the data were split into three equal parts to represent three data sets. The positions of $\pi/2$ and $3\pi/2$ correspond to the top and bottom of the calorimeter, respectively. The windward side of the calorimeter corresponds to the π position and the leeward side to the 0 position. In Fig. 26(a), the simulation data lie within the experimental confidence intervals except for the lower half of the cylinder on the windward side where the simulation underpredicts the heat flux. The size of the confidence intervals is a strong function of the wind, even with the wind fence present. That is, the heat flux is varying wildly within the first 10 min, creating a large range in which the true mean heat flux could reside. This effect is particularly noticeable in the region of highest heat flux to the calorimeter (position $\pi/2$, bottom of the device). In Fig. 26(b), the estimated error is plotted with 90% confidence intervals. Again, the error is large for the lower half of the calorimeter on the windward side. However, the largest error range occurs in the region of highest heat flux to the calorimeter (position $\pi/2$, bottom of the device).

For the second simulation, results of simulated heat fluxes to the pool surface are compared with the experimental data in Fig. 27. As with the previous data set, the temporal heat flux data were separated into four segments of equal time. The results are presented as a function of the gauge id number. Gauge #1 corresponds to the center location of the pool. Gauges #2–#9 correspond to the first ring and so on. Note that because the diameters of the simulated fire and the experimental fire were slightly different, the gauges corresponding to the 300 series from Blanchat *et al*. [152] are not included in this comparison. This second data set is better characterized, resulting in smaller bands for the 90% confidence interval, and most simulation data points lie within the confidence interval. Two points of higher heat flux are predicted by the simulation for Gauges #5 and #6, which correspond to the windward side of the fire. These higher simulation heat fluxes may result from holding the wind speed constant at 1m/s when the experimental wind speed varied up to 2.2 m/s. Higher wind speed results in a higher tilt to the fire, lowering heat fluxes to the windward side. From the simulation results, global metric values of the average relative error metric plus/minus the average relative confidence indicator are 11% ± 22%. In other words, the average relative error ranges from 0% to 33% with a 90% confidence.
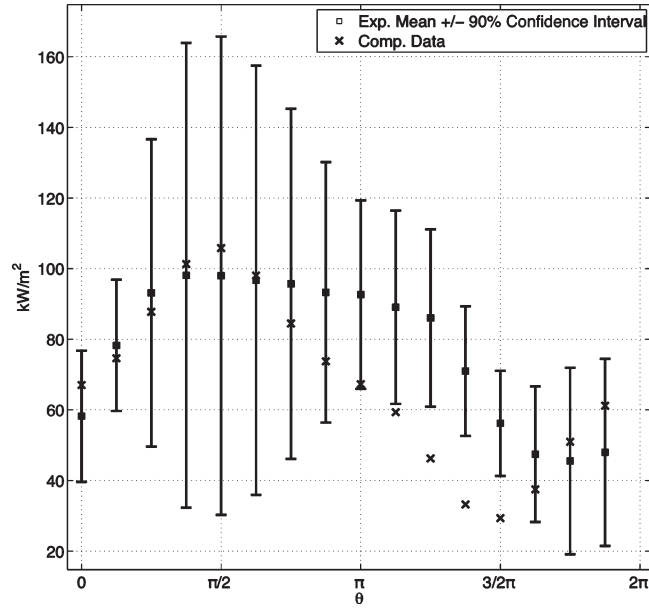
(a)
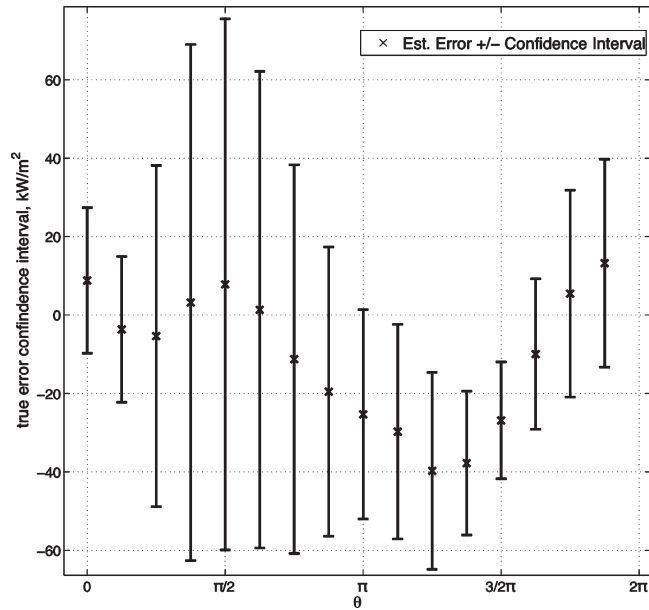
(b)

Figure 26: Heat flux results for simulation 1 compared to experimental data at the
1.96 m slice of the large calorimeter. (a) Experimental data with a 90%
confidence interval (Exp. Mean) and simulation mean (Comp. Data).
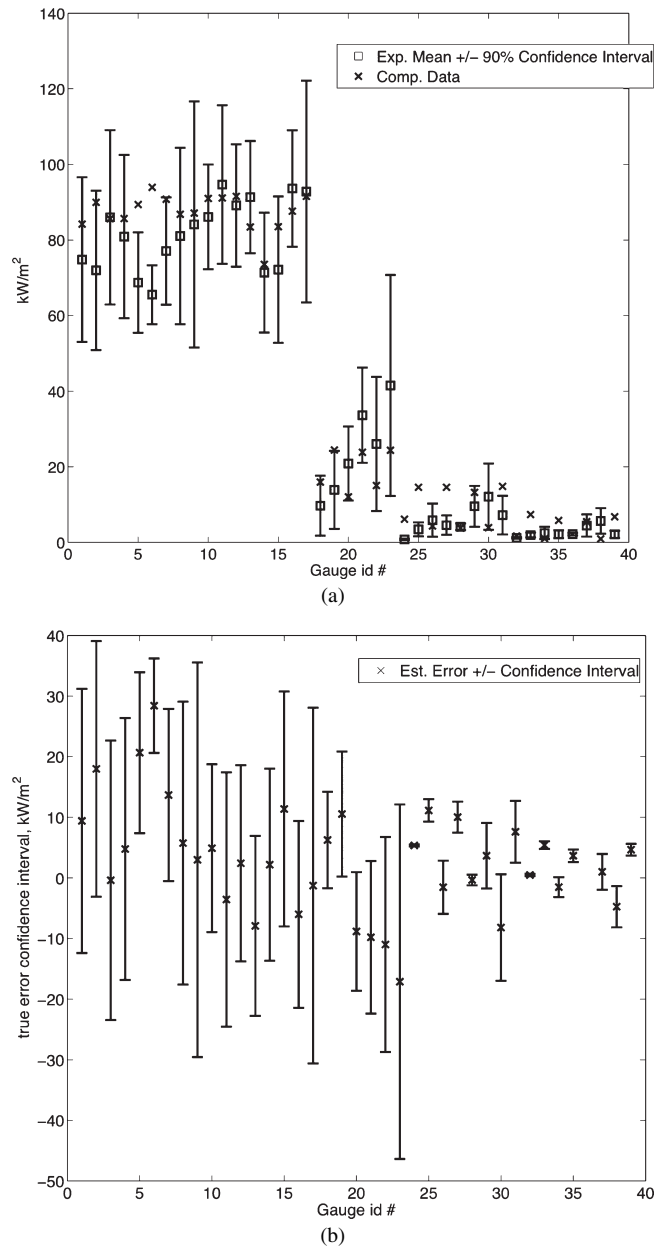(b) Estimated simulation error with a 90% confidence interval.

Figure 27: Heat flux results at the pool surface for simulation 2 compared to heat flux gauge data at corresponding locations. (a) Experimental data with a 90% confidence interval (Exp. Mean) and simulation mean (Comp. Data). (b) Estimated simulation error with a 90% confidence interval.

11 Prediction of heat flux to an explosive device in a JP-8 pool fire

As stated in Section 3.1, the motivation for this work is to develop a simulation tool with the intended application of predicting heat transfer to an object in a large-scale transportation fire. While such scenarios are worth studying experimentally for hazard classification reasons, they remain expensive and dangerous to perform. Thus, a simulation tool built on a hierarchy of validation becomes one potential solution for negating the costs and risks associated with performing the experiment. This section focuses on the prediction of heat flux to a rocket motor in a large-scale (10–20 m) JP-8 fire for transportation hazard classification. Both the Department of Transportation (DOT) and the Department of Defense (DoD) have established testing protocols that include an external bonfire test.

The DOT external fire test calls for the explosive article to be placed on a non-combustible surface (steel grate) above a fuel source of wood soaked with diesel fuel or equivalent. The fire is ignited and allowed to burn for 30 min while the material is observed for evidence of detonation, explosion, etc. [153]. The DoD testing protocol requires that the test specimen be surrounded by fuel rich flames from a large open hearth containing liquid fuel such that the heat transfer to the specimen is approximately 90% radiative. Wind speeds should not exceed 5.8 m/s [154].

Simulations of a full scale bonfire test of an explosive device under wind conditions allowable under the DoD testing protocol were performed using the LES fire simulation tool described in this chapter. One objective of the simulation was to determine if higher wind speeds allowed within the DoD protocol affected the engulfment of the rocket motor in the fire, resulting in a scenario that would not qualify under the current DoD regulations of full fire engulfment.

The explosive device was represented by a 1.2 m diameter, 8 m long cylindrical steel container. The container was suspended 1 m above a 24 m × 13 m rectangular pool of JP-8 fuel. The five-component JP-8 surrogate formulation proposed by Zhang *et al.* [36] was used for all calculations. Simulations were run at two different wind speeds, 2.2 and 5.8 m/s, the upper limit of the testing protocol.

The 5.8 m/s crosswind case was run on a 30 m × 60 m × 60 m domain with a mesh resolution of 100 × 180 × 180. The case was run on 196 processors of a massively parallel machine at Lawrence Livermore National Laboratory (LLNL). The 2.2 m/s crosswind case was run on 324 processors at LLNL on a 30 m × 30 m × 60 m domain with a mesh resolution of 150 × 150 × 220.

Volume-rendered images of the temperature field at one time slice are shown in Fig. 28 for both cases. The device is not fully engulfed in the flames in either case, but in the 5.8 m/s wind condition, the fire is blown away from the container. Figure 29 shows the volume-rendered temperature field in the 2.2 m/s crosswind case from a different angle at a later time. The region of highest heat flux to the container is at a location exposed to radiation from the leeward side of the fire.

As with the calorimeter experiments in Section 11, the wind speed significantly influences the azimuthal heat flux profile of the device. Table 5 lists mean heat
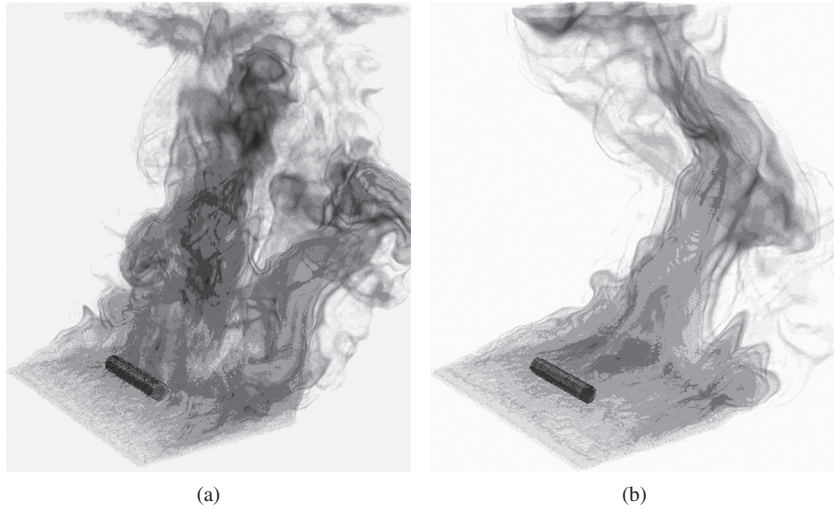
Figure 28: Volume-rendered images of the temperature field in the JP-8 pool fire: (a) 2.2 m/s crosswind and (b) 5.8 m/s crosswind.

Figure 29: Volume-rendered image of the temperature field in the JP-8 pool fire with a 2.2 m/s crosswind. Side view showing region of highest temperature on upper leeward side of the container surface.

Table 5: Mean heat fluxes to the explosive device obtained from simulations at two different wind speeds.

Axial location	Wind speed = 2.2 m/s		Wind speed = 5.8 m/s	
	Position = $\pi/2$	Position = $3\pi/2$	Position = $\pi/2$	Position = $3\pi/2$
4 m	110.1 kW/m^2	82.3 kW/m^2	1.8 kW/m^2	77.5 kW/m^2
6 m	68.6 kW/m^2	84.6 kW/m^2	0.7 kW/m^2	92.8 kW/m^2

fluxes obtained from the simulation at various locations on the surface of the device. At the lower crosswind speed (2.2 m/s), the device acts as a flame holder, leading to heat fluxes near the top of the container (position $\pi/2$) that equal or exceed those at the bottom. For the 5.8 m/s crosswind case, the heat flux at the top of the device is two orders of magnitude smaller than the heat flux at the bottom of the container. At this higher wind speed, the flame is still burning under the device but leans away from the top of the device, producing the large variation in heat flux between the top and bottom of the device. The low heat fluxes at the top of the device are a clear indication that the container is not even partially engulfed in the fire.

Information from the LES simulation about flame location and shape, heat flux to the explosive device, and rate of device heat-up can be used to establish acceptable operating conditions for the hazard classification bonfire test. At the time of this simulation, no data for this particular scenario existed. Thus, the LES tool was used in a predictive manner. Error bars associated with the results from these bonfire simulations must be inferred from lower hierarchical validation exercises, resulting in the qualitative statements made above regarding the effect of the wind on the flame shape and heat flux characteristics. It is recognized that for many scenarios, these types of qualitative statements are unacceptable. Indeed, in high consequence scenarios, the most valuable predictive simulation results will have quantified uncertainty. While such a simulation requirement should be considered, it is not a straightforward proposition as it involves an understanding of how errors propagate in a nonlinear fashion through the V&V hierarchy. Error quantification for multiphysics, multiscale simulations is further addressed in Section 13.

12 Predicting the potential hazard of an explosive device immersed in a JP-8 pool fire

The motivation for this chapter has been the calculation of the potential hazard of an explosive device engulfed in a pool fire of transportation fuel. One metric for potential hazard is the time to explosion. This section describes two methods for computing time to explosion using heat flux data from the LES fire simulation tool (see Section 10.2). The first method represents the explosive device as a three-dimensional MPM object during the heat-up and explosion phases. With this

method, the large deformations caused by the device breakup are captured on the computational mesh. The second method approximates heat transfer in the explosive device with a one-dimensional model that incorporates high fidelity reaction kinetics. Both methods simulate the response of an energetic material (HMX or PBX) in a fast cook-off environment. Here, fast cook-off is defined as ignition under confinement with the energetic material exposed to high heat fluxes. Fast cook-off is a surface phenomenon. Because the thermal conductivity of HMX is very low, large temperature gradients exist within the explosive. Only a thin layer of explosive next to the inner wall of the container experiences temperature increases high enough for chemical decomposition reactions to occur. In fact, the reaction zone is likely to occur in the region where the explosive is sandwiched next to the container wall [155]. For the purposes of this section, fast cook-off occurs when the energetic material is exposed to heat fluxes in the range of 1−100 kW/m^2, a typical range for transportation fuel pool fires.

12.1 Three-dimensional heat transfer, PBX combustion model

The three-dimensional heat transfer model uses the MPM [148] infrastructure as noted in Section 10.2. Because of the potentially long time to ignition, an implicit time integration strategy is used to eliminate stability restrictions on the timestep [149]. A single temperature field is computed for the steel and PBX, an assumption which ignores any potential gap formation due to differential thermal expansion or pressurization due to decomposition of the explosive. Heat fluxes to the container surface obtained from the fire simulation are fit to high order polynomials, which are in turn sampled at particle locations around the surface of the container and treated as source terms in the solution of the energy equations. Once the heat-up phase reaches a preset ignition temperature, the implicit MPM code transfers the data to the explicit MPMICE code [155] for the explosion; pressurization does occur in the explosion phase.

The combustion model for PBX [156] in the MPMICE code is based on a simplified two-step chemical reaction scheme introduced by Ward *et al*. [157] in which the solid propellant is initially converted to gas phase intermediates in a thermally activated, moderately exothermic zero-order reaction; the intermediates then react to form final products in a highly exothermic, bimolecular flame reaction having zero activation energy. As the pressure increases, the increase in rate of the second reaction moves the flame closer to the propellant surface, increasing the heat feedback and the surface temperature. The increased surface temperature increases the rate of the first reaction, which further increases the rate of gas formation. The computational model implements an iterative solver that seeks a self-consistent solution to the two closed form expressions for burn rate as a function of surface temperature and surface temperature as a function of burn rate and pressure.

These models for the heat transfer and explosion phases were run using heat flux data from LES simulations of a 10 cm long, 10 cm diameter steel container of PBX immersed in 0.5−1.0 m JP-8 pool fires.

12.2 One-dimensional heat transfer, fast cook-off HMX model

Heat flux data from an LES simulation of a 30 cm long, 12 cm diameter steel container immersed in a 30 cm JP-8 pool fire were extracted at 24 locations around the circumference of the steel cylinder. The 20 seconds of fluctuating heat flux data available from the simulation were assumed to be at quasi-steady state and were replicated to extend to the time required by the fast cook-off HMX model.

The HMX model is spatially one-dimensional, fully transient, and consists of equations for modeling the solid (condensed) phase HMX, the gas phase, and the surrounding steel container for fast cook-off conditions [158]. The steel shell provides a thermal barrier to the external heat flux. The condensed phase HMX decomposition reactions are described by distributed kinetics (calculated throughout the condensed phase, not just at the surface). The gas phase description includes a detailed chemistry model for the combustion of HMX. Solution of the PDEs results in temperature, pressure, velocity, and species mass fractions as a function of position and time. For additional details, see [158, 159].

12.3 Prediction of time to ignition and explosion violence

By coupling both the MPM/MPMICE models and the fast cook-off HMX model with the LES pool fire simulation, time to ignition for a range of conditions (labeled 'ignition delay' in Fig. 30) was computed using both models as shown in Figure 30. Also included in Fig. 30 are experimental time-to-ignition data obtained by various researchers [158]. Each point for 'Flux at steel container' is matched with the corresponding 'Flux at interface' value. The heat flux at the steel/HMX (or PBX)
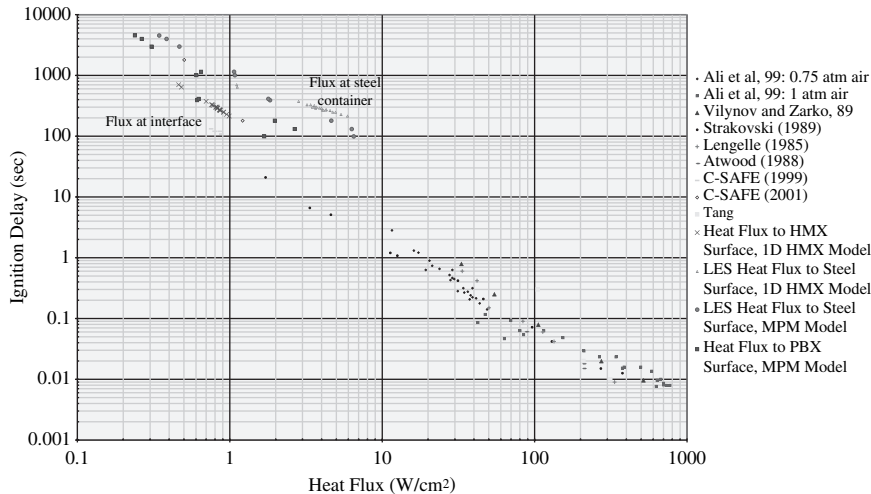

Figure 30: Ignition delay versus heat flux showing the difference between calculated interior and calculated exterior heat flux levels.

interface is always lower than the heat flux at the exterior of the steel container. In the limit as the heat flux at the exterior approaches zero, the heat flux at the interior will also approach zero and these two heat fluxes must converge. At the high heat flux end, the deviation between the two fluxes is large. As seen in Fig. 30, when the time to ignition is based on the 'Flux at interface' values, the model results fall in line with the experimental data. Alternatively, when the time to ignition is based on the 'Flux at steel container' values, the predicted values show a strong deviation from the experimental values. Hence, an important parameter for accurately predicting ignition delay is the flux that the explosive experiences, not the flux that the container experiences.

In addition to time to ignition data, results from the MPMICE simulations show evidence of explosion violence; data from two cases are considered here. In case 1, the 10 cm diameter container is located 0.5 m above the edge of a 0.5 m diameter JP-8 pool fire, there is no crosswind, and the fuel regression rate is 6.4 mm/min. In case 2, the container is located 0. 25 m above the edge of a 0.5 m diameter JP-8 fire, the crosswind speed is 4 m/s, and the fuel regression rate is 6.4 mm/min. Azimuthal heat flux data from LES pool fire simulations of the two cases are displayed in Fig. 31 for one axial location on the container. These traces are distinctly
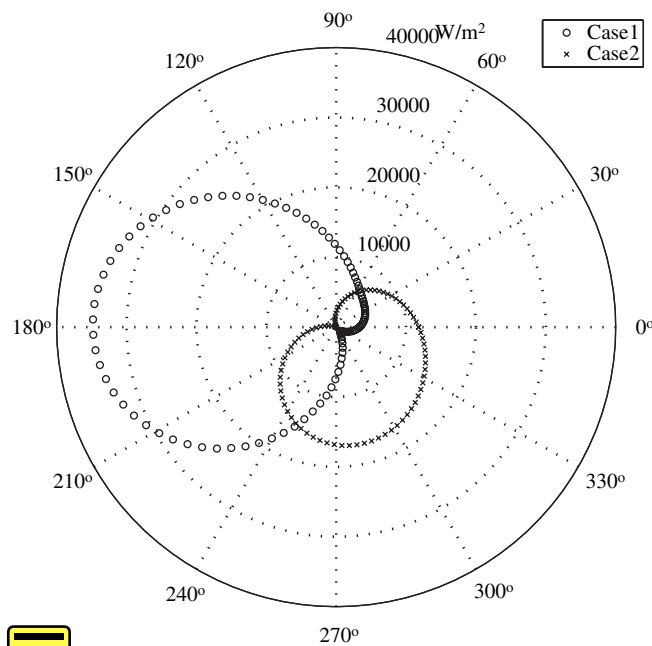

Figure 31: Azimuthal heat flux traces at a single axial location on the steel container obtained from pool fire simulations of cases 1 and 2. Case 1 – no crosswind, container is located 0.5 m above the pool surface at the edge of fire. Case 2 – crosswind of 4 m/s, container is located 0.25 m above pool surface at fire's edge.

different and produce different fragmentation patterns as observed in the three-dimensional volume renderings of the container and propellant shown in Fig. 32. A more quantitative analysis measures explosion violence by the total kinetic energy of the exploded container. Based on such an analysis, one finds that case 1 is more violent than case 2 as seen in the kinetic energy plots of Fig. 33. Experimental results have shown that lower heat fluxes produce more violent explosions, and the simulation data in Fig. 33 mirror this observation; the heat fluxes experienced by case 2 are lower than those experienced by case 1 (see Fig. 31).

These time to ignition and violence of explosion predictions provide the perspective of overall trends in the simulation data and generally agree with available data. However, they do not achieve the desired predictivity as there are no associated error bars. In fact, it is unclear how the errors identified in previous sections of this chapter were propagated in a nonlinear fashion up through the hierarchy for this 'complete system' case. For this reason, error quantification and propagation (see Section 13) are essential areas of research in moving toward predictivity.

13 Toward predictivity: error quantification and propagation

The goal of the simulation at the level of the complete system is to accurately predict heat flux to a container of energetic material immersed in a transportation fuel
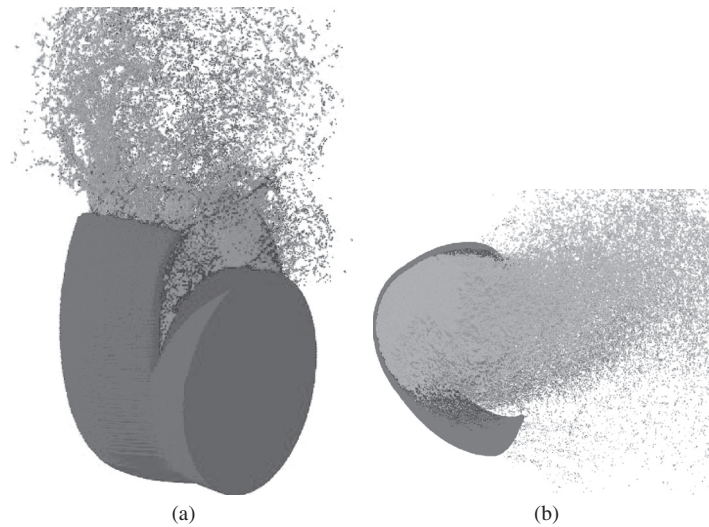

Figure 32: Volume rendered images of container fragmentation and propellant release from simulations of a 10 cm diameter steel container of PBX embedded in a 0.5 m JP-8 pool fire simulation. (a) Case 1 – no crosswind, container is located 0.5 m above the pool surface at the edge of fire. (b) Case 2 – crosswind of 4 m/s, container is located 0.25 m above pool surface at fire's edge.
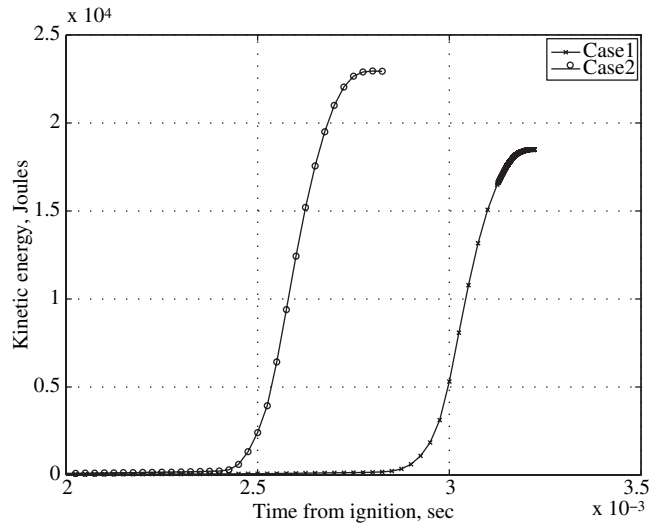
Figure 33: Total kinetic energy of all particles in the MPMICE simulation. Case 1 − no crosswind, container is located 0.5 m above the pool surface at the edge of fire. Case 2 − crosswind of 4 m/s, container is located 0.25 m above the pool surface at fire's edge.

pool fire. Despite the methodology of a V&V hierarchy, predictivity has not yet been achieved. The validation comparisons at the subsystem involve some quantification through the use of validation metrics, while the results of the 'complete system' simulation are qualitative in nature and do not account for uncertainties in the experimental or the simulation data. What are needed are systematic ways to represent uncertainties at lower levels of the V&V hierarchy, efficient computational algorithms to propagate those uncertainties all the way up to the complete system level, methods for identifying the parameters that control uncertainty, metrics for quantifying simulation error, and datasets for validation [160]. Ultimately, the truth comes from the experimental data; it is the window on the physical world. However, in ambitious simulations of multiphysics and multiscale simulations, it is through the tight coupling of both simulation and experimental data that predictivity with uncertainty quantification will be achieved.

The field of uncertainty quantification (UQ) and error propagation in multiphysics problems is an area of active research, and it still is not clear what approach or approaches will provide the analysis tools necessary to achieve predictability. McRae [160], Marzouk and Najm [161], and Najm and coworkers [162, 163] have proposed a method for UQ based on Bayesian inference. Inferring model parameters and inputs from data is a challenging task and is known as the inverse problem. Marzouk and Najm have focused on using Bayesian statistics as a foundation for inference [161]. Interestingly, there are strong parallels between the forward propagation of uncertainty and Bayesian approaches to inverse problems. Marzouk and

Najm have formalized this connection and have successfully employed polynomial chaos expansion (PCE) techniques to propagate a wide range of uncertainty through the forward problem. In their approach, the model parameters and field variables are treated as stochastic quantities that can be modeled using PCE techniques. After sampling the resultant spectral expansion, they achieve a more efficient Bayesian solution of the inverse problem [161]. A comparison of this approach to the more conventional UQ method of sensitivity analysis and error propagation in the context of H_2–O_2 ignition under supercritical-water conditions was performed by Najm and coworkers [163]. The results indicate that PCE methods provide first-order information similar to that from the sensitivity analysis. In addition, the PCE methods preserve higher-order information that is needed for accurate UQ and for assigning confidence intervals on sensitivity coefficients. Analysis shows substantial uncertainties in the sensitivity coefficients, illustrating that these higher-order effects can be significant.

A second approach has been proposed by Frenklach *et al.* [164] that relies on the concept of data collaboration. Data collaboration organizes the available experimental data and its uncertainties together with mechanistic knowledge of the physical system using the abstraction of a dataset. A dataset unit consists of 'the measured observation, uncertainty bounds on the measurement, and a model that transforms active parameter values into a prediction for the measurement' [164]. Note that a dataset unit includes a model prediction. In its application, the concept of data collaboration recognizes that a model is only an approximation to the truth and that the truth comes from the experimentally measured data. With this dataset abstraction, numerical analysis techniques can be used to probe the dataset. For example, consistency of the model to the measured data or of dataset units to each other can be determined with constrained optimization that utilizes solution mapping tools and robust control algorithms. Within the data collaboration framework, consistency thus becomes a quantifiable metric that can open up the model to a new level of interrogation such as what a low or moderate value of the metric means. Additionally, the uncertainties of the experimental data are transferred directly into the model. In one example of how to use the consistency metric, a consistency test was performed with the GRI-Mech 3.0 dataset [165], which is composed of 77 dataset units. The test identified two major outliers in the dataset. The researchers who collected the data re-examined their original observations and modified the reaction times they had extrapolated, removing the inconsistency in the GRI-Mech 3.0 dataset [164]. A similar consistency analysis could be applied to the model as outliers could also indicate a problem with the model.

Neither the Bayesian inference nor the data collaboration approach has yet been applied to a complex, multiscale, multiphysics problem. However, in order to achieve predictivity, it is clear that these or other approaches must be implemented in more complex systems. The treatment of uncertainties must become more systematic. Additionally, to use either approach in problems involving heat transfer to an explosive device, a large number of dataset units need to be identified and compiled in a database repository including the data sets discussed in Section 10. There is clearly much work to be done both computationally and experimentally.

14 Summary

The prediction of heat transfer to objects in transportation fuel pool fires using simulations requires the integration of complex methodologies. This chapter has summarized these methodologies in a manner that will assist the reader in identifying a suitable approach to this challenging problem. The high cost of large-scale experiments (both real-world and simulation), combined with the greatly reduced fidelity of experimental data at this scale, provides strong motivation for the use of a computational approach that has been validated and verified in a systematic manner and that includes the quantification and propagation of uncertainty from the unit problem level to the complete system level.

Acknowledgments

References

[1]   Hottel, H., Review: Certain laws governing diffusive burning of liquids by Blinov and Khudiakov (1957). *Fire Research Abstracts and Reviews*, **1**, pp. 41–44, 1959.

[2]   De Ris, J., Fire radiation − a review. *Proceedings of the Combustion Institute*, **17**, pp. 1003–1016, 1979.

[3]   Mudan, K., Thermal radiation hazards from hydrocarbon pool fires. *Progress in Energy and Combustion Science*, **10**, pp. 59–80, 1984.

[4]   Klassen, M. & Gore, J., Structure and radiation properties of pool fires. Technical report, NIST-GCR-94-651, NIST, 1994.

[5]   Grosshandler, W.L., Radcal: a narrow-band model for radiation calculations in a combustion environment. Technical report, 1402, NIST, 1993.

[6]   Vela, I., Kuhr, C. & Schönbucher, A., CFD simulation of large hydrocarbon pool fires. *Proceedings of the Combustion Institute*, **31**, p. 177, 2006.

[7]   Gawlowski, M., Göcka, D., Kuhr, C., Vela, I. & Schönbucher, A., The probabilistic thermal radiation model OSRAMO II for hydrocarbon pool fires. *Proceedings of the Combustion Institute*, **31**, p. 178, 2006.

[8]   Mudan, K. & Croce, P., Fire hazard calculations for large open hydrocarbon fires. *SFPE Handbook of Fire Protection Engineering*, ed. P. DiNenno, National Fire Protection Association: Quincy, MA, pp. 197–240, 1995.

[9] Smith, R.K., Radiation effects on large fire plumes. *Proceedings of the Combustion Institute*, **11**, pp. 507–515, 1967.

[10] Shinotake, A., Koda, S. & Akita, K., An experimental study of radiative properties of pool fires of an intermediate scale. *Combustion Science and Technology*, **43**, pp. 85–97, 1985.

[11] Gritzo, L., Nicolette, V., Tieszen, S., Moya, J. & Holeu, J., Heat transfer to the fuel surface in large pool fires. *Transport Phenomena in Combustion*, ed. S. Chan, Taylor and Francis: Washington, DC, 1995.

[12] Tieszen, S., On the fluid mechanics of fires. *Annual Review of Fluid Mechanics*, **33**, pp. 67–92, 2001.

[13] Shaddix, C., Williams, T., Blevins, L., Shefer, R., Jensen, K., Suo-Antilla, J. & Kearney, S., Soot formation, transport, and radiation in unsteady diffusion flames. Technical report, SAND2004-5060, Sandia National Laboratories, 2004.

[14] Daghlian, J., *Soot Volume Fraction and Temperature Measurement in a Slot Burner Utilizing Laser Extinction and Emission*, Master's Thesis, University of Utah, 2002.

[15] Koseki, H. & Yumoto, T., Air entrainment and thermal radiation from heptane pool fires. *Fire Technology*, **24**, pp. 33–47, 1988.

[16] Joulain, P., The behavior of pool fires: state of the art and new insights. *Proceedings of the Combustion Institute*, **27**, pp. 2691–2706, 1998.

[17] Oberkampf, W.L. & Trucano, T.G., Validation methodology in computational fluid dynamics. Fluids 2000, AIAA Paper 2000-2549, June 2000.

[18] Oberkampf, W.L., Trucano, T.G. & Hirsch, C., Verification, validation, and predictive capability in computational engineering and physics. Technical report, SAND2003-3769, Sandia National Laboratories, 2003.

[19] Oberkampf, W.L. & Barone, M.F., *Measures of Agreement Between Computation and Experiment: Validation Metrics*, Technical report, SAND2005-4302, Sandia National Laboratories, 2005.

[20] Wood, C., Development and application of a surrogate distillate fuel. *Journal of Propulsion and Power*, **5**, pp. 399–405, 1989.

[21] Schulz, W., Oxidation products of a surrogate JP-8 fuel. *Preprints, Division of Petroleum Chemistry*, **37**, pp. 383–392, 1992.

[22] Maurice, L. & Lindstedt, P., Detailed chemical-kinetic model for aviation fuels. *Journal of Propulsion & Power*, **16**, pp. 187–195, 2000.

[23] Agosta, A., *Development of a Chemical Surrogate for JP-8 Aviation Fuel Using a Pressurized Flow Reactor*. Master's Thesis, Drexel University: Philadelphia, PA, 2002.

[24] Mawid, M., Park, T., Sekar, B. & Arana, C., Development of detailed chemical kinetic mechanisms for ignition/oxidation of JP-8/Jet-A/JP-7 fuels. *Proceedings of ASME Turbo Expo 2003*, ASME, June 2003.

[25] Yan, S., Eddings, E., Palotas, A., Pugmire, R. & Sarofim, A., Prediction of sooting tendency for hydrocarbon liquids in diffusion flames. *Energy and Fuels*, **19**, pp. 2408–2415, 2005.

[26] Yan, S., *Formulation and Some Applications of Jet Fuel Surrogates*, PhD Thesis, University of Utah, Salt Lake City, UT, 2005.

[27] Blinov, V. & Khudiakov, G., Diffusion burning of liquids. *Academy of Sciences*, p. 208, 1961. Translation NTIS AD-296762.

[28] Burgess, D., Grumer, J. & Wolfhard, H., Diffusive burning of liquid fuels in open trays. *Fire Research Abstracts and Reviews*, **3**, pp. 177–192, 1961.

[29] Grumer, J., Strasser, A., Kubala, T. & Burgess, S., Uncontrolled diffusive burning of some new liquid propellants. *Fire Research Abstracts and Reviews*, **3**, pp. 159–175, 1961.

[30] Babrauskas, V., Free burning fires. *Fire Safety Journal*, **11**, pp. 33–51, 1986.

[31] Iwata, Y., Koseki, H., Janssens, M. & Takahashi, T., Combustion characteristics of crude oils. *Fire & Materials*, **25**, pp. 1–7, 2001.

[32] *Annual Book of ASTM Standards*. American Society for Testing and Materials: Philadelphia, PA, 2001.

[33] Edwards, T., 'Real' kerosene aviation and rocket fuels: composition and surrogates. *Chemical and Physical Processes in Combustion*, pp. 276–279, 2001.

[34] Delfau, C.D.J., Akrich, R. & Vovelle, C., Chemical structure of atmospheric pressure premixed *n*-decane and kerosene flames. *Combustion Science and Technology*, **106**, pp. 327–344, 1995.

[35] Violi, A., Yan, S., Eddings, E.G., Sarofim, A.F., Granata, S., Faravelli, T. & Ranzi, E., Experimental formulation and kinetic model for JP-8 surrogate mixtures. *Combustion Science and Technology*, **174**, pp. 399–417, 2002.

[36] Zhang, H.R., Eddings, E.G. & Sarofim, A.F., Criteria for selection of components for surrogates of natural gas and transportation fuels. *Proceedings of the Combustion Institute*, **31**, 2006 (in press).

[37] Bockhorn, H. (ed.), *Soot Formation in Combustion: Mechanisms and Models of Soot Formation*, Springer Series in Chemical Physics, Vol. 59, Springer-Verlag: Berlin.

[38] Appel, J., Bockhorn, H. & Frenklach, M., Kinetic modeling of soot formation with detailed chemistry and physics: laminar premixed flames of C_2 hydrocarbons. *Combustion and Flame*, **121**, pp. 122–136, 2000.

[39] Leung, K.M., Lindstedt, W.P. & Jones, W.P., A simplified reaction mechanism for soot formation in non-premixed flames. *Combustion and Flame*, **87**, pp. 289–305, 1991.

[40] Frenklach, M. & Wang, H., Soot formation in combustion: mechanisms and models. *Springer Series in Chemical Physics*, **59**, pp. 165–190, 1994.

[41] Richter, H., Granata, S., Green, W.H. & Howard, J.B., Detailed modeling of PAH and soot formation in a laminar premixed benzene/oxygen/argon ion-pressure flame. *Proceedings of the Combustion Institute*, **30**, pp. 1397–1405, 2005.

[42] Marinov, N.M., Westbrook, C.K. & Pitz, W.J., Detailed and global kinetics model for hydrogen. *8th International Symposium on Transport Processes*, Report No. CONF-9510158-1, October 1995.

[43] Hwang, S.M., Gardiner, W.C., Jr., Frenklach, M. & Hidaka, Y., Introduction zone exothermicity of acetylene ignition. *Combustion and Flame*, **67**, pp. 65–75, 1987.

[44] Miller, J.A., Mitchell, R.E., Smooke, M.D. & Kee, R.J., Toward a comprehensive chemical kinetic mechanism for the oxidation of acetylene – comparison of model predictions with results from flame and shock tube experiments. *Proceedings of the Combustion Institute*, **19**, pp. 181–196, 1982.

[45] Wang, H. & Frenklach, M., A detailed kinetic modeling study of aromatics formation in laminar premixed acetylene and ethylene flames. *Combustion and Flame*, **110(1–2)**, pp. 173–221, 1997.

[46] Marinov, N.M. & Malte, P.C., Ethylene oxidation in a well-stirred reactor. *International Journal of Chemical Kinetics*, **27**, pp. 957–986, 1995.

[47] Tsang, W., Chemical kinetics data base for combustion chemistry. Part 3. Propane. *Journal of Physics and Chemistry Reference Data*, **17(2)**, pp. 887–951, 1988.

[48] Tsang, W., Chemical kinetics data base for combustion chemistry. Part 5. Propene. *Journal of Physics and Chemistry Reference Data*, **20(2)**, pp. 221–273, 1991.

[49] Pitz, W.J. & Westbrook, C.K., Chemical kinetics of the high-pressure oxidation of normal-butane and its relation to engine knock. *Combustion and Flame*, **63(1–2)**, pp. 113–133, 1986.

[50] Miller, J.A. & Melius, C.F., Kinetic and thermodynamic issues in the formation of aromatic compounds in flames of aliphatic fuels. *Combustion and Flame*, **91**, pp. 21–39, 1992.

[51] Emdee, J., Brezinsky, K. & Glassman, I., A kinetic model for the oxidation of toluene near 1200 K. *Journal of Physics and Chemistry*, **96**, pp. 2151–2161, 1992.

[52] Doute, C., Delfau, J.L. & Vovelle, C., Detailed reaction mechanisms for low pressure premixed *n*-heptane flames. *Combustion Science and Technology*, 1999.

[53] Pitsch, H., Personal communication, 2005.

[54] Marinov, N.M., Pitz, W.J., Westbrook, C.K., Castaldi, M.J. & Senkan, S.M., Modeling of aromatic and polycyclic aromatic hydrocarbon formation in premixed methane and ethane flames. *Combustion Science and Technology*, **116–117(1–6)**, pp. 211–287, 1996.

[55] Westmoreland, P.R., Howard, J.B. & Longwell, J.P., Tests of published mechanisms by comparison with measured laminar flame structure in fuel-rich acetylene combustion. *Proceedings of the Combustion Institute*, **21**, pp. 773–782, 1988.

[56] Bastin, E., Delfau, R.M., Reuillon, M., Vovelle, C. & Warnatz, J., Experimental and computational investigation of the structure of a sooting C_2H_2-O_2-Ar flame. *Proceedings of the Combustion Institute*, **22**, pp. 313–322, 1988.

[57] Bockhorn, H., Fetting, F. & Wenz, H.W., Investigation of the formation of high molecular hydrocarbons and soot in premixed hydrocarbon-oxygen flames. *Berichte der Bunsen-Gesellschaft*, **87(11)**, pp. 1067–1073, 1983.

[58] Harris, S.J. & Weiner, A.M., Surface growth of soot particles in premixed ethylene/air flames. *Combustion Science and Technology*, **31(3–4)**, pp. 155–167, 1983.

[59] Castaldi, M.J., Marinov, N.M., Melius, C.F., Huang, J., Senkan, S.M., Pitz, W.J. & Westbrook, C.K. *Proceedings of the Combustion Institute*, **26**, pp. 693–702, 1996.

[60] Bittner, J.D. & Howard, J.B., Composition profiles and reaction mechanisms in a near-sooting premixed benzene/oxygen/argon flame. *Proceedings of the Combustion Institute*, **18**, pp. 1105–1116, 1981.

[61] Tregrossi, A., Ciajolo, A. & Barbella, R., The combustion of benzene in rich premixed flames at atmospheric pressure. *Combustion and Flame*, **117(3)**, pp. 553–561, 1999.

[62] Bakali, A.E., Delfau, J.L., Akrich, R. & Vovelle, C., Measurement of soot volume fraction and gaseous species concentrations in premixed *n*-heptane and iso-octane flames. *Journal de Chimie Physique et de Physico-Chimie Biologique*, **94(9)**, pp. 1659–1673, 1997.

[63] Sarofim, A.F. & Hottel, H.C., Radiative transfer in combustion chambers: influence of alternative fuels. *Proceedings of the 6th International Heat Transfer Conference*, **6**, Hemisphere Publishing: Washington, DC, pp. 199–217, 1978.

[64] Neoh, K.G., Howard, J.B. & Sarofim, A.F., Soot oxidation in flames. *Particulate Carbon: Formation During Combustion*, eds D.D. Siegla & G.W. Smith, Plenum: New York, pp. 261–282, 1981.

[65] Mell, W.E., McGrattan, K.B. & Baum, H.R., Numerical simulation of fire plumes. *Proceedings of the Combustion Institute*, **26**, pp. 1523–1530, 1996.

[66] McGrattan, K.B., Baum, H.R., Rehm, R.G., Forney, G.P. & Prasad, K., Future of fire simulation. *Fire Protection Engineering*, **13**, pp. 24–36, 2002.

[67] Schmidt, R.C., Smith, T.M., DesJardin, P.E., Voth, T.E., Christon, M.A., Kerstein, A.R. & Wunsch, S.E., *On the Development of the Large Eddy Simulation Approach for Modeling Turbulent Flow: LDRD Final Report*, Technical report, SAND2002-0807, Sandia National Laboratories, New Mexico and California, 2002.

[68] Kang Y., Wen, J., McGrattan, K. & Baum, H., Use of a laminar flamelet approach in the large eddy simulation of flame structure at the base of a pool fire. *Interflam 2001: International Interflam Conference, 9th Proceedings*, Vol. 1, Interscience Communications Ltd.: London, pp. 743–754, 2001.

[69] Xin, Y., Gore, J., McGrattan, K., Rehm, R. & Baum, H., Fire dynamics simulation of a turbulent buoyant flame using a mixture-fraction-based combustion model. *Combustion and Flame*, **141**, pp. 329–335, 2005.

[70] Morvan, D., Porterie, B., Loraud, J. & Larini, M., Numerical simulation of a methane/air radiating turbulent diffusion flame. *International Journal of Numerical Methods for Heat & Fluid Flow*, **10**, pp. 196–227, 2000.

[71] Wang, H., Joulain, P. & Most, J., On the numerical modeling of buoyancy-dominated turbulent diffusion flames by using large-eddy simulation and

k–ε turbulence model. *Combustion Science and Technology*, **176**, pp. 1007–1034, 2004.

[72]   Desjardin, P. & Frankel, S., Two-dimensional large eddy simulation of soot formation in the near-field of a strongly radiating nonpremixed acetylene-air turbulent jet flame. *Combustion and Flame*, **119**, pp. 121–132, 1999.

[73]   McGrattan, K., Baum, H. & Rehm, R., Fire dynamics simulator, technical reference guide. Technical report, NISTIR 6467, National Institute of Standards and Technology, Gaithersburg, Maryland, 2000.

[74]   Hostikka, S., McGrattan, K.B. & Hamins, A., Numerical modeling of pool fires using les and finite volume method for radiation. *Proceedings of the 7th International Symposium on Fire Safety Science*, ed. D. Evans, Boston, MA, pp. 383–394, 2003.

[75]   Pope, S.B., *Turbulent Flows*, Cambridge University Press: Cambridge, UK, 2000.

[76]   Pitsch, H. & Steiner, H., Large-eddy simulation of a turbulent piloted methane/air diffusion flame (Sandia flame D). *Physics of Fluids*, **12(10)**, pp. 2541–2544, 2000.

[77]   Smagorinsky, J., General circulation experiments with the primitive equations. *Monthly Weather Review*, **91(3)**, pp. 99–106, 1963.

[78]   Moin, P., Squires, K., Cabot, W. & Lee, S., A dynamic subgrid-scale model for compressible turbulence and scalar transport. *Physics of Fluids A*, **3(11)**, pp. 2746–2757, 1991.

[79]   Lilly, D.K., A proposed modification of the Germano subgrid-scale closure method. *Physics of Fluids A*, **4**, pp. 633–635, 1992.

[80]   Morinishi, Y., Lund, T., Vasilyev, O. & Moin, P., Fully conservative higher order finite difference schemes for incompressible flow. *Journal of Computational Physics*, **143**, pp. 90–124, 1998.

[81]   Gottlieb, S., Shu, C.W. & Tadmor, E., Strong stability-preserving high-order time discretization methods. *SIAM Review*, **43(1)**, pp. 89–112, 2001.

[82]   Rawat, R., Spinti, J.P., Yee, W. & Smith, P.J., Parallelization of a large scale hydrocarbon pool fire in the Uintah PSE. *Proceedings of IMECE'02 International Mechanical Engineering Congress and Exposition*, ASME, IMECE2002-33105, pp. 49–56, 2002.

[83]   Johnson, C., Parker, S., Hansen, C., Kindlmann, G. & Livnat, Y., Interactive simulation and visualization. *IEEE Computer*, **32(12)**, pp. 59–65, 1999.

[84]   Parker, S., Beazley, D. & Johnson, C., Computational steering software systems and strategies. *IEEE Computational Science and Engineering*, **4(4)**, pp. 50–59, 1997.

[85]   Balay, S., Gropp, W.D., McInnes, L.C. & Smith, B.F., The portable extensible toolkit for scientific computing (PETSc) version 29. Technical report, http://www.mcs.anl.gov/petsc/petsc.html, 2000.

[86]   Falgout, R., Jones, J. & Yang, U., The design and implementation of HYPRE, a library of parallel high performance preconditioners. *Numerical Solution of Partial Differential Equations on Parallel Computers*, eds A. Bruaset & A. Tveito, Springer-Verlag: Berlin, pp. 267–294, 2006.

[87] Roache, P., *Verification and Validation in Computational Sciences and Engineering*. Hermosa Publishers, 1998.

[88] Minion, M., A projection method for locally refined grids. *J. Comput. Phys.*, **127**, pp. 158–177, 1996.

[89] Compte-Bellot, G. & Corrsin, S., Simple Eulerian time correlation of full and narrow-band velocity signals in grid-generated, 'isotropic' turbulence. *Journal of Fluid Mechanics*, **48**, pp. 273–337, 1971.

[90] McDermott, R.J., *Toward One-Dimensional Turbulence Subgrid Closure for Large-Eddy Simulation*, PhD Thesis, University of Utah, Salt Lake City, UT, 2005.

[91] Tieszen, S., Fire sciences validation data, http://192.84.24.155/datasite_viv.cfm.

[92] Piomelli, U. & Liu, J., Large-eddy simulation of rotating channel flows using a localized dynamic model. *Physics of Fluids*, **7(4)**, pp. 839–848, 1995.

[93] DesJardin, P., O'Hern, T. & Tieszen, S., Large-eddy simulation and experimental measurements of the near-field of a large turbulent helium plume. *Physics of Fluids*, **16(6)**, pp. 1866–1883, 2004.

[94] Maas, U. & Pope, S.B., Simplifying chemical kinetics: intrinsic low-dimensional manifolds in composition space. *Combustion and Flame*, **88**, pp. 239–264, 1992.

[95] Williams, F.A., *Combustion Theory: The Fundamental Theory of Chemically Reacting Flow Systems*, 2nd edn, Perseus Books, 1985.

[96] Felder, R.M. & Rousseau, R.W., *Elementary Principles of Chemical Processes*, 2nd edn, John Wiley and Sons: New York, 1986.

[97] Mell, W.E., Nilsen, V., Kosaly, G. & Riley, J.J., Direct numerical simulation investigation of the conditional moment closure model for nonpremixed turbulent reacting flows. *Combustion Science and Technology*, **91**, pp. 179–186, 1993.

[98] Jiménez, J., Liñán, A., Rogers, M.M. & Higuera, F.J., A-priori testing of sub-grid models for chemically reacting nonpremixed turbulent shear flows. *Journal of Fluid Mechanics*, **349**, pp. 149–171, 1997.

[99] DesJardin, P.E. & Frankel, S.H., Large eddy simulation of a nonpremixed reacting jet: application and assessment of subgrid-scale combustion models. *Physics of Fluids*, **10(9)**, pp. 2298–2314, 1998.

[100] Montgomery, C.G., Kosaly, G. & Riley, J.J., Direct numerical simulation of turbulent nonpremixed combustion with multistep hydrogen-oxygen kinetics. *Combustion and Flame*, **109**, pp. 113–144, 1997.

[101] International Workshop on Measurement and Computation of Turbulent Nonpremixed Flames, Sandia National Laboratories, http://www.ca.sandia.gov/TNF/abstract.html

[102] Echekki, T., Kerstein, A.R., Dreeben, T.D. & Chen, J.Y., One-dimensional turbulence simulation of turbulent jet diffusion flames: model formulation and illustrative applications. *Combustion and Flame*, **125**, pp. 1083–1105, 2001.

[103] Goodwin, D.G., An open-source, extensible software suite for CVD process simulation. *Proceedings of CVD XVI and Euro CVD Fourteen*, Electrochemical Society, p. 162, 2003.

[104] Glarborg, P., Kee, R.J., Grcar, J.F. & Miller, J.A., PSR: a FORTRAN program for modeling well-stirred reactors. Technical report, SAND86-8209, Sandia National Laboratories, 1986.

[105] Kee, R.J., Rupley, F.M. & Miller, J.A., *CHEMKIN-II: A Fortran Chemical Kinetics Package for the Analysis of Gas-Phase Chemical Kinetics*, Technical report, SAND 89-8009, Sandia National Laboratories, 1989.

[106] Peters, N., Laminar diffusion flamelet models in non-premixed turbulent combustion. *Progress in Energy and Combustion Science*, **10**, pp. 319–339, 1984.

[107] Sutherland, J.C., Smith, P.J. & Chen, J.H., A quantitative method for a priori evaluation of combustion models. *Combustion Theory and Modeling*, **11(2)**, pp. 287–303, 2007.

[108] Kennedy, C.A. & Carpenter, M.H., A comparison of several new numerical methods for the simulation of compressible shear layers. *Applied Numerical Mathematics*, **14(4)**, pp. 397–433, 1994.

[109] Kennedy, C.A., Carpenter, M.H. & Lewis, R.M., Low-storage, explicit Runge-Kutta schemes for the compressible Navier-Stokes equations. *Applied Numerical Mathematics*, **35(3)**, pp. 177–219, 2000.

[110] Kee, R.J., Dixon-Lewis, G., Warnatz, J., Coltrin, M.E., Miller, J.A. & Moffat, H.K., *Transport*, Technical report, Release 3.5, Reaction Design, Inc.: San Diego, CA, 1999.

[111] Yetter, R.A., Dryer, F.L. & Rabitz, H., A comprehensive reaction mechanism for carbon monoxide/hydrogen/oxygen kinetics. *Combustion Science and Technology*, **79(1–3)**, pp. 97–128, 1991.

[112] Mueller, M.A., Kim, T.J., Yetter, R.A. & Dreyer, F.L., Flow reactor studies and kinetic modeling of the H_2/O_2 reaction. *International Journal of Chemical Kinetics*, **31(2)**, pp. 113–125, 1999.

[113] Bergmann, V., Meier, W., Wolff, D. & Stricker, W., Application of spontaneous Raman and Rayleigh scattering and 2D LIF for the characterization of a turbulent $CH_4/H_2/N_2$ jet diffusion flame. *Applied Physics B*, **66**, pp. 489–502, 1998.

[114] Meier, W., Barlow, R.S., Chen, L.Y. & Chen, J.Y., Raman/Rayleigh/LIF measurements in a turbulent $CH_4/H_2/N_2$ jet diffusion flame: experimental techniques and turbulence-chemistry interaction. *Combustion and Flame*, **123**, pp. 326–343, 2000.

[115] Krishnamoorthy, N., *Reaction Models and Reaction State Parameterization for Turbulent Non-Premixed Combustion,* PhD Thesis, University of Utah, Salt Lake City, UT, 2008.

[116] Gore, J.P. & Faeth, G.M., Structure and spectral radiation properties of turbulent ethylene/air diffusion flames. *Proceedings of the Combustion Institute*, **21**, pp. 1521–1531, 1986.

[117] Kennedy, I.M., Kollmann, W. & Chen, J.Y., Model for soot formation in a laminar diffusion flame. *Combustion and Flame*, **81**, pp. 73–85, 1990.

[118] Peters, N., *Turbulent Combustion*, Cambridge University Press: Cambridge, UK, 2000.

[119] Pitsch, H., Riesmeier, E. & Peters, N., Unsteady flamelet modelling of soot in turbulent diffusion flames. *Combustion Science and Technology*, **158**, pp. 389–406, 2000.

[120] Desam, P.R. & Smith, P.J., A systematic evaluation of NO_x formation pathways and subgrid scale models in turbulent nonpremixed $CO/H_2/N_2$ jet flame predictions. *ASME International Mechanical Engineering Congress and Exposition*, Anaheim, CA, 2004.

[121] Pope, S.B., PDF methods for turbulent reacting flows. *Progress in Energy and Combustion Science*, **11**, pp. 119–195, 1984.

[122] Kollmann, W., The PDF approach to turbulent flow. *Theoretical and Computational Fluid Dynamics*, **1**, pp. 285–349, 1990.

[123] Taing, S., Masri, A.R. & Pope, S.B., PDF calculations of turbulent nonpremixed flames of H_2/CO_2 using reduced chemical mechanisms. *Combustion and Flame*, **95**, pp. 135–150, 1993.

[124] Anand, M.S., Hsu, A.T. & Pope, S.B., PDF calculations for swirl combustors. *AIAA Journal*, **35**, pp. 1143–1150, 1996.

[125] Tsai, K., Gillis, P., Sen, S. & Fox, R.O., A finite-mode PDF model for turbulent reacting flows. *Proceedings of FEDSM99*, ASME/JSME Joint Fluids Engineering Conference, San Francisco, CA, pp. 909–914, 1999.

[126] Fox, R.O., *Computational Models for Turbulent Reacting Flows*, Cambridge University Press, 2003.

[127] Yeates, D.R., *Validation of Presumed Probability Density Function Methods with the Sandia Turbulent Non-Premixed Flames*, PhD Thesis, University of Utah, Salt Lake City, UT, 2005.

[128] Cook, A.W. & Riley, J.J., A subgrid model for equilibrium chemistry in turbulent flows. *Physics of Fluids*, **6(8)**, pp. 2868–2870, 1994.

[129] Girimaji, S.S., Assumed β-PDF model for turbulent mixing: validation and extension to multiple scalar mixing. *Combustion Science and Technology*, **78**, pp. 177–196, 1991.

[130] Lockwood, F.C. & Naguib, A.S., The prediction of the fluctuations in the properties of free, round-jet, turbulent, diffusion flames. *Combustion and Flame*, **24**, pp. 109–124, 1975.

[131] Smoot, L.D. & Smith, P.J., *Coal Combustion and Gasification*, Plenum Press: New York, NY, 1985.

[132] de Bruyn Kops, S.M., *Numerical Simulation of Non-premixed Turbulent Combustion*, PhD Thesis, University of Washington, Seattle, WA, 1999.

[133] Pierce, C.D. & Moin, P., A dynamic model for subgrid-scale variance and dissipation rate of a conserved scalar. *Physics of Fluids*, **10(12)**, pp. 3041–3044, 1998.

[134] Jamaluddin, A.S. & Smith, P.J., Predicting radiative transfer in rectangular enclosures using the discrete ordinates method. *Combustion Science and Technology*, **59**, pp. 321–340, 1988.

[135] Modest, M.F., *Radiative Heat Transfer*, 1st edn, McGraw-Hill: New York, 1993.

[136] Krishnamoorthy, G., Rawat, R. & Smith, P.J., Parallel computations of radiative heat transfer using the discrete-ordinates method. *Numerical Heat Transfer B*, **47**, pp. 19–38, 2005.

[137] Cetegen, B.M. & Ahmed, T.A., Experiments on the periodic instability of buoyant plumes and pool fires. *Combustion and Flame*, **93**, pp. 157–184, 1993.

[138] Denison, M.K., *A Spectral Line-Based Weighted-Sum-of-Gray-Gases Model for Arbitrary RTE Solvers*, PhD Thesis, Brigham Young University, Provo, UT, 1994.

[139] Liu, F., Gülder, Ö.L. & Smallwood, G.J., Non-grey gas radiative transfer analyses using the statistical narrow-band model. *International Journal of Heat and Mass Transfer*, **41**, pp. 2227–2236, 1998.

[140] Coppalle, A. & Vervisch, P., The total emissivities of high-temperature flames. *Combustion and Flame*, **49**, pp. 101–108, 1983.

[141] Adams, B.R., *Computational Evaluation of Mechanisms Affecting Radiation in Gas- and Coal-Fired Industrial Furnaces*, PhD Thesis, University of Utah, Salt Lake City, UT, 1993.

[142] Krishnamoorthy, G., Rawat, R. & Smith, P.J., Parallel computations of non-gray radiative heat transfer. *Numerical Heat Transfer B*, **48**, pp. 191–211, 2005.

[143] Hsu, P. & Farmer, J.T., Benchmark solutions of radiative heat transfer within nonhomogeneous participating media using the Monte Carlo and YIX methods. *ASME Journal of Heat Transfer*, **119**, pp. 185–188, 1997.

[144] Li, B.W., Chen, H.G., Zhou, J.H., Cao, X.Y. & Cen, K.F., The spherical surface symmetrical equal dividing angular quadrature scheme for discrete ordinates method. *ASME Journal of Heat Transfer*, **124**, pp. 482–490, 2002.

[145] Burns, S.P. & Christon, M.A., *Spatial Domain-Based Parallelism in Large-Scale, Participating-Media, Radiative Transport Applications*, Technical report, SAND96-2485, Sandia National Laboratories, 1996.

[146] Sagaut, P., *Large-Eddy Simulation for Incompressible Flows: An Introduction*, 2nd edn, Springer-Verlag: Berlin, 2002.

[147] Ciro, W., *Heat Transfer at Interfaces of a Container of High-Energy Materials Immersed in a Pool Fire*, PhD Thesis, University of Utah, Salt Lake City, UT, 2005.

[148] Sulsky, D., Chen, Z. & Schreyer, H.L., A particle method for history dependent materials. *Computer Methods in Applied Mechanics and Engineering*, **118**, pp. 179–196, 1994.

[149] Guilkey, J.E. & Weiss, J.A., Implicit time integration for the material-point method: quantitative and algorithmic comparisons with the finite-element

method. *International Journal for Numerical Methods in Engineering*, **57**, pp. 1323–1338, 2003.

[150]   Kramer, M.A., Greiner, M., Koski, J.A. Lopez, C., & Suo-Anttila, A., Measurements of heat transfer to a massive cylindrical object engulfed in a circular pool fire. *J. Heat Transfer*, **125**, pp. 110–118, 2003.

[151]   Blackwell, B.F., Douglass, R.W., & Wolf, H., *A User's Manual for the Sandia One-Dimensional Direct and Inverse Thermal (SODDIT) Code*, Technical report, SAND85-2478, Sandia National Laboratories, 1985.

[152]   Blanchat, T.K., Nicolette, V.F., Sundberg, W.D., & Figueroa, V.G., *Well-Characterized Open Pool Experimental Data and Analysis for Model Validation and Development*, Technical report, SAND2006-7508, Sandia National Laboratories, 2006

[153]   Safety Management Services, Tests for class 1 explosives, http://www.sms-ink.com/services_dot_class1.html.

[154]   Department of Defense Explosives Safety Board, Department of Defense Ammunition and Explosives Hazard Classification Procedures, http://ddesb.pentagon.mil/hazardclass/tb700%20review%20draft.pdf.

[155]   Guilkey, J.E., Harman, T.B. & Banerjee, B., An eulerian-lagrangian approach for simulating explosions of energetic devices. *Computers and Structures*, **85**, pp. 660–674, 2007.

[156]   Wight, C.A. & Eddings, E.G., Science-based simulation tools for hazard assessment and mitigation. *Proceedings of the 7th International Symposium on Special Topics in Chemical Propulsion*, September 2007 (submitted).

[157]   Ward, M.J., Son, S.F. & Brewster, M.Q., Role of gas- and condensed-phase kinetics in burning rate control of energetic solids. *Combustion Theory and Modelling*, **2**, pp. 293–312, 1998.

[158]   Meredith, K.V. & Beckstead, M.W., Fast-cookoff modeling of HMX. *39th JANNAF Combustion Meeting*, Colorado Springs, Boulder, CO, 2003.

[159]   Meredith, K.V. & Beckstead, M.W., Laser-induced ignition modeling of HMX. *39th JANNAF Combustion Meeting*, Colorado Springs, Boulder, CO, 2003.

[160]   McRae, G.J., Uncertainty propagation in combustion kinetics – implication for database design and computation. *NSF Workshop on Cyber-Based Combustion Science*, 2006.

[161]   Marzouk, Y. & Najm, H., *Bayesian Inference with Detailed Physical Models*, Technical report, Combustion Research Facility News, Sandia National Laboratories, New Mexico and California, Vol. 28, No 3, May/June 2006.

[162]   Reagan, M.T., Najm, H.N., Debusschere, B.J., Maître, O.P.L., Knio, O.M. & Ghanem, R.G., Spectral stochastic uncertainty quantification in chemical systems. *Combustion Theory and Modelling*, **8**, pp. 607–632, 2004.

[163]   Reagan, M.T., Najm, H.N., Pebay, P.P., Knio, O.M. & Ghanem, R.G., Quantifying uncertainty in chemical systems modeling. *International Journal of Chemical Kinetics*, **37**, pp. 368–382, 2005.

[164]   Feeley, R., Seiler, P., Packard, A. & Frenklach, M., Consistency of a reaction dataset. *Journal of Physical Chemistry Part A*, **108**, pp. 9573–9583, 2004.

[165]   Smith, G.P., Golden, D.M., Frenklach, M., Moriarty, N.W., Eiteneer, B., Goldenberg, M., Bowman, C.T., Hanson, R.K., Song, S., Gardiner, W.C., Jr., Lissianski, V.V. & Qin, Z., Gri-mech 3.0, http://www.me.berkeley.edu/gri_mech/.